

Berkeley Seismological Laboratory



Annual Report
July 2008 - June 2009

Berkeley Seismological Laboratory
Annual Report
July 2008 - June 2009

Cover Picture

Remotely operated vehicle (ROV) being deployed to BSL station MOBB. Since February 27, 2009, the BSL's and MBARI's ocean bottom seismometer station, MOBB, is sending data to our datacenter in real time. This is the culmination of a long effort on the part of both institutions. In the week before it was connected to the ocean bottom MARS science node, a 3 km long power and data cable was laid out to the MOBB site.

Contents

1	Director's Report	1
1	Introduction	1
2	History and Facilities	1
3	BSL staff news	3
4	Acknowledgements	3
2	Research Studies	5
1	Tremor-tide Correlations and Near Lithostatic Pore Pressures on the Deep San Andreas Fault	6
2	Detection of Missing Repeating Earthquakes Using Recurrence Elements Analysis	8
3	TerraSAR InSAR Investigation of Active Crustal Deformation	10
4	Creep Measurements on the Concord Fault from PS-InSAR	12
5	Seismicity Changes and Aseismic Slip on the Sunda Megathrust Preceding the M_w 8.4 2007 Earthquake	14
6	Moment Moment Tensors for Very Long Period Signals at Etna Volcano, Italy	16
7	Temporal Variations in Crustal Scattering Structure near Parkfield, California, from Receiver Functions	18
8	Remote Triggering of Fault-Strength Changes on the San Andreas Fault at Parkfield	20
9	Source Analysis of the Memorial Day Explosion, Kimchaek, North Korea	22
10	Towards a continuous seismic wavefield scanning	24
11	The rupture process of the Parkfield SAFOD target earthquakes obtained from the empirical Greens function waveform inversion method	26
12	Nonvolcanic Tremor Evolution in the Parkfield, CA Region	28
13	Stability of Local and Regional Coda: Application to the Wells, Nevada Sequence	30
14	Anomalous Moment Tensor Solutions for The Geysers, CA	32
15	Statistical Testing of Theoretical Rupture Models Against Kinematic Inversions	34
16	Testing ElarmS in Japan	36
17	Real-time Earthquake Detection and Hazard Assessment by ElarmS Across California	38
18	Joint Inversion of Group Velocity Dispersion and Long Period Waveforms for Upper Mantle Structure	40
19	Reactivation of an Archean Craton: Constraints from P- and S-wave Tomography in North China . .	42
20	Plume vs. Plate: Convection Beneath the Pacific Northwest	44
21	Imaging Shallow Cascadia Structure with Ambient Noise Tomography	46
22	Seismic Anisotropy Beneath Cascadia and the Mendocino Triple Junction: Interaction of the Subducting Slab with Mantle Flow	48
23	Recovering the Attenuation of Surface Waves from One-Bit Noise Correlations: A Theoretical Approach	50
24	The Origin of Seismic Anisotropy in the D''	52
25	Toward a 3D Global Attenuation Model in the Lower Mantle from the Earth's Free Oscillations	54
26	Anisotropic North American Lithosphere and its Boundary with Asthenosphere	56
27	Crustal Stress and Mechanical Anisotropy of the Lithosphere in Western North America	58
28	Berkeley 3-D Isotropic and Anisotropic S-velocity Model of North American Upper Mantle, Updated to June 2008	61
29	Weak Mantle in NW India Probed by Postseismic GPS Measurements Following the 2001 Bhuj Earthquake	63
30	Comprehensive Test Ban Monitoring: Contributions from Regional Moment Tensors to Determine Source Type and Depth	66

3 BSL Operations	67
1 Berkeley Digital Seismic Network	69
2 California Integrated Seismic Network	78
3 Northern Hayward Fault Network	83
4 Parkfield Borehole Network (HRSN)	93
5 Bay Area Regional Deformation Network	103
6 Northern California Earthquake Data Center	109
7 Data Acquisition and Quality Control	119
8 Northern California Earthquake Monitoring	124
9 Outreach and Educational Activities	130
Glossary	132
Appendix I Publications, Presentations, and Panels 2008-2009	134
Appendix II Seminar Speakers 2008-2009	148
Appendix III Organization Chart 2008-2009	150

Chapter 1

Director's Report

1 Introduction

As in previous years, I am pleased to introduce the 2008-09 Berkeley Seismological Laboratory Annual Report. This report covers two interrelated activities at BSL: basic research and real time earthquake monitoring operations. Chapter 2 describes the research accomplishments; Chapter 3 details progress in our development of infrastructure and facilities.

The basic research spans many topics in seismology and tectonics. They range from studies of the earth's deep structure and dynamics to various aspects of earthquake physics; from microearthquakes and tremor studies to studies of earthquake mechanisms and rupture spanning different times scales; and from slow tectonic deformation, to real time seismology and earthquake early warning. These are described in 30 short contributions in Chapter 2 of this report.

This year, I wish to particularly highlight two major accomplishments on the operational side of the BSL. First, after almost ten years of sustained efforts involving our CISN partners at the US Geological Survey and Caltech, and after many intermediate steps, we finally have a completely integrated earthquake notification system across the State of California. Notably, as of June 2009, completely mirrored systems operate continuously and in real time across the San Francisco Bay (at Berkeley and USGS Menlo Park), backing each other up in case of downtime due to failure or maintenance. This system relies on complementary seismic data from the Berkeley and USGS Northern California networks. The next step, which we are starting to plan, is to integrate real time GPS data into the system. This involves coordination with USGS Menlo Park in Northern California, and with various partners in southern California (i.e. USGS, UCSD). Towards this goal, we have continued to convert GPS data acquisition from our continuous GPS BARD (BARD network) to high rate sampling (1Hz), and have recently reorganized and consolidated the BARD data acquisition and processing system. Second, in March 2009, the autonomous ocean floor broadband station MOBB (Monterey Bay Ocean

Bottom Broad Band Observatory), which we have operated in collaboration with the Monterey Bay Aquarium Research Institute (MBARI) since 2002, was connected to the MARS cable (<http://www.mbari.org/mars>). It is now sending data continuously and in real time to the BSL, where we are integrating the data with those of the land-based stations, as a demonstration project for earthquake real-time notification.

Finally, I note that the development of replacement electronics for the STS-1 very broadband seismometers, under the technical leadership of our collaborator, Metrozet, Inc. has been completed. We are now actively assisting Metrozet in the ambitious goal of building a modernized version of the mechanical sensor. This unique seismometer, which revolutionized global seismology in the last 20 years, has not been produced by Streckeisen & Co. for several years. This raised considerable concerns in the international community. The BSL spearheaded the new development effort and helped secure funding for it from the NSF EAR-Instruments and Facilities program. We are designing a new baseplate for these seismometers, as well as participating in the testing of the new sensors.

The following sections give a brief historical overview of the BSL, and finally some BSL staff news.

2 History and Facilities

The Berkeley Seismological Laboratory (BSL), formerly the Berkeley Seismographic Station (BSS), is the oldest Organized Research Unit (ORU) on the UC Berkeley campus. Its mission is unique in that, in addition to research and education in seismology and earthquake-related science, it is responsible for providing timely information on earthquakes (particularly those that occur in northern and central California) to the UC Berkeley constituency, to the general public, and to various local and state government and private organizations. The BSL is therefore both a research center and a facility/data resource, which sets it apart from most other ORUs. A major component of our activities is focused on developing and maintaining several regional obser-

vational networks, and participating, along with other agencies, in various aspects of the collection, analysis, archival, and distribution of data pertaining to earthquakes, while maintaining a vigorous research program on earthquake processes and Earth structure. In addition, the BSL staff spends considerable time on public relations activities, including tours, talks to public groups, responding to public inquiries about earthquakes, and, more recently, World-Wide-Web presence (<http://seismo.berkeley.edu/>).

UC Berkeley installed the first seismograph in the Western Hemisphere at Mount Hamilton (MHC) in 1887. Since then, it has played a leading role in the operation of state-of-the-art seismic instruments and in the development of advanced methods for seismic data analysis and interpretation. Notably, the installation, starting in 1927, of Wood-Anderson seismographs at 4 locations in northern California (BKS, ARC, MIN and MHC) allowed the accurate determination of local earthquake magnitude (M_L) from which a unique historical catalog of regional earthquakes has been maintained to this day, providing crucial input to earthquake probabilities studies.

Over the years, the BSS continued to keep apace of technological improvements. The first centrally telemetered network using phone lines in an active seismic region was installed by BSS in 1960. The BSS was the first institution in California to operate a 3-component "broadband" system (1963). It played a major role in the early characterization of earthquake sources using "moment tensors" and source-time functions. The BSS also made important contributions to the early definitions of detection/discrimination of underground nuclear tests and, jointly with UCB Engineering, to earthquake hazards work. Starting in 1986, the BSS acquired 4 state-of-the-art broadband instruments (STS-1), while simultaneously developing PC-based digital telemetry, albeit with limited resources. As the telecommunication and computer technology made rapid progress, in parallel with broadband instrument development, paper record reading was completely abandoned in favor of largely automated digital data analysis.

The current facilities of BSL have been built progressively over the last two decades, efforts initiated by significant "upgrade" funding from UC Berkeley in 1991-1995. The BSL currently operates and acquires data, continuously and in real-time, from over 60 regional observatories. These house a combination of broadband and strong motion seismic instrumentation installed in vaults, borehole seismic instrumentation, the permanent GPS stations of the Bay Area Regional Deformation (BARD) network, and electromagnetic sensors. The seismic data are fed into the BSL real-time processing and analysis system. Since 1996, they are used in conjunction with data from the USGS NCSN network in the joint earthquake notification program for northern California. This

program capitalizes on the complementary capabilities of the networks operated by each institution to provide rapid and reliable information on the location, size and other relevant source parameters of regional earthquakes. In recent years, a major emphasis in BSL instrumentation has been in densifying the state-of-the-art seismic and geodetic networks. At the same time, research efforts have been directed toward the development of robust methods for quasi-real time, automatic determination of earthquake source parameters and predicted strong ground motion, using a sparse network combining broadband and strong motion seismic sensors, as well as permanent geodetic GPS receivers. Recently research emphasis has been directed toward the development of "earthquake early warning" capabilities

The Berkeley Digital Seismic Network (BDSN), a regional network of 32 digital broadband and strong motion seismic stations with continuous telemetry to UC Berkeley, is the backbone of the BSL operations. This network provides the basic regional data for the real-time estimation of location, size and rupture parameters for earthquakes of M 3 and larger in central and northern California, within our Rapid Earthquake Data Integration (REDI) program. It is the Berkeley contribution to the California Integrated Seismic Network (CISN). The REDI program was replaced this June by the CISN software (see 8). The data from the BDSN also provide a fundamental database for the investigation of three-dimensional crustal structure and its effects on regional seismic wave propagation. This is ultimately crucial for estimating ground shaking for future earthquakes. Most stations also record auxiliary temperature/pressure channels, valuable in particular for background noise quality control. Complementing this network is a ~ 25 station "high-resolution" network of borehole seismic sensors located along the Hayward Fault (HFN) and under the Bay Area bridges, operated jointly with the USGS/Menlo Park and linked to the Bridge Safety Project of the California Department of Transportation (Caltrans). The latter has facilitated the installation of sensor packages at 15 bedrock boreholes along 5 east bay bridges in collaboration with Lawrence Livermore National Laboratory (LLNL). A major science goal of this network is to collect high signal-to-noise data for micro-earthquakes along the Hayward Fault to gain insight into the physics that govern fault rupture and its nucleation. The BSL also operates and maintains the 13 element Parkfield borehole seismic array (HRSN). This array provides high quality data on micro-earthquakes, clusters and most recently tremors, and is an important reference for the San Andreas Fault Observatory at Depth (SAFOD). Since April 2002, the BSL collaborates with MBARI on the operation of a permanent broadband ocean bottom station, MOBB.

In addition to the seismic networks, the BSL oper-

ates, maintains and processes data from the 30 permanent geodetic stations of the BARD Network. It archives and distributes this data as well. Where possible, BARD sites are collocated with BDSN sites to minimize telemetry costs. In particular, sites are progressively being upgraded to 1 Hz sampling. This will support one focus of BSL research, the development of analysis methods which will combine seismic and geodetic data to rapidly estimate source parameters of significant earthquakes.

Finally, two of the BDSN stations (PKD, SAO) also share data acquisition and telemetry with 5-component electromagnetic sensors installed with the goal of investigating the possibility of detection of tectonic signals. In 2002-2003, automated quality control software was implemented to monitor the electromagnetic data.

Archival and distribution of data from these and other regional networks is performed at the Northern California Earthquake Data Center (NCEDC), operated at the BSL in collaboration with USGS/Menlo Park. The data reside on a mass-storage device (current holdings \sim 40 terabytes), and are accessible “on-line” over the Internet (<http://www.ncedc.org>). Among others, data from the USGS Northern California Seismic Network (NCSN), are archived and distributed through the NCEDC. The NCEDC also maintains, archives and distributes the ANSS earthquake catalog.

Core University funding to our ORU has until now provided salary support for one staff scientist and several technical and administrative staff members, representing about 30% of the total infrastructure support. The remaining support comes from extra-mural grants and contracts, primarily from the USGS, NSF, and the State of California, through its Emergency Management Agency (CalEMA, formerly OES). We acknowledge valuable recent contributions from other sources such as Caltrans and PEER, as well as our Earthquake Research Affiliates. The effects of drastic budget cuts in FY09-10 are temporarily being offset by ARRA funding from the USGS. Over the next two years, these funds will allow us to upgrade the aging equipment at most of our remote observatories. This will put us in a better position to design the next generation earthquake notification system, the move towards earthquake early warning, using a combination of seismic and geodetic data.

3 BSL staff news

Changes in BSL staff in 2008-09 are as follows.

In the past year, the following graduate students associated with BSL completed their PhD’s: Ahyi Kim joined Schlumberger in Cambridge (UK) in summer 2009; Sean Ford is now a post-doc at Lawrence Livermore National Laboratory.

In the global seismology group, post-doc Laurent Stehly left for a research position at the University of

Nice (France). Post-doc Nicolas Houlié left in July 2009 and now holds a research position at the University of Leeds (UK). There have been several new arrivals: Scott French, Patrick Stutz-Boyer, Ana Luz Acevedo-Cabrera and Hong-Han Huang joined the BSL as graduate students in the Fall of 2009. Mathias Obrebski joined Richard Allen’s group as a post-doc in the Fall of 2008. Ingrid Johanson returned to Roland Burgmann’s group as a post-doc in October 2009. Since Nicolas Houlié’s departure in the Summer of 2009, she is helping out with the BARD program. After a brief stay in Hawaii, where she is finishing up a research project, she will take on an assistant researcher’s position at BSL and provide guidance to the field and data acquisition staff on matters related to BARD, and participate in the development of high rate GPS data assimilation in our earthquake notification system.

BSL hosted the following visiting scientists in 08-09: Liang Zhao (Institute of Geophysics, Chinese Academy of Sciences, Beijing) and Michael Slawinski (Department of Earth Sciences at Memorial University in Newfoundland, Canada). Shweta Sangewar (India Institute of Technology) and Fabian Walter (ETH Zürich, Switzerland) were summer interns in 2008.

As a result of a campus wide reorganization of the research administration of Organized Research Units, our four administrative staff have been laid off, effective November 30, 2009. Kristen, Tina and Yolanda have been rehired at RES (Research Enterprise Services), the new agency which will provide business administration to ORUs at Berkeley. Meanwhile, Kate is enjoying her new baby daughter Audrey and prospecting for job opportunities. They have been outstanding members of the BSL team, and we are sorry to see them go in spite of all our efforts. I wish them all the best for the future.

The greater BSL family has also grown, almost explosively, in the past year. We have welcomed four children of BSL staff and students in the past year. A baby boy, Kaito Taira, was born to Taka’aki Taira and his wife Akiko in August. Kate Lewis and her husband Justin had a girl, Audrey, in October. November brought two, somewhat early arrivals: Freeman McCarty was born to Jennifer Taggart and her husband Kevin McCarty, and Arieh Wurman-Fenton was born to Gilead Wurman and his wife Lori Fenton. We wish them all happiness and health.

4 Acknowledgements

I wish to thank our technical and administrative staff, scientists and students for their efforts throughout the year and their contributions to this Annual Report. Individual contributions to activities and report preparation are mentioned in the corresponding sections, except for the Appendix section, which was prepared by Kate

Lewis, Kristen Jensen and Jennifer Taggart.

I also wish to specially thank the individuals who have regularly contributed to the smooth operation of the BSL facilities: Mario Aranha, Rich Clymer, Doug Dreger, John Friday, Jarrett Gardner, Peggy Hellweg, Nicolas Houlié, Bill Karavas, Oleg Khainovski, Rick Lellinger, Pete Lombard, Rick McKenzie, Bob Nadeau, Doug Neuhauser, Charley Paffenbarger, Jennifer Taggart, Bob Uhrhammer, and Stephane Zuzlewski, and in the administrative office, Kristen Jensen, Kate Lewis, Tina Barber-Riggins and Yolanda Andrade. I also wish to thank our undergraduate assistants, Chris Rawles, Danny Feucht, Josef Matlak, Eric Winchell, Alicia Adams and Amanda Truyol for their contributions to our research and operations activities.

I am particularly grateful to Jennifer Taggart and Peggy Hellweg, for their help in putting together this Annual Report, and bringing it to closure under the present difficult circumstances.

The Annual Report of the Berkeley Seismological Laboratory is available on the WWW at http://seismo.berkeley.edu/annual_report.

Chapter 2

Research Studies

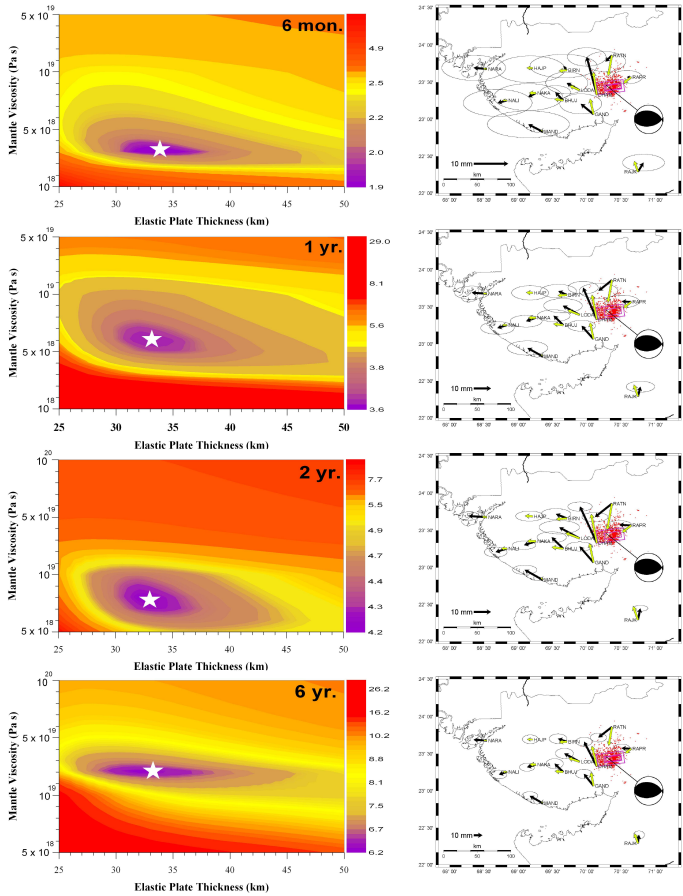


Figure 2.1: Model results. The RMS misfit between the calculated and observed horizontal displacements as a function of elastic plate thickness (H_p) and asthenosphere viscosity (η_a) for the two layer Earth model as a function of time since the earthquake. The star marks the best-fit displacement model with the lowest RMS error value. The best-fit horizontal displacements for each of the best-fit models is plotted adjacent to its misfit plot. Vectors in black denote the observed displacement tipped with 95% confidence ellipses and yellow arrows are the calculated model displacements. (Figure from Section 29)

1 Tremor-tide Correlations and Near Lithostatic Pore Pressures on the Deep San Andreas Fault

Amanda Thomas, Robert Nadeau, and Roland Bürgmann

1.1 Introduction

Early studies of non-volcanic tremor (NVT) attempted to relate the tremor signal and flow processes of fluids introduced from metamorphic dehydration in the subducting crust, but more recent evidence from subduction zone tremor in Japan and Cascadia indicates that tremor is directly associated with shear failure (*Shelly et al., 2006*). The presence of fluids and the significant impact small stress perturbations, such as tidal forcing, have on tremor activity implies low effective normal stresses are present in the tremor source region (*Gomberg et al., 2008; Miyazawa and Brodsky, 2008; Peng et al., 2008a; Rubinstein et al., 2007*).

Following the initial discovery in Japan and Cascadia, two additional tremor varieties were discovered in different tectonic environments: widespread triggered tremor, activated by dynamic stress changes associated with the passage of teleseismic surface waves (*Gomberg et al., 2008; Rubinstein et al., 2007*), and continuous tremor located deep on the San Andreas fault, near the 2004 Parkfield mainshock (*Nadeau and Dolenc, 2005*). The Parkfield tremor demonstrates several notable dissimilarities when compared to tremor in Cascadia and Japan, including continuous occurrence, changes in activity levels due to nearby intermediate-size earthquakes, and absence of an accompanying geodetic signature (*Nadeau and Dolenc, 2005; Smith, 2009*). In this study, we investigate the influence of tidal loading conditions on non-volcanic tremor on the San Andreas fault in order to determine if the Parkfield tremor is modulated by tides, resolve which tidal stresses affect tremor, and explore implications about the source region conditions.

1.2 Methods and Preliminary Results

We develop our analysis in parallel for the tremor catalog and two earthquake catalogs. We consider a regional catalog of events within $.5^\circ$ of Cholame, and a repeating micro-earthquake catalog located along the creeping segment of the San Andreas fault (*Nadeau and McEvilly, 2004*). We compute the extensional and shear strains induced in the lithosphere by the solid earth and ocean tides (*Agnew, 1997*). Assuming 2-D plane strain and linear elasticity, with an elastic modulus of 30 GPa and Poisson ratio of $.25$, we then convert the strains to stresses and resolve those stresses onto the fault normal and parallel (shear) directions on the San Andreas fault ($N45^\circ W$). For each catalog, the normal, shear, and Coulomb stresses and stress rates are computed for the

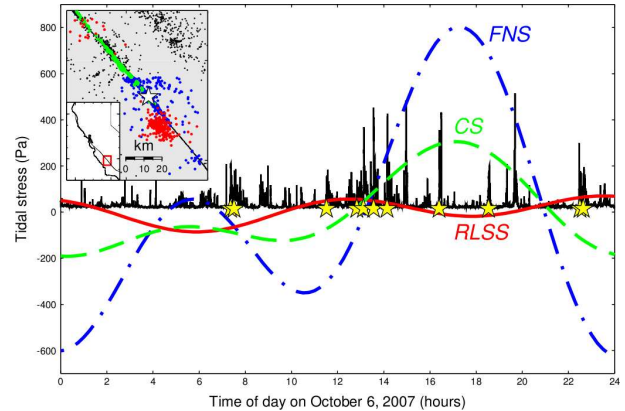


Figure 2.2: Example one-day tremor time series with superimposed tidal signals. Black is RMS envelope of tremor activity in Cholame. Red, blue, and green curves are the tidally induced fault-normal stress (FNS), right-lateral shear stress (RLSS), and Coulomb stress (CS) for $\mu=0.4$. Yellow stars mark tremor start times. Some short spikes in the RMS envelope are micro-earthquakes. Inset map shows tremor locations in red, regular earthquakes in blue, and the repeating earthquake catalog in green. Background earthquake activity is shown in black. White star indicates epicenter of the 2004 Parkfield earthquake.

start time of each event (Figure 2.2).

To investigate the influence of both the stress magnitude and rate on tremor occurrence, we divide the tremor into “quadrants” depending on the sign of the loading condition under which they occur. The tidal signal consists of a superposition of multiple harmonic functions, thus the amount of time that the tides induce a given load is not equal for all loading conditions. If tremor and tides are uncorrelated, the number of tremors that occur under a particular tidal loading condition will be directly proportional to the amount of time that condition exists. We use a chi-square test to establish the existence of a correlation using the null hypothesis that tremor start times are randomly distributed with respect to tidal influence. For the tremor catalog, the level of correlation of the normal, shear, and Coulomb stresses exceed the 99% significance level, while the correlation levels for the other catalogs are statistically insignificant. The lack of correlation in the earthquake catalogs is not surprising given the size of the catalogs and results from previous efforts to establish a significant tidal triggering of earth-

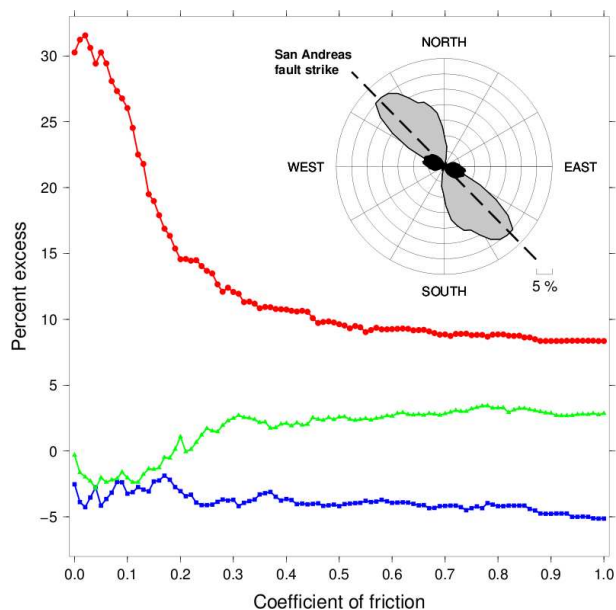


Figure 2.3: Percentage of excess events (i.e. above long term average) during times of positive ΔCS parallel to the San Andreas fault vs. effective coefficient of friction. Values for the tremor, regular, and repeating event catalogs are shown as red circles, blue squares, and green triangles respectively. Standard deviations (2σ) were computed using a bootstrap procedure on each friction value of each catalog. Maximum 2σ errors over all possible friction values are 5.66%, 5.80%, and 4.66% for the tremor, regular, and repeating catalogs respectively. The inset diagram displays the positive percent excess tremor for FNS (black) and RLSS (grey) relative to the fault orientation.

quakes in California (Beeler and Lockner, 2003; Lockner and Beeler, 1999).

We further explore this apparent correlation by comparing tremor start times with the loading conditions they occur under. Correlation between tremor occurrence and tidal stressing rate is insignificant for all components. Induced shear stresses ($\Delta RLSS$) demonstrate the most compelling correlation of the three magnitude comparisons, with distinct increases in tremor activity that correspond to positive (right-lateral) shear stresses parallel to the San Andreas fault and equally apparent decreases when values are negative. Additionally, the tremor surpluses and deficits become more pronounced as $\Delta RLSS$ increases to peak values of ± 150 Pa. Though normal stresses changes (ΔFNS) are much larger, they only exhibit a weak correlation at large, positive (tensile) values of greater than 1000 Pa. Coulomb stresses ($\Delta CS = \Delta RLSS + \mu \Delta FNS$, $\mu = 0.4$) exhibit less correlation than the shear stress alone.

Assuming tremor is caused by a frictional Coulomb

failure process, the optimal friction coefficient is the value that maximizes the number of events that occur during times of encouraged failure stress (Figure 2.3). Tremors show a marked increase for friction values near zero with a peak above 30% excess for $\mu = 0$. Percent excess for both the regular and repeating earthquake catalogs does not exceed 5%. This demonstrates that tidally induced shear stresses parallel to the San Andreas fault, while of much smaller magnitude than normal stress changes, have the most robust correlation with non-volcanic tremor near Parkfield. Since the stress perturbations are so small relative to the overburden stresses at these depths, this finding is indicative of very low effective normal stresses or near-lithostatic pore pressures at depth. Finally, going back to the initial assumption of the strike of the San Andreas fault in our stress calculations, we perform the same analysis to determine the percent excess tremor with respect to any vertical fault orientation (Figure 2.3, inset). The peak percent excess occurs at $N44^\circ W$, nearly parallel to the strike of the San Andreas fault.

1.3 Acknowledgements

Supported by the USGS through awards 06HQGR0167, 07HQAG0014, and 08HQGR0100, by the NSF through awards EAR-0537641, EAR-0544730, and the GRFP.

1.4 References

- Agnew, D. C., NLOADF: A program for computing ocean-tide loading, *JGR-Solid Earth*, 102, B3, 5109-5110, 1997.
- Beeler N. M., D. A. Lockner, Why earthquakes correlate weakly with the solid Earth tides: Effects of periodic stress on the rate and probability of earthquake occurrence, *J. Geophys. Res.*, 108(B8), 2391, doi:10.1029/2001JB001518, 2003.
- Gomberg, J., et al., Widespread triggering of nonvolcanic tremor in California, *Science*, 319, 5860, 173-173, 2008.
- Lockner, D. A., and N. M. Beeler, Premonitory slip and tidal triggering of earthquakes, *JGR-Solid Earth*, 104, B9, 20133-20151, 1999.
- Miyazawa M., E. E. Brodsky (2008), Deep low-frequency tremor that correlates with passing surface waves, *J. Geophys. Res.*, 113, B01307, doi:10.1029/2006JB004890.
- Nadeau, R. M., and T. V. McEvilly, Periodic pulsing of characteristic microearthquakes on the San Andreas Fault, *Science*, 303, 5655, 220-222, 2004.
- Nadeau, R. M., and D. Dolenc, Nonvolcanic tremors deep beneath the San Andreas Fault, *Science*, 307, (5708), 389-389, 2005.
- Peng, Z. G., et al., Strong tremor near Parkfield, CA, excited by the 2002 Denali Fault earthquake, *Geophys. Res. Lett.*, 35, 23, 2008a.
- Rubinstein, J. L., et al., Non-volcanic tremor driven by large transient shear stresses, *Nature*, 448, 7153, 579-582, 2007.
- Shelly, D. R., et al., Low-frequency earthquakes in Shikoku, Japan, and their relationship to episodic tremor and slip, *Nature*, 442, 7099, 188-191, 2006.
- Smith, E. F., A Search in Strainmeter Data for Slow Slip Associated with Triggered and Ambient Tremor near Parkfield, California, *Jour. Geophys. Res.*, In preparation, 2009.

2 Detection of Missing Repeating Earthquakes Using Recurrence Elements Analysis

Kate Huihsuan Chen, Roland Bürgmann, and Robert M. Nadeau

2.1 Introduction

Stress perturbations influence earthquake recurrence and are of fundamental importance to understanding the earthquake cycle and determining earthquake hazard. The large population of repeating earthquakes on the San Andreas fault at Parkfield provides a unique opportunity to examine the response of the repeating events to the occurrence of moderate earthquakes. We analyze 187 M -0.4 to 1.7 repeating earthquake sequences (RES) from the High Resolution Seismic Network catalog to estimate the impact of M 4-5 events on RES's timing. Here we adopt a recurrence element analysis based on five recurrence elements (Fig. 1a): (1) $dt+$: the time difference between a major earthquake and the first subsequent recurrence of a repeating event; (2) $dt-$: the time difference between a major earthquake and the most recent repeating event; (3) Tr_{cos} : the recurrence interval spanning the major event; that is, the sum of $dt-$ and $dt+$; (4) Tr_{post} : the duration of the first full recurrence interval following the major event, and (5) Tr_{pre} : last recurrence interval just preceding the potential trigger. These elements are divided by the average 1987-1998 recurrence interval of a given RES to obtain the normalized values of $dt+^*$, $dt-^*$, Tr_{cos}^* , Tr_{post}^* , and Tr_{pre}^* . Very short recurrence elements of $dt+^*$ (i.e., smaller than 10% of the typical cycle) can indicate the immediate triggering due to the major event, whereas longer than 1 Tr_{cos}^* , Tr_{post}^* , and Tr_{pre}^* reflect a population of missing events.

2.2 Recurrence elements associated with M 4-5 events

For each RES, the five recurrence elements associated with every M 4-5 event are calculated (Fig. 1a). In Fig. 1b, the RES within 5 km distance from the major events tend to have a high fraction of short $dt+^*$ (< 0.1). Fig. 1b-d also show the percentage of events within a given distance range that have a $dt+^*$ less than the threshold specified. For example, more than 30% of the events within 2 km distance have $dt+^* < 0.1$, whereas within distances of greater than 5 km $\sim 10\%$ of the RES exhibit such rapid recurrence. The percentage of short $dt+^*$ remain unchanged for events beyond 5 km. To confirm that the observed short $dt+$ population indicates the triggering effect of M 4-5 events, we compare the observed distribution of $dt+^* < 0.1$, $0.1-0.2$, and > 0.5 with $dt+^*$ values generated from randomly generated times of the five M 4-5 events. The 30 sets of 5 randomly generated M

4-5 times (150 runs in total) produce roughly equal percentages of $dt+^*$ at most distances, as shown by the blue lines in Figure 1. The random behavior of the small $dt+^*$ population ($dt+^* < 0.1$) is strikingly different from the real population in the near field of the M 4-5 events (< 5 km). Beyond 5 km, however, the observed $dt+^* < 0.1$ distribution matches the synthetic $dt+^*$. Compared to $dt+^*$ curves, the fraction of short $dt-^*$ measured over the same range of distances do not reveal systematic change with distance. The percentages of the observed $dt-^*$ at all distances match the value of $dt-^*$, as one can expect from random behavior.

2.3 Undetected repeating events?

In Figure 2, the histogram of Tr_{pre}^* reveals a somewhat broader distribution with median value of 1.62. The median Tr_{pre}^* is about a half cycle shorter than the median value of 1.14 and 1.29 for Tr_{cos}^* and Tr_{post}^* , respectively. This suggests a general pattern of shortened interval at and following the time of M 4-5 events. Note that the small secondary peak in Fig. 2b is about twice the normalizing interval, indicating some missed recurrences that may have occurred during the trigger event. Given that a single skipped event in a sequence leads to a Tr_{cos}^* value of slightly greater than 1, the second peak at $Tr_{cos}^* \sim 2$ is suggestive a number of unrecognized repeating event. And since the secondary peak near 2 is minor, the undetected repeating events are unlikely to have significant influence on the M 4-5 triggering effect. We also note that Tr_{post}^* is also somewhat reduced compared to pre-event recurrences, indicating the possible role of afterslip or general acceleration of slip in the early 1990s.

2.4 Summary

We illustrate the effect of major events on earthquake cycles of nearby characteristically repeating micro-earthquakes and determine the distance over which triggering can be documented. We find evidence that the five M 4-5 events that occurred at Parkfield triggered small, nearby repeating earthquakes. The triggering effect can only be seen in the near-field (< 5 km) by the measures of rapid recurrence subsequent to the major event. A small population of missing repeating events at the time of a major event is also detected by the longer-than-average intervals spanning and following a major event. In future

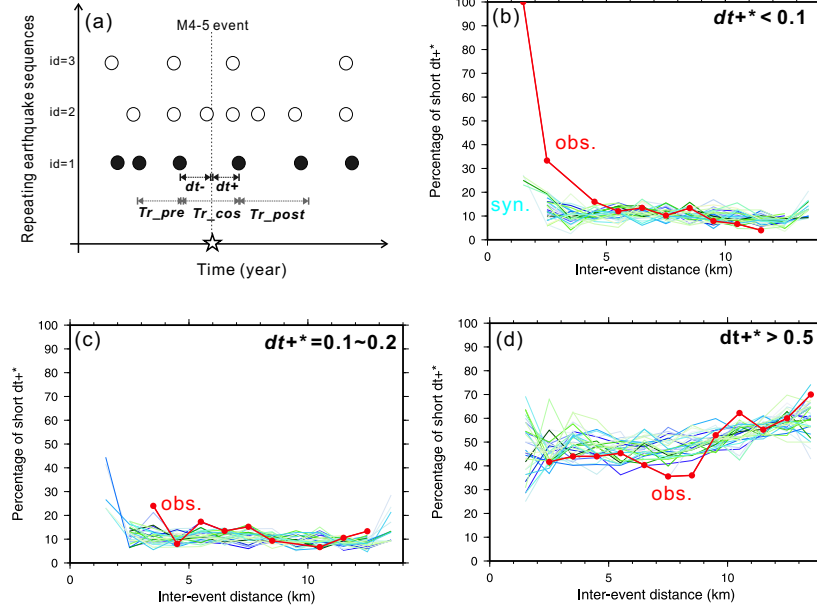


Figure 2.4: (a) Schematic illustration of the five recurrence elements, dt_+ , dt_- , Tr_{pre} , Tr_{cos} , and Tr_{pos} . Percentage of (b) $dt_+^* < 0.1$ (c) $0.1 < dt_+^* < 0.2$ (d) $dt_+^* > 0.5$ as a function of distance from M 4-5 events for real data (red line) and synthetic data (blue lines generated by 30 sets of 5 randomly drawn of M 4-5 event times). Note that the percentage in each distance bin (1 km) is calculated when the dt_+^* number is greater than 3.

work, we will consider whether interaction with nearby $M < 4$ events plays an additional important role in the RES recurrence patterns. We will also explore in detail the response of the RES to the M 6 2004 Parkfield earthquake.

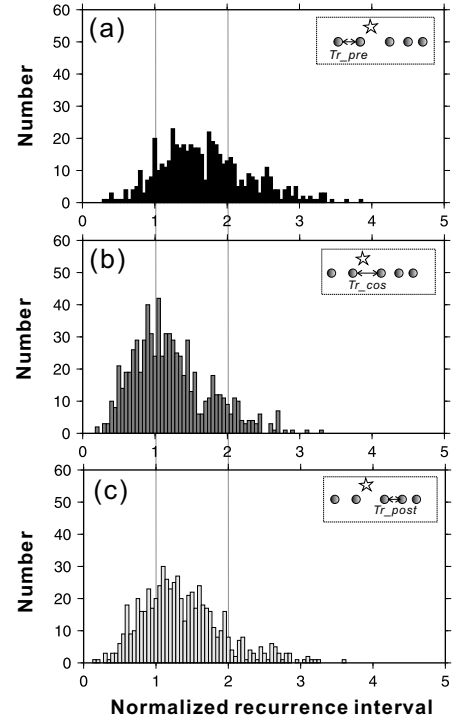


Figure 2.5: Histograms of Tr_{pre}^* , Tr_{cos}^* , and Tr_{post}^* determined by the average recurrence intervals of full period. Grey lines denote the normalized recurrence intervals of 1 and 2.

3 TerraSAR InSAR Investigation of Active Crustal Deformation

Ling Lei and Roland Bürgmann

3.1 Introduction

This project aims to utilize advanced analysis of TerraSAR data to investigate the dynamics and interactions of solid Earth deformation processes, such as earthquakes and fault creep, and Earth surface processes, such as land subsidence and groundwater movements, in a densely populated, urban region, the San Francisco Bay Area. Results from TerraSAR data will be carefully compared and integrated with InSAR data from other spacecraft, including the ERS-1/2, Envisat, RADARSAT-1, and ALOS satellites, and will be integrated in a rigorous analysis and monitoring effort of active surface deformation in the region. Ongoing deformation imaging reveals a number of natural hazards, including elastic strain accumulation about seismologic faults, active landsliding, land subsidence and rebound, and settling of unconsolidated sediments that are highly susceptible to liquefaction. Up to now, we have ordered and received 20 TerraSAR-X Spotlight Single Look Complex (SLC) images and 4 Stripmap SLC images delivered by the German Aerospace Centre (DLR) and obtained a few primary preliminary results.

3.2 Data analysis and processing

The TerraSAR-X images were acquired over the San Francisco Bay Area, particularly around an area of active landsliding, coastal subsidence, and shallow Hayward fault creep near the city of Berkeley. Berkeley is situated between 37.45° and 38.00° latitude, and 237.30° and 238.00° longitude. The data acquisition interval is from November, 2008 to July, 2009. Four types of Spotlight images and one type of Stripmap image in time sequence were ordered and acquired: spot_012, spot_038, spot_049, spot_075, and strip_003, having different look angles and pass directions. The data acquired with the standard Spotlight mode are with 1m pixel resolution, 10 km wide swath, and HH polarization. A TerraSAR-X Spotlight scene covers approximately $10*5\text{km}^2$. Actually, there are 122 spotlight beams called spot_001 to spot_122 and 8 different beams of Spotlight data over the Berkeley area. But the recommended performance beams of Spotlight images are spot_010 to spot_079. So we chose four recommended beams of all the available beams for the Bay Area. Details of the data set used are mentioned in Table 2.1. Access to the SAR data is via FTP about 10 days after acquisition date.

The data is supplied in TerraSAR-X standard SLC COSAR (COMplex SAR) format with orbital information in an Extensible Markup Language (XML) header.

The file contains integer real-complex components with double sampling and calibration constants for values. The COSAR file contains all focused complex SAR data of one beam in a burst-by-burst order, together with sample validity and position annotation. Stripmap and Spotlight images consist of one burst in that sense. The huge variety of level 1b product types for TerraSAR-X (complex, detected, geocoded) requires product annotation in an extensible and dynamic format.

I am using ROLPAC to do the interferograms. But ROLPAC was designed to process raw data rather than SLC images. So there are two main problems. One is that ROLPAC does the azimuth spectrum filtering (cutting out the part of the azimuth spectrum that does not overlap) in the "roi" program. So "resamp_roi" has to be changed to do the azimuth spectrum filtering in the interferogram formations. The other is that there is a significant difference between the way that ROLPAC and other SAR processors use the Doppler centroid in the SLC formation. ROLPAC is set up to process the SLC in the original geometry, but the TerraSAR processor produces the SLC images in a deskewed geometry. The deskewing moves the data to adjust for the squint or angle between the radar line of sight (LOS) and projects it perpendicular to the orbit track.

Another problem is the processing with the Spotlight data. In order to form coherent Spotlight interferograms from two SAR observations, the following two conditions must be met: the ground projected-range spectra of both observations must overlap, and the received Doppler frequency spectra must overlap as well. The nonstationary squint angle during spotlight imaging also causes a negative drift of the Doppler centroid frequency in the SAR data. So the linear Doppler drift in azimuth has to be removed and Doppler centroid set to zero before making interferograms. We are now still working on those problems and will hopefully get better results in the near future. Here are some preliminary results: a Stripmap interferogram (Figure 2.6) and a Spotlight interferogram (Figure 2.7). I also plotted the landslides areas around Berkeley Hills. There are four large, slow moving, deep-seated landslides. All the landslides extend through residential areas and move on the order of cm/year, each covering an area of roughly $0.25\text{-}1.00\text{ km}^2$

3.3 Acknowledgements

We thank the German Aerospace Centre (DLR) for providing TerraSAR-X data for this project. We thank Paul Lundgren, Eric J. Fielding, and Paul Rosen for

Date	Time	Polarization Mode	Polarization Channels	Incidence Angles	Pass Direction	Beam
2008-11-26	14:23:42UTC	Single	HH	21.78	D	spot_012
2008-12-18	14:23:40UTC	Single	HH	21.78	D	spot_012
2009-01-09	14:23:38UTC	Single	HH	21.78	D	spot_012
2009-02-22	14:23:38UTC	Single	HH	21.78	D	spot_012
2009-04-07	14:23:38UTC	Single	HH	21.78	D	spot_012
2008-11-18	2:00:28UTC	Single	HH	34.14	A	spot_038
2009-01-12	2:00:24UTC	Single	HH	34.14	A	spot_038
2000-02-25	2:00:24UTC	Single	HH	34.14	A	spot_038
2009-04-10	2:00:20UTC	Single	HH	34.14	A	spot_038
2009-07-18	2:00:29UTC	Single	HH	34.14	A	spot_038
2008-11-21	14:15:09UTC	Single	HH	38.94	D	spot_049
2008-12-24	14:15:08UTC	Single	HH	38.94	D	spot_049
2009-02-28	14:15:07UTC	Single	HH	38.94	D	spot_049
2009-04-13	14:15:02UTC	Single	HH	38.94	D	spot_049
2009-07-21	14:15:11UTC	Single	HH	38.94	D	spot_049
2008-11-23	2:09:01UTC	Single	HH	47.82	A	spot_075
2008-12-26	2:08:59UTC	Single	HH	47.82	A	spot_075
2009-03-02	2:08:56UTC	Single	HH	47.82	A	spot_075
2009-04-15	2:08:53UTC	Single	HH	47.82	A	spot_075
2009-07-23	2:09:02UTC	Single	HH	47.82	A	spot_075
2009-05-10	14:23:39UTC	Single	HH	21.45	D	strip_003
2009-05-21	14:23:43UTC	Single	HH	21.45	D	strip_003
2009-07-26	14:23:39UTC	Single	HH	21.45	D	strip_003
2009-08-06	14:23:43UTC	Single	HH	21.45	D	strip_003

Table 2.1: Information on the data acquired

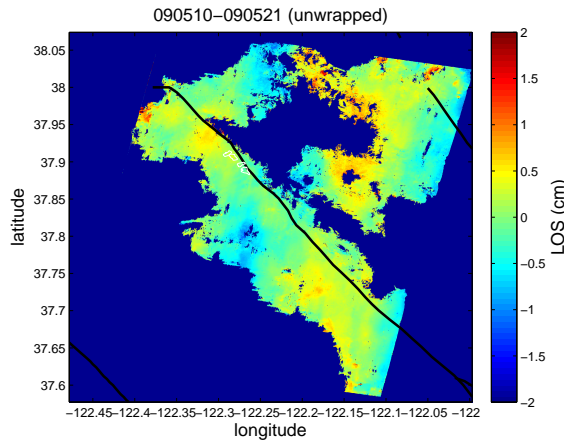


Figure 2.6: Interferogram for Stripmap pair of 10th May and 21st May, 2009

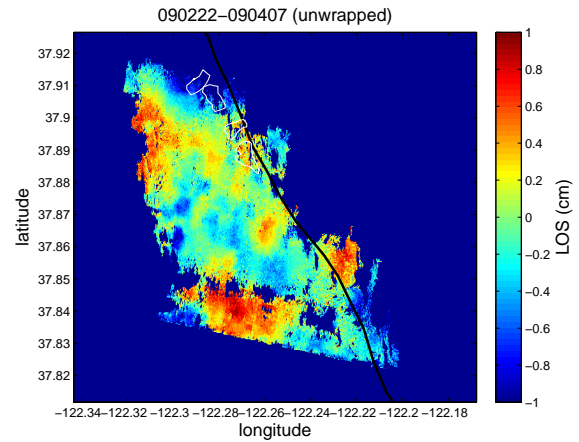


Figure 2.7: Interferogram for Spotlight pair of 22nd Feb. and 7th April, 2009

providing TerraSAR reading codes and beneficial discussions.

3.4 References

TerraSAR-X Ground Segment Basic Product Specification Document, TX-GS-DD-3302.
TerraSAR-X Ground Segment Level 1b Product Format Specification, TX-GS-DD-3307.

Bürgmann, R., E. Fielding, and J. Sukhatme, Slip along the Hayward fault, California, estimated from space-based synthetic aperture radar interferometry, *Geology*, 26, 559-562, 1998.

Eineder, M., N. Adam, and R. Bamler, Spaceborne Spotlight SAR Interferometry With TerraSAR-X, *IEEE Trans. Geosci. Remote Sens.*, 5, 1524-1535, 2009.

4 Creep Measurements on the Concord Fault from PS-InSAR

Ingrid Johanson, Roland Bürgmann, Alessandro Ferretti (TRE, Milan) and Fabrizio Novali (TRE, Milan)

4.1 Introduction

We use PS-InSAR (permanent scatterer interferometric synthetic aperture radar) measurements to study surface creep on the Concord fault in the Eastern Bay Area. Creep on the Concord fault has previously been measured in two locations using alignment arrays (*McFarland et al.*, 2009). The alignment arrays found that creep occurs at rates of 2.5-3.5 mm/yr and mostly in episodes every 3-5 years. InSAR provides dense measurements of ground motion that allow us to measure fault creep along several cross-fault profiles and gain a sense of the distribution of creep along-strike. The PS-InSAR method identifies and integrates individual points with stable phase measurements (outcrops, buildings, utility poles, etc.) in all SAR acquisitions of an area of interest. PS-InSAR provides time-series of range-change measurements that we can use to resolve deformation rates at high precision (<1 mm/yr). This may allow us to also resolve some of the variability in the Concord fault's creep rate.

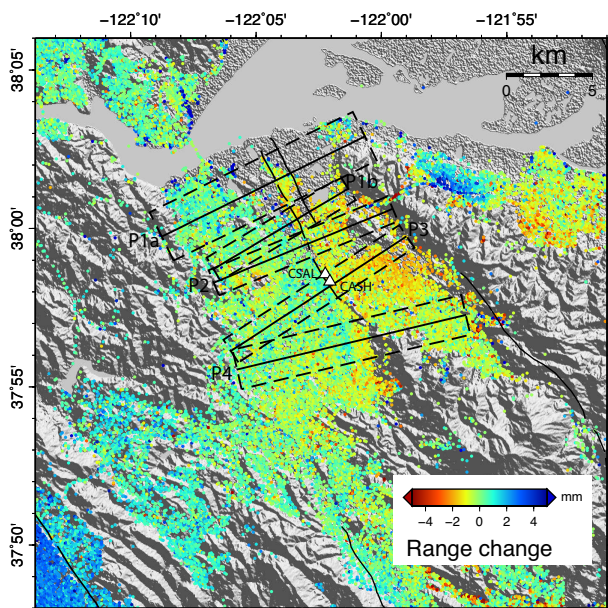


Figure 2.8: Overview map showing mean velocity of each PS-InSAR points from 46 InSAR scenes spanning 1992-2001. Dashed boxes are the areas included in the swath averages, which are then projected onto the solid black centerlines. The two alignment arrays, CSAL and CASH, are shown as white triangles and fall mostly within Profile 3 (P3).

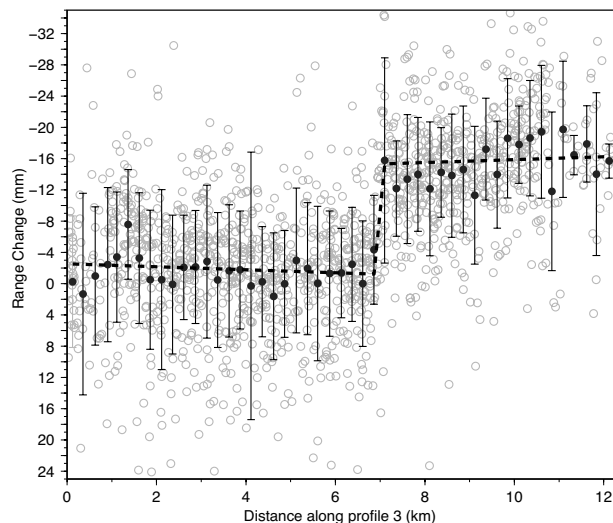


Figure 2.9: An example of a swath average profile; this is for profile 3 on 12/9/2001, referenced to 5/6/1992. Grey circles are the actual PS-InSAR points within the dashed box in Figure 2.8 and projected onto the centerline. Black circles are the derived swath averages; averages of all points inside a 0.25 km bin. Error bars are one standard deviation of the PS-InSAR points comprising each swath average. The dashed black line is fit to the data using a linear inversion and the fault creep is measured from the offset of the profile at the fault trace.

4.2 Measuring creep from PS-InSAR

We use 46 acquisitions from the European Space Agency's ERS1 & 2 satellites, on descending track 70, frame 2853, and spanning from 1992 through 2001. The data were processed using the PS-InSAR method of *Ferretti et al.* (2001) to produce time series of range change (change in distance between the ground and satellite) for each point shown in Figure 2.8. To measure creep on the Concord fault, we look at motion along several profiles through the Permanent Scatterers (PSs), crossing the Concord fault. We use swath averaging to construct each profile. Within each swath, shown as dashed lines in Figure 2.8, points within 0.25 km bins perpendicular to the fault are averaged together and projected onto the centerline. For example, all points between 0.5 and 0.75 km west of the fault are averaged together to provide one point on the profile and their standard deviation provides an estimate of the profile point's uncertainty.

A swath average profile is constructed for all 46 acqui-

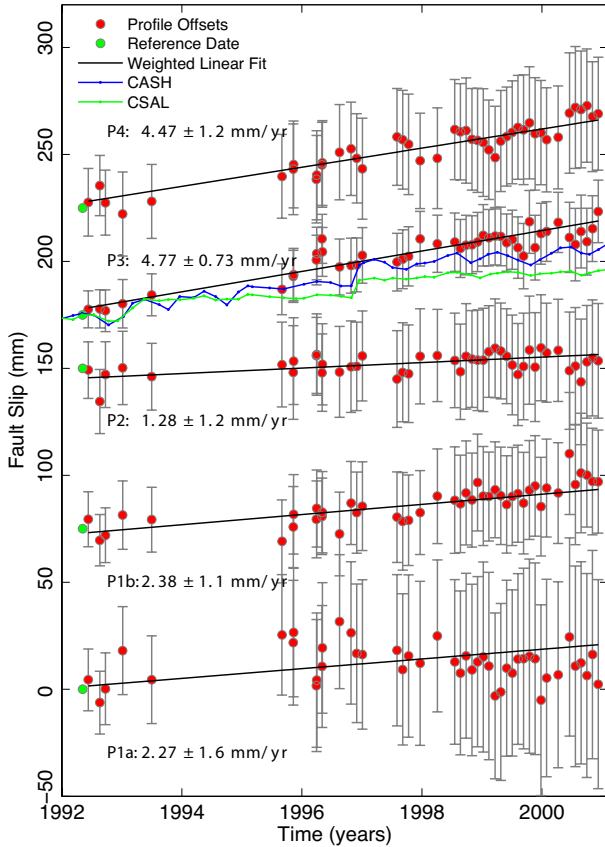


Figure 2.10: Surface creep through time for the five profiles shown in Figure 2.8. Individual time series are offset from each other for clarity. The creep rate as determined from a weighted linear inversion is printed next to each series. Alinement array measurements from sites CSAL and CASH are plotted with Profile 3 (P3) for comparison.

sition dates on each of the five profiles, for a total of 230 profiles (an example is shown in Figure 2.9). A linear inversion is performed on each profile to obtain the offset at the fault trace, produced by the shallowly creeping fault. Each offset value represents the amount of creep on the Concord fault since the beginning of the time series in 1992.

4.3 Long-term creep rates

Time series of profile offsets for all five profiles are shown in Figure 2.10. By fitting a line to the offsets, we can obtain a measurement of the creep rate at each profile. The two northern-most profiles (P1a & P1b) have creep rate of 2.3-2.4 mm/yr; this is very low, but measurable within the calculated uncertainty of 1.1-1.6 mm/yr. The creep rate continues to be low southward through profile 2 (P2), where the measured rate could be zero within uncertainty. Creep picks up fairly suddenly at pro-

file 3 (P3), which is near the portion of the fault known to creep from alinement arrays. Time series of creep measurements from the alinement arrays are plotted with the time series from P3 in Figure 2.10. Both arrays measure slightly lower creep rates than is indicated by P3, but support the idea that the creep rate is increasing toward the south. CSAL is the more northern alinement array and is on the north edge of P3 (see Figure 2.8); it has a lower creep rate (2.8 mm/yr) than CASH (3.7 mm/yr), which is located toward the center of P3. P3 incorporates more data to the south of CASH, which may explain its higher creep rate. Higher rates of creep continue in profile 4 (P4), our southern-most profile.

4.4 Time-variable creep

Creep on the Concord fault has also been shown by alinement array measurements to be episodic, with a 3-5 year period. This variability is within the uncertainty in the profile offsets and could not be independently detected using the PS-InSAR data. However, offsets for P3 match some of the variability in alinement array CASH, particularly post-1998, suggesting that there is information available in the PS-InSAR data on the time variability of Concord fault creep.

4.5 Acknowledgements

This work was supported by USGS-NEHRP external grant #08-HQGR-0095. SAR data are copyrighted by the European Space Agency and were obtained via the WInSAR consortium.

4.6 References

Ferretti, A., C. Prati, and F. Rocca, Permanent scatterers in SAR interferometry, *IEEE Trans. Geosci. Remote Sens.*, 39, 8-20, 2001.
 McFarland, F., J. Lienkaemper, and S. J. Caskey, Data from theodolite measurements of creep rates on San Francisco Bay region faults, California; 1979-2009, *USGS Open file report 09-1119*, 2009.

5 Seismicity Changes and Aseismic Slip on the Sunda Megathrust Preceding the M_w 8.4 2007 Earthquake

Kelly Grijalva, Roland Bürgmann, and Paramesh Banerjee (Earth Observatory of Singapore)

5.1 Introduction

The September 12, 2007 Sumatra M_w 8.4 earthquake initiated ~ 750 km south of the 2005 epicenter. Twelve hours later, a deeper M_w 7.9 aftershock ruptured further to the north. Their occurrence, close in time and space to the 2004 M_w 9.2 Sumatra-Andaman earthquake, 2005 M_w 8.7 Nias earthquake, and 2000 M_w 8.0 Enggano earthquake, suggests the possibility of these being triggered events. Coulomb failure stress models have shown that the 2000 earthquake had a larger impact at the 2007 hypocenter than the 2004 and 2005 earthquakes, and could have contributed to its southern location. We investigate seismicity changes and GPS-measured velocities, in the 2007 rupture region, for alternative triggering evidence.

5.2 Seismicity Rate Changes

We investigate seismicity rate changes in Southern Sumatra using the standard Beta-statistic approach (e.g. *Reasenburg & Simpson, 1992*). Beta will be positive when the postseismic rate is higher than the background seismicity rate, and negative when it is lower. Our earthquake catalog consists of the preferred events from IRIS SeismiQuery (<http://www.iris.washington.edu/SeismiQuery>). The magnitude of completeness for this catalog, which starts in 1980, is 4.7. In order to reduce the effect of aftershocks, we use ZMAP (*Wiemer, 2001*) to decluster our catalog.

The number of annual earthquakes increased greatly for the time period following the 2000 earthquake and before the 2004 earthquake. When calculating an average value of β for the 2007 high-slip region, approximated by longitude 99° - 102.5° and latitude 1° - 5° S, the largest two spikes in β occur after the 2000 and 2005 earthquakes (Figure 2.11).

Figure 2.12 shows β calculated for 1 year time intervals and spatially binned into 1° squares. In general, the seismicity level has been extremely elevated in Western Sumatra and the offshore region north of the equator. In 2005, there was a cluster of aftershocks near Siberut Island, as evident by $\beta > 10$. From 2005-2007, there was a more moderate increase in seismicity near the Mentawai Islands of Sipora, North Pagai, and South Pagai, regions that slipped during the 2007 earthquake sequence. In 2005, there were moderate seismicity increases of up to $\beta = 4$, in the 1° squares surrounding the 2007 hypocenter. There was a slight decrease in seismicity in the squares containing the 2007 and 2000 epicenters. In 2006, the

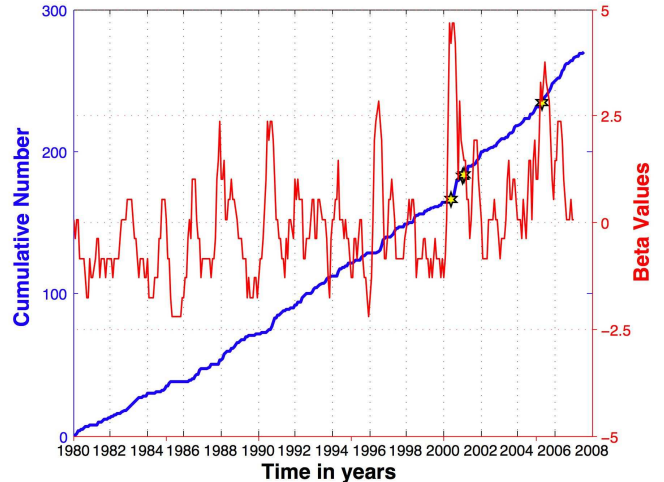


Figure 2.11: Beta values in the 2007 high-slip region are plotted in red (see Figure 2.13 for high-slip contours). The blue line indicates the cumulative number of $M \geq 4.7$ earthquakes since 1980. The yellow stars indicate earthquakes with $M > 6.5$.

seismicity increased in the 2007 and 2000 squares, but decreased significantly in the surrounding region. The β values continued to decrease down to average levels during the first 9 months of 2007, before the September earthquake. If one compares the post-2004 seismicity levels with just the 1980-1999 catalog, thereby removing the effect of the 2000 earthquake, the seismicity levels are significantly higher in the epicentral region.

5.3 Aseismic Slip on the Megathrust

GPS-measured velocities in Southern Sumatra have been centimeters above their interseismic rates during the years following the 2004 earthquake (*Sumatran GPS Array* data). Figure 2.13 shows the 2006 and 2007 (up to the September earthquake) GPS velocities in the 2007 high-slip region, with horizontal and vertical interseismic velocities removed (*Apel et al., 2006; Natawidjaja et al., 2007*). We invert these GPS velocities for dipslip motion on the Sunda megathrust. The 2006 and 2007 inversions reveal an increased level of coupling on the deeper portion of the seismogenic zone, from ~ 15 - 75 km depth, northwest of the M_w 8.4 high-slip patch. In addition, there was centimeters of aseismic reverse-slip over the region that slipped during the 2007 main event.

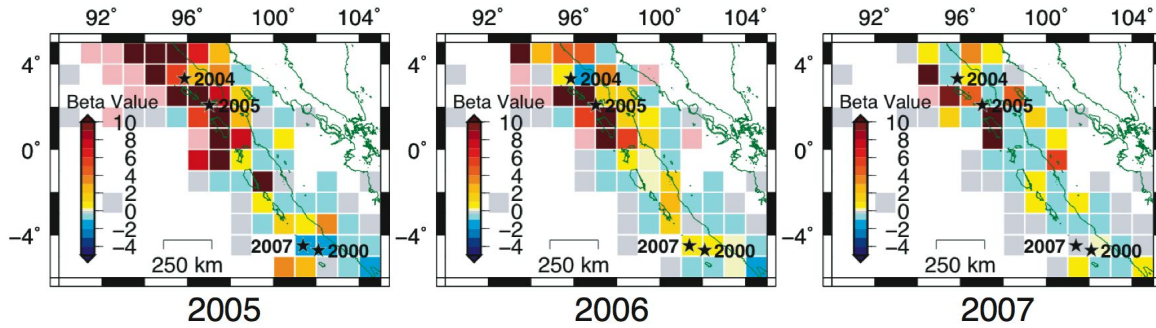


Figure 2.12: Beta values showing the relative change in seismicity following the 2004 earthquake compared to the time period 1980-2004. The pink squares signify regions where there were no earthquakes during the preseismic period.

5.4 Discussion and Future Work

The 2007 earthquake location may be the result of delayed dynamic triggering from the large number of earthquakes following the 2000 and 2005 earthquakes. The increased level of seismicity may be associated with the observed aseismic slip transients, as in the case of the afterslip following the 2005 earthquake. More stress modeling is needed to determine whether this observed aseismic slip contributed significantly to the timing and location of the 2007 earthquake.

5.5 Acknowledgments

This work is supported by the National Science Foundation grant EAR 0738299. The GPS data is provided by the Tectonics Observatory, LIPI and SOPAC.

5.6 References

Apel, E., R. Bürgmann, P. Banerjee, and B. Nagarajan, Geodetically constrained Indian Plate motion and implications for plate boundary deformation, *Eos Trans. AGU*, 85(52), Fall Meeting Supplement, T51B-1524, 2006.

Konca, A. O., J. Avouac, A. Sladen, A. J. Meltzner, K. Sieh, P. Fang, Z. Li., J. Galetzka, J. Genrich, M. Chlieh, D. H. Natawidjaja, Y. Bock, E. J. Fielding, C. Ji, and D. V. Helmberger, Partial rupture of a locked patch of the Sumatra megathrust during the 2007 earthquake sequence, *Nature*, 465, 631-635, 2008.

Natawidjaja, D. H., K. Sieh, M. Chlieh, J. Galetzka, B. W. Suwargadi, H. Cheng, R. L. Edwards, J. Avouac, and S. N. Ward, Source parameters of the great Sumatran megathrust earthquakes of 1797 and 1833 inferred from coral microatolls, *J. Geophys. Res.*, 111, 10.1029/2005JB004025, 2006.

Reasenber, P. A. and R. W. Simpson, Response of Regional Seismicity to the Static Stress Change Produced by the Loma Prieta Earthquake, *Science*, 255, 1687-1690, 1992.

Wiemer, S., A software package to analyse seismicity: ZMAP, *Seismol. Res. Lett.*, 72, 373-382, 2001.

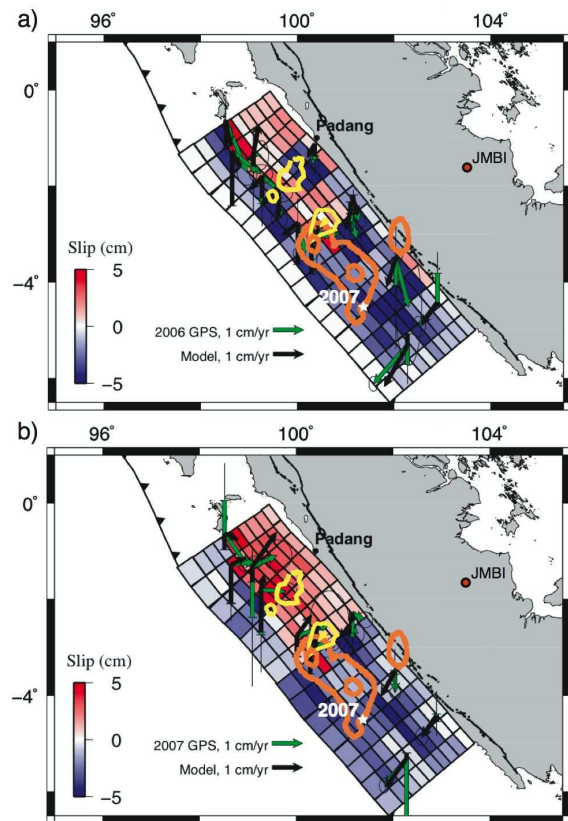


Figure 2.13: Inverted slip on the Sunda megathrust, for a) 2006, and b) 2007 up to September 12th earthquake. Positive slip values indicate stronger coupling and negative slip values indicate aseismic slip on the megathrust. The 1-m and 5-m slip contour lines for the 2007 M_w 8.4 earthquake are shown in orange and for the M_w 7.9 aftershock in yellow (Konca et al., 2008).

6 Moment Moment Tensors for Very Long Period Signals at Etna Volcano, Italy

Margaret Hellweg, Andrea Cannata (INGV, Catania), Stefano Gresta (Universita Catania), Sean Ford, Guiseppe Di Grazia (INGV, Catania)

6.1 Introduction

Very long period signals (VLP, 10 s - 30 s) associated with long period events (0.5 Hz - 5 Hz) were observed at Etna Volcano, Italy, during June-November 2005. They are only recorded at the broadband stations nearest to Etna's craters, ECPN, EBEL, EPDN and EPLC. These stations are part of the permanent seismic network run by the Catania Section of the Istituto Nazionale di Geofisica e Vulcanologia (INGV). Although the signal-to-noise (S/N) ratio for these VLPs is in general only poor to fair, they seem to recur, and can be classified into two families. We improved the S/N by stacking (see 2008 Annual Report), and determined moment tensors for the VLP events using the complete waveform, full moment tensor inversion program (*Minson and Dreger, 2008*).

6.2 Moment Tensor Results

We calculated both deviatoric and full moment tensors for the VLP stacks of Family I and Family II using the complete waveform inversion code described by *Minson and Dreger (2008)* and synthetic Green's functions for very shallow source depths. The velocity model used to calculate the Green's functions described a simple half-space with a P-wave velocity of 2.0 km/s and a S-wave velocity of 1.2 km/s. A suite of moment tensor inversions was performed at grid points (horizontal spacing 0.25 km; depths in km: 0.25, 0.50, 0.75, 1.0, 1.5) within the volcanic edifice (locations shown in Figure 2.14). The origin of the rectangular grid was the centroid of the four summit stations. Etna's topography was not included in the calculation of the Green's functions.

For both families, the moment tensor solutions with the best variance reduction (VR) were in the same region of the edifice as the locations determined for the VLP events using radial semblance (*Cannata, et al., 2009*). For Family I, the best solutions had VR > 70% and were best explained by sources that are 60-70% isotropic (ISO) (Figure 2.14). For Family II, they had VR > 60% and 60-70% ISO. Deviatoric solutions for both families had much poorer VR and waveform fits were clearly less satisfactory.

In moment tensor inversions, the signal to noise ratio (SNR) of the data is clearly important. Fifteen years of experience of moment tensor analysis in California include small events down to M 3.5 and below (*Hellweg et al., 2006*). Although events along the central San Andreas Fault are known to be purely double couple (DC),

deviatoric moment tensor solutions for small events with low SNR in the band of analysis (10 s - 50 s) may have up to 30% of their energy modeled by a compensated linear vector dipole (CLVD) mechanism. For the VLP

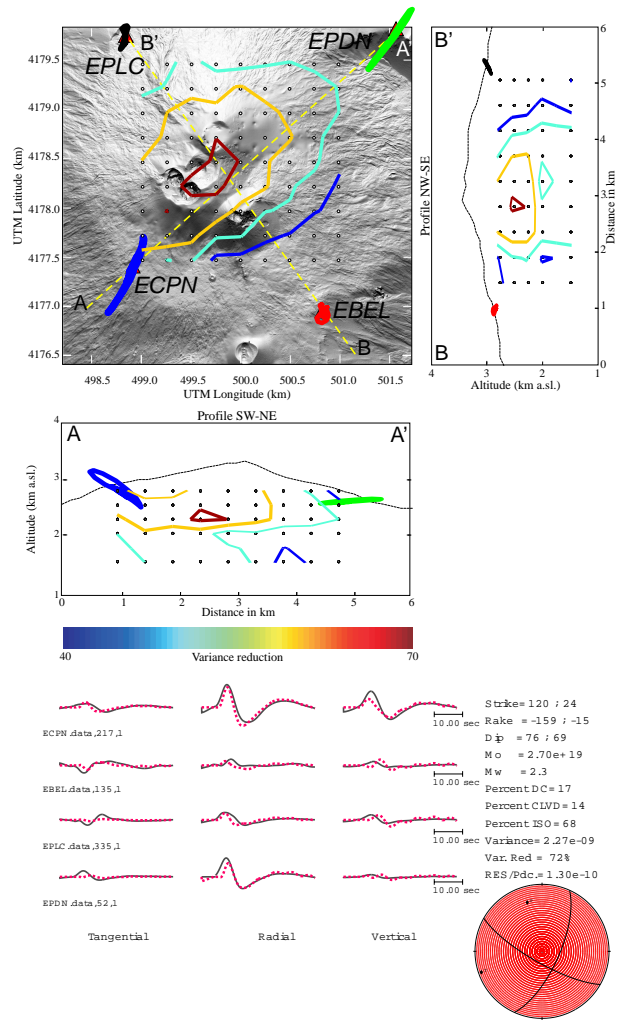


Figure 2.14: Full moment tensor results for Family I events. The map and cross sections show the particle motion at the four summit stations, as well as the search grid and the spatial variation of VR. The source type is plotted on the diamond shaped graph. The bottom panel shows the waveform fits and the mechanism. Note that the amplitudes of the waveforms are scaled so that they can be compared. Results for Family II are very similar.

events of Mt. Etna, even the stacks analysed here, the SNR is low. The DC and CLVD elements of the best solutions vary from grid point to grid point. The eigenvalues describing the deviatoric portions of the solutions also primarily vary randomly in space, with a preference of the largest eigenvector toward a subhorizontal orientation and a slight predominance of SW orientations. Thus, we are convinced that the deviatoric parts of the moment tensor solution are most likely to be efforts of the inversion to explain the noise. They cannot be used to interpret the geometry of the source without better data. There is no reason to suppose that a fit including single-force elements (e.g. *Chouet et al., 2003, Chouet et al., 2005*) would provide greater insight into the source of the VLP events. On “source-type” plots (*Hudson et al., 1989*), it is notable that all of the moment tensor solutions plot somewhere between “explosion” and “opening crack” sources. The scatter gives some sense of the uncertainty in the solutions.

6.3 Perspectives

Using Green’s functions for full moment tensors calculated using a simple half space velocity model, inversions using the algorithm described in *Minson and Dreger (2008)* indicate that a volume change explains a large portion of the waveforms. We intend to follow up with further analysis to investigate the effects of the simple velocity structure, using Green’s functions calculated for the locally used velocity model. We also hope to investigate single source type solutions (i.e. only DC, only CLVD, only ISO), and hope to have longer wavessnippets to improve our understanding of the signal to noise ratio.

6.4 References

Cannata, A., M. Hellweg, G. Di Grazia, S. Ford, S. Alparone, S. Gresta and P. Montalto, Long Period and Very Long Period events at Mt. Etna volcano: characteristics, variability and causality, and implications for their sources, *J. Volcanol. Geotherm. Res.*, in press, 2009.

Chouet, B., P. Dawson, T. Ohminato, M. Martini, G. Saccorotti, F. Giudicepietro, G. De Luca, G. Milana and R. Scarpa, Source mechanism of explosions at Stromboli Volcano, Italy, determined from moment-tensor inversions of very-long-period data, *J. Geophys. Res.* 108, doi:10.1029/20042JB001919, 2003.

Chouet, B., P. Dawson and A. Arciniega-Ceballos, Source mechanism of Vulcanian dagassing at Popocatepetl Volcano, Mexico, determined from waveform inversions of very long period signals, *J. Geophys. Res.* 110, doi:10.1029/2004JB003524, 2005.

Green, D., and J. Neuberg, Waveform classification of volcanic low-frequency earthquake swarms and its implication at Soufriere Hills Volcano, Monserrat, *J. Volcanol. Geotherm. Res.*, 153, 51-63, 2006.

Hellweg, M., D. Dolenc, L. Gee, D. Templeton, M. Xue, D. Dreger and B. Romanowicz, Twelve Years and Counting: Regional Moment Tensors in and around Northern California *Seismol. Res. Lett.*, 77(2), 221, 2006.

Hudson, J.A., R.G. Pearce and R.M. Rogers, Source type plot for inversion of the moment tensor, *J. Geophys. Res.*, 9(B1), 765-774, 1989.

Minson, S. and D. Dreger, Stable Inversions for Complete Moment Tensors, in press *Geophys. Journ. Int.*, 2008.

7 Temporal Variations in Crustal Scattering Structure near Parkfield, California, from Receiver Functions

Pascal Audet

7.1 Introduction

The accurate determination of crustal velocity structure in the region surrounding a fault is an essential component in the investigation of fault processes since it yields important information on the composition and state of the crust (e.g. anisotropy, pore-fluid pressure, etc). In addition, temporal variations in crustal architecture (i.e. 4-D imaging) can provide key constraints on the dynamics of faulting. One method that provides accurate point measurements of crustal velocity structure is based on the characterization of the scattering structure beneath a recording station using teleseismic events, i.e. the so-called receiver function method. The technique is based on the deconvolution of the source time function, approximated by the P-wave train, from the S-components of motion. The resulting seismograms represent an approximation to the Earth's Green function, and are used to determine the depth and velocity of discrete crustal layers. A novel use of the receiver function method is proposed here which makes use of decade-long high-quality records from permanent broadband stations to estimate temporal variations in crustal scattering structure.

7.2 4-D imaging using receiver functions

The conventional receiver function method has been applied to data from the Parkfield broadband seismic station PKD, and results demonstrate the existence of a lower crustal, low-velocity layer with strong (~15%) anisotropy (Ozacar and Zandt, 2009). Using 12 years of data at station PKD (~1000 events, Figure 2.15), we calculate the power spectral density (PSD) for each individual, unfiltered receiver function and bin into 12 month-long, 90% overlapping segments within which we calculate the median PSD and total power by integrating the PSD. Results show a clear change in PSD and spectral power after the 2003 M_w 6.5 San Simeon earthquake with a subsequent decrease (~2 dB) in the post-seismic background PSD level (Figure 2.16). Careful investigation of both event distribution and instrument response functions estimated from noise records reveal that the change is not due to uneven source distribution or instrumental bias. Moreover, this change is observed only for events coming from the back-azimuth range 0°-200°(dominated by events originating from South-Central America), which sample the crust along strike and southwest of the San Andreas Fault near Parkfield (Figure 2.15).

Variations in PSD levels do not constrain the depth of

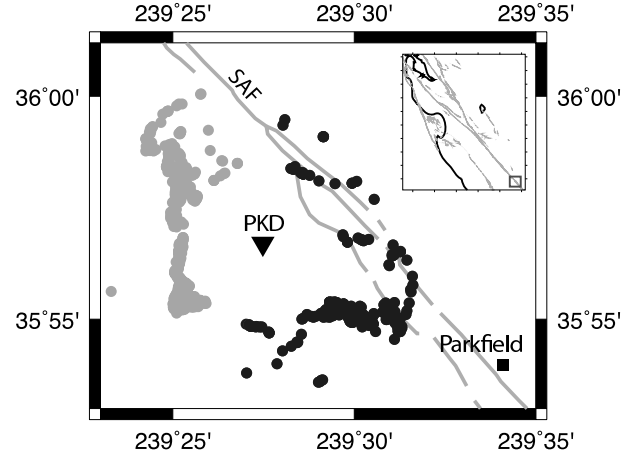


Figure 2.15: Moho piercing points (grey and black dots) of receiver functions around station PKD near Parkfield, California, with respect to study region (inset). Events from eastern azimuths (0°-200°- black dots) sample the crustal structure along the strike of the San Andreas Fault.

this change; however, given its azimuthal dependence, it is unlikely that it originates at shallow levels. Its manifestation at periods of 0.5-3 s where PSD is highest suggests a depth-integrated effect that may be related to crack opening, non-linear damage, or permeability-enhanced pore-fluid flow. Reduced PSD levels imply a decrease in scattering energy from structure, i.e. smaller impedance contrasts across interfaces, which is consistent with redistribution of crustal pore-fluids and the breaking of impermeable barriers due to shaking (i.e. damage). The fact that the Parkfield earthquake did not have a similarly strong effect on the PSD levels may reflect the total re-equilibration of pore-fluid pressures in the crustal column after the San Simeon earthquake.

Such questions may be addressed by complementary methods that provide depth resolution (e.g. time-domain receiver functions, ambient-noise tomography, etc.) and using different data sets. These results are consistent with time-varying crustal S-velocities from ambient noise correlation studies and the coincident modulation of tremor activity near Parkfield following the 2003 San Simeon and 2004 Parkfield earthquakes (Brenquiere et al., 2008). This preliminary study indicates that the receiver function method bears the potential for investigating 4-D faulting processes, albeit only as a diagnostic tool.

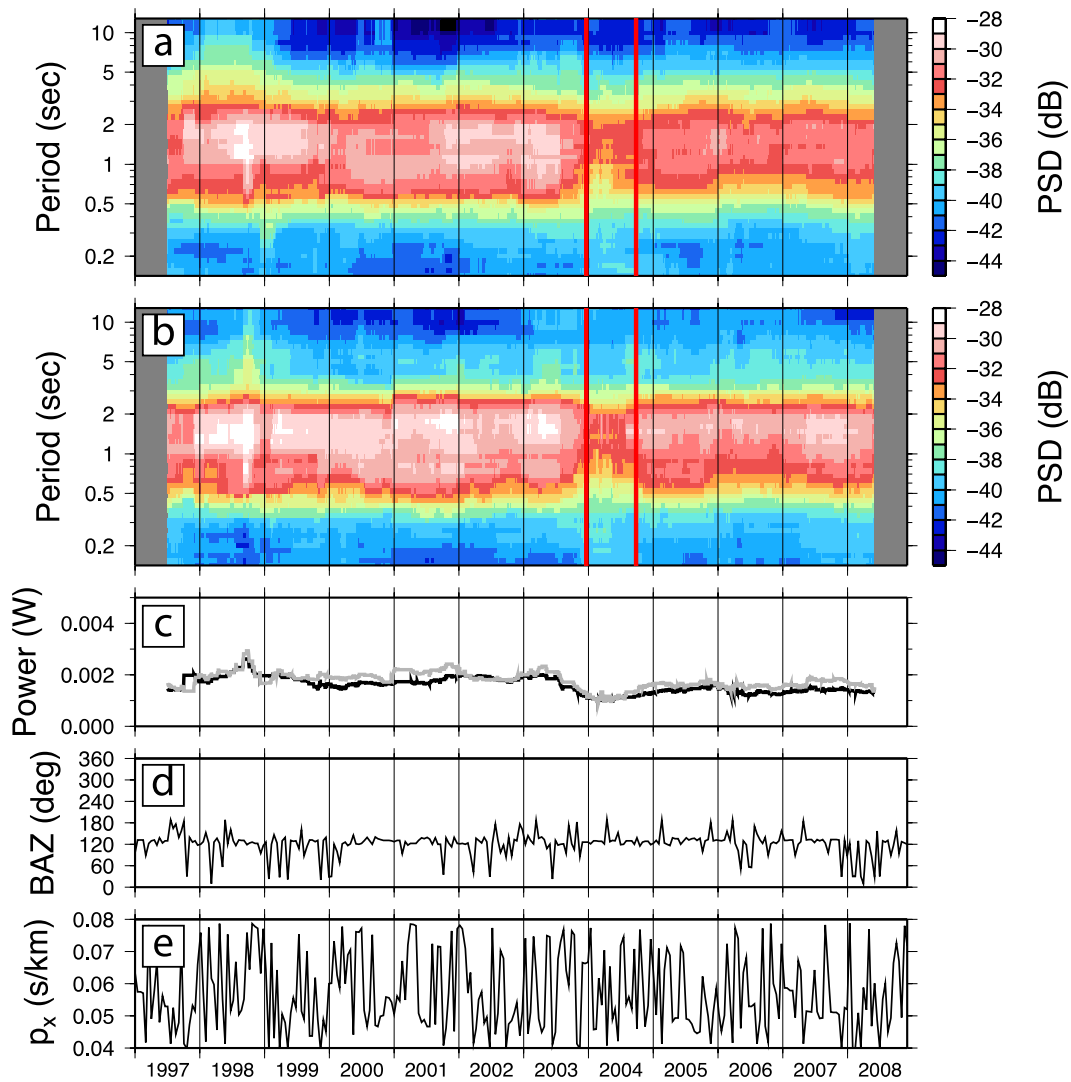


Figure 2.16: Temporal variations in receiver functions at station PKD for back-azimuths 0° - 200° . Top panels show power-spectral density (PSD) of receiver functions binned within 90% overlapping, 12-month windows for radial (a) and transverse (b) components. Panel (c) shows the corresponding variations in total power (black line - radial; grey line - transverse). Distribution of events with respect to back-azimuth and slowness of incoming wave-fields is presented in (d,e). Vertical lines indicate times of the San Simeon (2003) and Parkfield (2004) earthquakes.

7.3 Acknowledgements

This work was funded by the Miller Institute for Basic Research in Science (UC Berkeley).

7.4 References

- Brenguier, F., M. Campillo, C. Hadziioannou, N.M. Shapiro, R.M. Nadeau, and E. Larose, Postseismic relaxation along the San Andreas fault at Parkfield from continuous seismological observations, *Science*, *321*, 1478-1481, 2008.
- Ozacar A. A., and G. Zandt, Crustal structure and seismic anisotropy near the San Andreas fault at Parkfield, California, *Geophys. J. Int.*, in press, 2009.

8 Remote Triggering of Fault-Strength Changes on the San Andreas Fault at Parkfield

Taka'aki Taira, Paul G. Silver (Carnegie Institution of Washington), Fenglin Niu (Rice University), and Robert M. Nadeau

8.1 Introduction

Fault strength is a fundamental property of seismogenic zones, and its temporal changes can increase or decrease the likelihood of failure and the ultimate triggering of seismic events. While changes in fault strength have been suggested to explain various phenomena, such as the remote triggering of seismicity, there has been, to our knowledge, no means of actually monitoring this important property in situ. Here we argue that ~ 20 years of observation (1987-2008) of the Parkfield area at the San Andreas Fault have revealed a means of monitoring fault strength. We have identified a long-term change in fault strength most likely induced by the 2004 M_w 9.1 Sumatra-Andaman earthquake (SM04) (Taira *et al.*, 2009). The change possessed two manifestations: temporal variations in the properties of seismic scatterers - likely reflecting the stress-induced migration of fluids - and systematic temporal variations in the characteristics of repeating-earthquake sequences that are most consistent with changes in fault strength.

8.2 Fault-Strength Change

The time-varying properties of seismic scatterers have recently been used to probe stress-induced changes in the San Andreas Fault zone near Parkfield in central California (Niu *et al.*, 2003; Taira *et al.*, 2008). As a measure of temporal scatterer behavior from one earthquake to the next, we use the decorrelation index $D(t)=1-C_{\max}(t)$ derived from the cross correlation of two seismograms, where $C_{\max}(t)$ is the maximum cross correlation (Niu *et al.*, 2003). Using tightly-clustered repeating microearthquakes (Nadeau and McEvilly, 1999) recorded by the High-Resolution Seismic Network (Figure 2.17a), we have been able to track the behavior of a group of time-dependent scatterers (the target scatterer) that was first identified by Niu *et al.* (2003), for a 22-year period (1987-2008) (Figure 2.17b). The target scatterer has been interpreted as fluid-filled fractures, and their temporal variations as due to the stress-induced migration of fluids near the target scatterer.

There are three excursions in $D(t)$. The 1st excursion is coincident with the 1993 Parkfield Aseismic Transient (PAT93). It initiated around 1993 (Figure 2.17b), peaked in the mid 1990s and slowly decayed over about a subsequent ~ 7 -year period. The 2nd excursion (September 2004) is associated with the 2004 Parkfield earthquake (PK04) (Figure 2.17c) and decayed back to the pre-earthquake level after about 2-3 months. The 3rd ex-

cursion in $D(t)$ occurred about three months after the 2004 Parkfield earthquake (Figure 2.17c). The magnitude of change in $D(t)$ is comparable to that observed for the other two transients. The increase in $D(t)$ takes place over three months, after which time $D(t)$ decays slowly over a subsequent ~ 1 year period (Figure 2.17c).

There are also changes in repeating-earthquake properties that accompany this 3rd excursion in $D(t)$. Following the 2004 Parkfield earthquake, there is a characteristic increase in recurrence interval T_r as is typically observed postseismically. This trend, however, is interrupted roughly three months after the 2004 Parkfield earthquake. In 6 of the available 13 sequences, there is a systematic reduction in T_r that reaches a minimum about 6 months after the 2004 Parkfield earthquake. To explore this apparent disruption further, we removed the post-seismic effect by the 2004 Parkfield earthquake, assuming Omori's law, $T_r(t)=at^p$ where t is time after the earthquake and a and p are constants to be estimated, and computed the residual recurrence interval $\hat{T}_r(t)=T_r(t)/(at^p)$.

Using all available sequences, we find that the log of the residuals increases by roughly a factor of 2 beginning three months after the 2004 Parkfield earthquake. This increased variability suggests an additional perturbation to T_r and a temporal change in the mechanical properties of the fault. An interesting feature of this variability is that there is a positive correlation between \hat{T}_r and seismic moment M_0 (Figure 2.17d). Such a correlation is consistent with a slip-predictable model for earthquake occurrence (Shimazaki and Nakata, 1980), where the stress drop and T_r are both determined by the failure strength of the fault for constant loading rate and constant minimum stress. Assuming rupture area is constant among members of a repeating-earthquake sequence (Nadeau and Johnson, 1998), then fault slip will be proportional to M_0 which should in turn be proportional to stress drop. The most dramatic correlation that we found is for sequence K3 (5 km depth) (Figure 2.17d). This sequence also has the least variability in event location, so that the assumption of constant fault area should be the most valid. A reduction in \hat{T}_r (and M_0) around 6 months after the 2004 Parkfield earthquake indicates a temporary weakening of the fault.

We have localized the onset time of the 3rd excursion in $D(t)$, utilizing all of the repeating-earthquake sequences that displayed a change in $D(t)$. We find that the excursion must have initiated between December 21 (se-

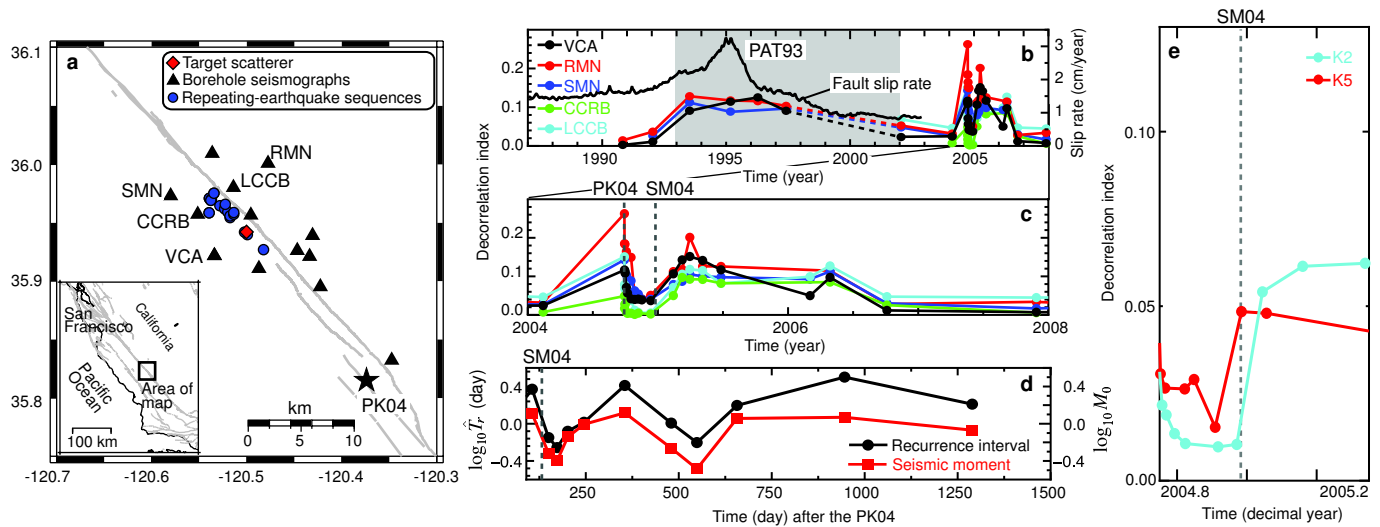


Figure 2.17: (a) Map view of the study area. $D(t)$ for sequence K3 during (b) 1987-2008 and (c) 2004-2008. (d) \hat{T}_r and M_0 normalized by its average for sequence K3. (e) Average $D(t)$ using the lowest-noise stations VCA, LCCB, and CCRB, for sequences K2 and K5.

quence K2) and December 26, 2004 (sequence K5) (Figure 2.17e). The most dramatic tectonic event to occur within the 5-day time window is the 26 December 2004 M_w 9.1 Sumatra-Andaman earthquake, whose origin time is 7 hours before the end of the interval. The timing strongly suggests that the dynamic stresses from this earthquake, estimated to be about 10 kPa [based on the amplitude of long period surface waves (>30 s) which are likely to have the strongest impact on fluid flow], induced fluid flow that caused both a structural change in the fault zone region [i.e. changes in $D(t)$] and, through variations in pore pressure, consequent changes in the strength of the fault. It is now well documented that such dynamic stresses are capable of remotely triggering seismicity. The present study suggests that these same dynamic stresses can actually produce long-term (~ 1 year for our study) changes in fault strength.

8.3 Conclusions

We showed that temporal changes in seismic scatterer properties and characteristics (frequency and magnitude) of repeating microearthquakes constitute a proxy for changes in fault strength, proposing that they provide a means of continually monitoring fault zone strength which is an important parameter in assessing earthquake potential of a fault.

8.4 Acknowledgements

The present study was supported by the National Science Foundation EAR-0337308, EAR-0408947, EAR-0409024, EAR-0453638, EAR-0537641, EAR-0544730,

and DTM-2025-01 and by the Department of Terrestrial Magnetism, Carnegie Institution of Washington. The Parkfield High-Resolution Seismic Network is operated by University of California, Berkeley Seismological Laboratory with financial support from the U.S. Geological Survey through National Earthquake Hazards Reduction Program award 07HQAG0014.

8.5 References

- Nadeau, R.M. and L.R. Johnson, Seismological studies at Parkfield VI: Moment release rates and estimates of source parameters for small repeating earthquakes, *Bull. Seismol. Soc. Am.*, *88*, 790-814, 1998.
- Nadeau, R.M. and T.V. McEvilly, Fault slip rates at depth from recurrence intervals of repeating microearthquakes, *Science*, *285*, 718-721, 1999.
- Niu, F., P.G. Silver, R.M. Nadeau, and T.V. McEvilly, Migration of seismic scatterers associated with the 1993 Parkfield aseismic transient event, *Nature*, *426*, 544-548, 2003.
- Shimazaki, K. and T. Nakata, Time-predictable recurrence model for large earthquakes, *Geophys. Res. Lett.*, *7*, 279-282, 1980.
- Taira, T., P.G. Silver, F. Niu, and R.M. Nadeau, Detecting seismogenic stress evolution and constraining fault zone rheology in the San Andreas Fault following the 2004 Parkfield earthquake, *J. Geophys. Res.*, *113*, B03303, doi:10.1029/2007JB005151, 2008.
- Taira, T., P.G. Silver, F. Niu, and R.M. Nadeau, Remote triggering of fault-strength changes on the San Andreas Fault at Parkfield, *Nature*, doi:10.1038/nature08395, 2009 (accepted for publication).

9 Source Analysis of the Memorial Day Explosion, Kimchaek, North Korea

Douglas Dreger, Sean Ford (LLNL), William Walter (LLNL)

9.1 Introduction

The Democratic People’s Republic of Korea (DPRK) announced it conducted a second nuclear test on 25 May 2009. Within hours of the test, and before the official DPRK announcement, several organizations, including the U.S. Geological Survey National Earthquake Information Center and the Comprehensive Test Ban Treaty Organization (CTBTO), reported a seismic signal in the magnitude range 4.5 to 4.7 near the vicinity of the 2006 DPRK nuclear test (CTBTO Press Centre, 2009a). However, the International Monitoring System of the CTBTO did not detect radioactive noble gases that would confirm the test of a nuclear-device (Clery, 2009).

In our previous work (Ford *et al.*, 2009a) we showed it was possible to identify explosions at the Nevada Test Site with a full moment tensor inversion of seismic waveforms from nearby stations in the Western US. In this contribution, we show that the best-fit source for the

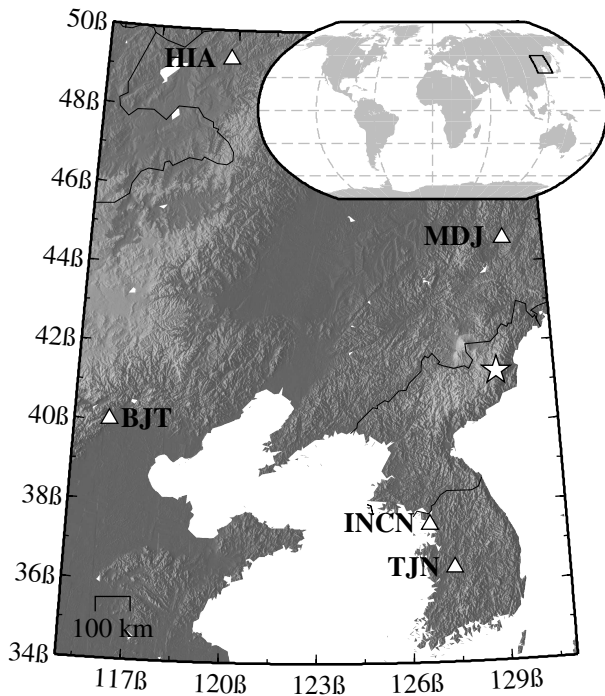


Figure 2.18: Map of the Yellow Sea / Korean Peninsula region. The North Korea explosion is identified with a star and the stations with triangles. The region is outlined in the global inset map.

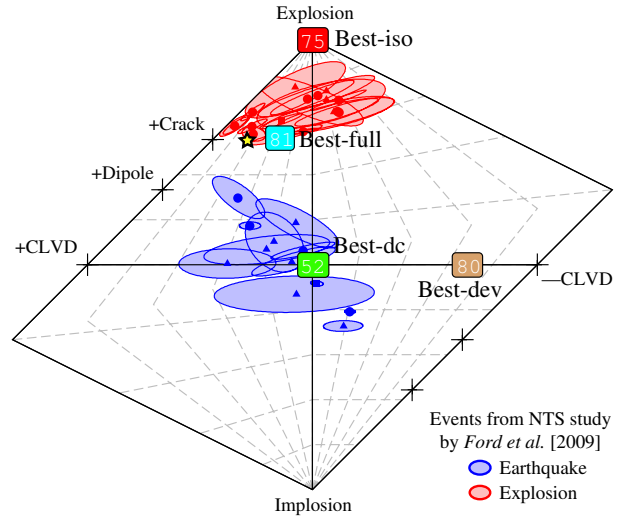


Figure 2.19: Source-type plot with various solutions and their associated fit percent. Note that the Best-DC solution is at the center ($[\epsilon, k] = [0, 0]$) and the Best-dev solution is along the abscissa ($k = 0$). Also plotted are results for explosions at the Nevada Test Site (NTS) from Ford *et al.* [2009a] with their associated 95% error ellipses. Error ellipses for the North Korea test are smaller than the plotted symbol.

2009 Memorial Day event near Kimchaek, North Korea is dominantly isotropic, which is consistent with an explosion. A more detailed description of this work is found in Ford *et al.* (2009b)

9.2 Results

Three component waveform data from Global Seismograph Network (GSN) and China Digital Seismograph Network (CDSN) stations MDJ, INCN, BJT and HIA along with station TJN from the Ocean Hemisphere Project Seismological Network (Figure 2.18) are instrument corrected, integrated to displacement, and band-pass filtered using an 6th order acausal Butterworth filter with corners at 0.02 and 0.10 Hz. Green’s functions were computed using a model appropriate for the region. The Green’s functions were aligned with the data based on a location and origin time of 00:54:43.38, 25 May 09, 41.2986°/129.0694° (D. Dodge, unpublished data, 2009), and timing shifts of less than 5 seconds (maximum half-cycle recommended by Ford *et al.* (2009a))

were employed to maximize the fit to the data. A source depth of 600m was initially assumed. Explosion, earthquake (double-couple or DC), deviatoric, and full moment tensor solutions were evaluated. The explosion and DC solutions were obtained with a grid-search to find the best-fitting parameters, whereas the deviatoric and full moment tensor solutions were calculated with a least-squares linear inversion.

As Figure 2.19 shows, the pure explosion model fits the data with a variance reduction of 75% and yields an isotropic moment of 1.8×10^{22} dyne-cm ($M_w 4.1$; all seismic moment values are calculated with the method of *Bowers and Hudson (1999)*). In contrast, the pure DC earthquake solution fits the data much worse at 52% with $M_0 = 3.8 \times 10^{22}$ dyne-cm ($M_w 4.4$). The fact that the single degree of freedom explosion model fits so much better than the four degree of freedom DC model is highly significant and indicates that such a comparison can be a useful discriminant. The strike, rake, and dip of the best-fit DC is 50° , -85° , and 10° , respectively. Such a steep dip-slip mechanism is unusual for an earthquake. Of all sources calculated by the Global CMT Project (<http://www.globalcmt.org/>) less than 1.6% have dips of less than 10° . This type of information may be used as an additional indication of anomalous sources. The DC overpredicts the Love wave amplitude on the transverse components at almost all stations and underpredicts the Rayleigh wave amplitudes, especially at station INCN. The pure explosion does not produce Love waves, and therefore the actual source is a composite.

The full moment tensor inversion fits the data at 81% and yields an isotropic moment of 3.6×10^{22} dyne-cm, and a total moment of 6.3×10^{22} dyne-cm ($M_w 4.5$). The deviatoric moment tensor inversion fits the data at 80% and a total moment of 3.2×10^{22} dyne-cm ($M_w 4.3$). If the deviatoric source is decomposed to a compensated linear vector dipole (CLVD) and DC sharing the same principal axes, then the source is 70% CLVD. The similarity in fits between the dominantly CLVD deviatoric source and dominantly isotropic full moment tensor shows that at shallow depths, a vertical CLVD mechanism can effectively mimic an explosion at the distances and periods analyzed here. The full moment tensor isotropic moment is two times larger than the pure explosion, indicating that the compound source of the full moment tensor solution (DC+CLVD+Isotropic) required to fit the Love waves also modifies the Rayleigh waves, causing the isotropic component to increase in order to compensate.

The best-fitting sources are far from the center, indicating that the source is anomalously non-DC (Figure 2.19). Along with the best-fitting sources the solutions and their 95% error ellipses for explosions at the Nevada Test Site (NTS) and earthquakes in the Western US from *Ford et al. (2009a)* are also plotted. The best-fit full moment tensor plots in the same region as the explosions,

close to the solution for the 2006 North Korean test, and away from the earthquake population. The error ellipses for the best-fit sources from this study are all smaller than the symbol used to plot the solutions due to the very high signal-to-noise of the event records.

Unlike earthquake inversions, the isotropic radiation of a predominantly explosive source does not allow constraint of the source depth by comparing fits at different depths at the frequencies examined here (e.g. *Ford et al., 2009a*). Event locations put the source at less than 1 km, so the results discussed above assume a source depth of 600 m. *Ford et al., (2009b)* examines the sensitivity of isotropic moment with source depth

9.3 Conclusions

Modeling of low-frequency, regional distance waveforms identifies the Memorial Day event in Kimchaek, North Korea as decidedly non-tectonic with the best-fit model dominated by an explosion source. While the source type is well determined to be non-DC, the isotropic moment of the full moment tensor inversion has some uncertainty and the M_w is between 4.4 and 4.6. Comparison of pure explosion and pure double-couple models indicate that the simpler explosion model fits the waveform data substantially better than the higher degree of freedom DC model, where the isotropic moment of the explosion model is 1.8×10^{22} dyne-cm ($M_w 4.1$). However, there are Love waves observed at several stations indicating that the source must have some non-isotropic component. Possible causes of the tangential displacement are additional tectonic sources, tensile failure at depth, and anisotropic propagation.

9.4 Acknowledgements

This research was supported by the National Nuclear Security Administration, contract DE-FC52-06NA27324.

9.5 References

- Bowers, D., and J. A. Hudson, Defining the scalar moment of a seismic source with a general moment tensor, *Bull. Seism. Soc. Am.*, 89(5), 1390-1394, 1999.
- Clery, D., Test ban monitoring: No place to hide, *Science*, 325, 382-385, 2009.
- CTBTO Press Centre, Next phase in the analysis of the announced DPRK nuclear test, Press Release 27 May 09, 2009a.
- Ford, S. R., D. S. Dreger and W. R. Walter, Identifying isotropic events using a regional moment tensor inversion, *J. Geophys. Res.*, 114, B01306, doi:10.1029/2008JB005743, 2009a.
- Ford, S. R., D. S. Dreger and W. R. Walter, Source Analysis of the Memorial Day Explosion, Kimchaek, North Korea, *in press Geophys. Res. Lett.*, 2009b.
- Hudson, J. A., R. G. Pearce, and R. M. Rogers, Source type plot for inversion of the moment tensor, *J. Geophys. Res.*, 94, 765-774, doi:10.1029/JB094iB01p00765, 1989.

10 Towards a continuous seismic wavefield scanning

Aur lie Guilhem, Doug S. Dreger and Bob Uhrhammer

10.1 Introduction

The Mendocino Triple Junction (MTJ) region is tectonically very complex, and as a result it is the seismically most active region of Northern California, with earthquakes (including potential large earthquakes $M > 7$) occurring on the Mendocino Transform Fault, along the Cascadia subduction zone, and in the offshore Gorda/Juan de Fuca plate. In addition to typical intra- and inter- plate seismic events, a variety of anomalous seismic events, including repeating earthquakes, slow/low-stress-drop earthquakes, and nonvolcanic tremors, are observed. In order to more effectively monitor the offshore region, we implement an automatic scanning of the continuous long-period (> 10 sec) broadband seismic records to continuously detect, locate and determine moment tensors of events within minutes following their occurrence. Because the analysis will be done every two seconds, this scanning offers the possibility of rapidly identifying any large damaging and potentially tsunamigenic events.

10.2 Method

We follow the algorithm proposed by Kawakatsu (1998) and used in Japan by Tsuruoka *et al.*, 2009. A seismogram d recorded at a station k can be represented as the convolution of the response of the medium to an impulsive source G with the moment tensor elements m for a source s : $\sum_i G_i^{sk}(t)m_i^s = d^k(t)$ (1). The normal equation based on (1) is given by: $\sum_i A_{ji}^s m_i^s = b_j^s$ (2). A is a square matrix and the least-squares solution of the moment tensor \hat{m} is then given by: $\hat{m} = A^{-1}b$ (3). The moment tensor m can be obtained by a simple matrix multiplication once b is calculated. The variance reduction (VR) obtained from the residual between data and synthetic seismograms is used to evaluate the fit for each calculation.

This analysis is performed over a grid search between 40.0° and 43.0° latitude (0.2° interval), -128° and -123° longitude (0.2° interval), and 5 to 38 km depth (3km interval) (Figure 2.20). For each point of the grid, a moment tensor is generated every two seconds, using 380 sec of broadband velocity seismograms filtered between 20 and 50 sec from four stations of the Berkeley Digital Seismic Network (BDSN) - HUMO, ORV, WDC, and YBH - and a previously generated catalog of Green's functions. The best calculated VR gives the preferred solution for an event.

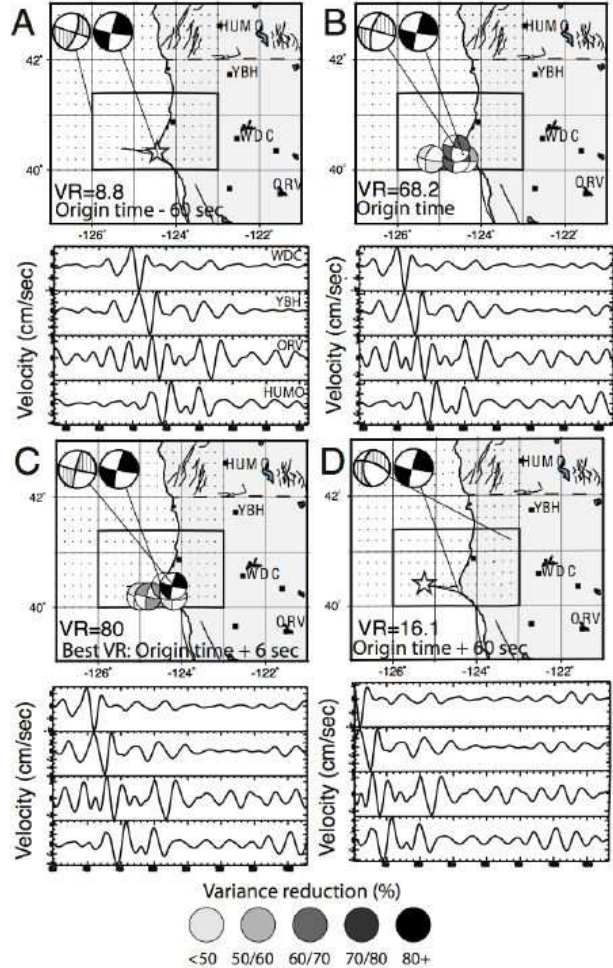


Figure 2.20: Preliminary test for a $M_w 5.0$ earthquake in the MTJ. The large dashed beach ball diagram represents the best mechanism (largest VR indicated on the map) determined for each window, and the large black one shows the reference solution from the Berkeley Moment Tensor catalog. The smaller beach ball diagrams represent the solutions obtained for each time period. The waveforms (vertical velocity seismograms) show the data used in the computation for each time window. A) Analysis performed for 380 sec starting 60 sec before the original time. B) Data starts at the origin time (ANSS catalog) of the earthquake. C) Best time given by the best VR computed for the grid search (here 6 sec after the ANSS catalog time). D) Window starts 60 sec after the origin time.

10.3 Preliminary results

We performed preliminary tests of the continuous seismic scanning using different magnitude earthquakes (from M_w 4.2 to M_w 7.2) located in the study region (Figure 2.20). We centered the grid search around the origin time of the events (about 90 sec before and 60 after), and we reduced the grid search to increase the computational timing of the calculations. For the five studied earthquakes we are able to retrieve their characteristics (origin time, location, magnitude, and mechanism) by searching for the maximum VR (between 69 and 80% agreement between data and synthetics). Additional tests have been performed for periods of seismic noise and teleseismic wave arrivals to evaluate the response of the designed technique when no event was generated in the study region.

Also, because the Mendocino region lies in the southernmost part of the Cascadia subduction zone, which is capable of great and potentially tsunamigenic earthquakes, we performed a synthetic test for a M_w 8.2 reverse earthquake along the trench. We simulated synthetic waveform data for the four stations, filtered between 100 and 200 sec period. 480 sec were inverted, beginning 50 sec before the origin time and ending 50 sec afterward, and the best VR was determined for each point of the grid. Such a multi point-source inversion gives promising results for large earthquakes and can be employed in parallel to the single point-source analysis.

10.4 Implementation of the continuous scanning

The preliminary tests utilized archived seismic data rather than the realtime data that will be processed when the system is in service. We plan to use HH and HL channels (80 sps to 100 sps) from the four stations, decimated to 1 sps and filtered between 20-50 sec and 100-200 sec. Tests of the recursive filters, computed in only a fraction of a second for the 12 channels simultaneously, have been done, and they show very good agreement with similar filters computed in SAC. Also, because a realtime system might mean a lack of incoming data, we performed a jack-knife test to measure the effects of missing channels on the stability of the moment tensor solution for a M_w 5.0 earthquake (Figure 2.21). The mechanism and magnitude of an earthquake are stable. However the VR may change by tens of percentage points, which may result in the non detection of an event if the threshold is set at 65%. Also, missing two or three channels from different stations can worsen the result compared to missing one or two stations, especially if those missing channels contained most of the energy of the earthquake. As a result, we intend to remove all stations with missing channels from the computation and account for missing stations when computing the VR.

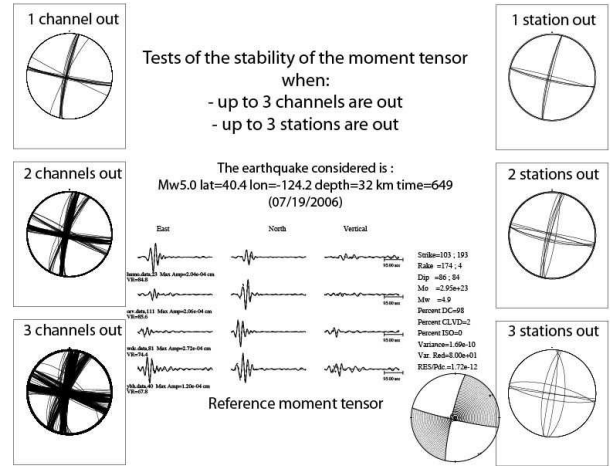


Figure 2.21: Test of the stability of the moment tensor with missing channel(s) and station(s). To symbolize the missing traces, we multiplied the data by zero. The beach ball diagrams on the right and left sides of the figure show the variation in the strikes. The central part of the figure shows the optimal solution obtained with the 12 working channels.

10.5 Conclusions

We are designing a continuous seismic waveform scanning system that will allow the detection, location, and determination of the magnitude and mechanism of any earthquakes of M_w 3.5+ located in the vicinity of the MTJ. The combination of single point-source and multiple point-source inversions by the implementation of two parallel calculations (20-50 sec and 100-200 sec periods) will be useful for the detection of small to great earthquakes in the region. Such realtime monitoring will provide faster results than the currently used procedures. However, HUMO is currently in a triggered mode for the HH and HL channels. We will need to either obtain continuous datastreams or consider replacing it with another seismic station. Finally, the MTJ region is also known for the occurrence of unusual seismicity, in particular for slow/low-stress-drop earthquakes, and such a technique considering long period data may then help in the search for these unusual earthquakes.

10.6 References

- Kawakatsu, H., On the realtime monitoring of the long-period seismic wavefield, *Bull. Earthquake Res. Inst.*, 73, 267-274, 1998.
- Tsuruoka, H., H. Kawakatsu, and T. Urabe, GRiD MT (grid-based real-time determination of moment tensors) monitoring the long-period seismic wavefield, *Phys. Earth Plan. Int.*, 175, 8-16, 2009.

11 The rupture process of the Parkfield SAFOD target earthquakes obtained from the empirical Greens function waveform inversion method

Ahyi Kim, Douglas Dreger, and Taka'aki Taira

11.1 Introduction

Nadeau et al. (1995) found that the seismicity on the San Andreas fault at Parkfield is highly clustered and individual clusters consist of sequences of near periodically repeating small earthquakes of similar seismic moment. *Nadeau and Johnston* (1998) studied the moments, slip rate, and recurrence intervals of these repeating earthquakes, and found that the stress drop of small earthquakes is quite high and, remarkably, increases with decreasing seismic moment. For example, for one of the SAFOD target M2.1 (*Hickman et al.*, 2004) earthquakes, the relationship developed by *Nadeau and Johnston* (1998) yields a stress drop of 100 MPa (correcting for a rigidity of 12 GPa for hypocentral depth of 2.1 km; e.g. *Dreger et al.*, 2007). On the other hand, a spectral corner frequency method yields an average stress drop for the same earthquake of 8.9-22.1 MPa (*Imanishi et al.* 2004; *Imanishi and Ellsworth*, 2006). Recently, *Dreger et al.* (2007) investigated the rupture processes of a sequence of repeating M2.1 SAFOD target earthquakes using the eGf deconvolution method. In that study, they found that peak stress drops between 66.7-93.9 MPa. We applied an eGf waveform inversion method to the M_w 2.1 repeating earthquakes and compared rupture process models, static stress drop distributions, and waveform fits with those from the eGf deconvolution method.

11.2 Method

Inspired by *Hartzell et al.* (1978), we directly inverted observed seismograms using the linear least-squares method of *Hartzell and Heaton* (1983) in which the finite-source is discretized with a finite distribution of point sources in both space and time instead of inverting deconvolved moment rate functions. In this method, the point sources are triggered by the passage of a circular rupture front. The Greens function from each subfault to station is defined by the waveform of a small earthquake, or eGf, located near the hypocenter of each subfault. One advantage of this method is that propagation differences over the fault are better represented for each station. The observed seismogram at location x for the main event, U , is expressed by the discrete form of the general representation theorem:

$$U(x, t) = \sum_{k=1}^K \mu_k A_k u_k \cdot eGf(x, x_k, t + \delta t_k)$$

where x_k is the location of subfault. A_k, μ_k , and u_k are subfault area, rigidity, and slip for the k th subfault of a total of K subfaults. The phase delay term includes

both the delay due to rupture propagation and the travel time difference between the eGf hypocenter and the subfault. We assume that each eGf has the same mechanism as the main event, an acceptable approximation for small earthquakes. The variation of mechanism in the main shock can also potentially be accounted for if eGfs are well distributed over the fault plane. For our San Andreas fault applications, the focal mechanisms of events vary little over a wide range of magnitudes (*Thurber et al.*, 2006). To stabilize the inversion, we employed a slip positivity constraint using the non-negative, least-squares routine of *Lawson and Hanson* (1974), as well as spatial smoothing. The weight of the smoothing constraint was determined by trial and error by finding the smallest value that produced a smoothed model with close to the maximum fit to the data measured by the variance reduction,

$$VR = \left[1 - \frac{\sum_i (d_i - s_i)^2}{\sum_i d_i^2} \right] \times 100$$

where d_i and s_i represent the data and synthetic time series, respectively. The subscript i is an index over station, component, and time. The size of the subfault was chosen to produce a temporally smooth kinematic process with respect to the sample rate of the data.

11.3 Computational setup

We used three-component velocity waveforms recorded at five of the Berkeley Seismological Laboratory's High Resolution borehole Seismic Network (HRSN) stations to examine the rupture processes of the same 5 repeating earthquakes studied by *Dreger et al.* (2007). We also performed eGf deconvolution inversions using the 5 stations, to allow comparison with our waveform inversion results. Locations of repeating earthquakes and stations are shown in Figure 2.22. For the inversion, we used the same fault parametrization as *Dreger et al.* (2007), a $150 \times 150 m^2$ fault decomposed into 31 by 31 square subfaults of $4.8 \times 4.8 m^2$. The strike, dip, and rake are 137, 90, and 180, respectively. The records from HRSN are sampled at 250 sps, which gives an effective bandwidth of 100 Hz. The subfault size is consistent with approximately a quarter of the wavelength of S waves assuming a velocity of 2.3 km/s at 2.1 km depth. We used the same M_w 0.68 event (eGf 1) as *Dreger et al.* (2007)

for the Greens function. eGf 1 is located about 10 m away from the centroid of the target events (Dreger *et al.*, 2007). Since the eGf is a real earthquake, the waveforms contain a rise time which can bias the slip model to be more compact than it actually is. To cancel this effect, we convolved an assumed eGf rise time of 0.008 seconds with the data before performing the inversion. (Dreger *et al.* (2007)).

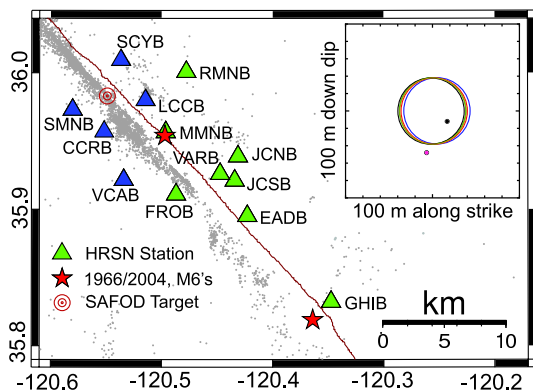


Figure 2.22: Map showing the HRSN station locations (blue triangles are the stations used in this study) and SAFOD repeating target events (star). The inset shows the cross-sectional view of the relative locations of the five studied M2.1 repeating events (larger colored circles), and M_w 0.68 eGf 1 (red dot) and M_w 0.64 eGf 6 (blue dot). The size of the circles shows the respective areas of a 100 MPa event. For comparison, the large gray circle shows the inferred area for a 10 MPa event.

11.4 Inversion results and interpretations

As an example of the results, slip model and stress drop distribution are shown for EVT4 in Figure 2.23. Typically, the slip distribution is circular with a diameter of about 50 m, and the average slip of the main asperity is 3.3 -4.0 cm. The peak slip amplitudes were found to be 10-13 cm. Using our spatially variable slip distribution model, we computed the coseismic stress change on the fault plane using the method of Ripperger and Mai (2007) (Figure 2.23). The computed static stress drop distribution shows that the small patch has a peak stress drop of 63.9-89.4 MPa, which is consistent with the values reported by Dreger *et al.* (2007). However, the average stress drop of 5 MPa is consistent with the typical range of between 1-10 MPa. The rupture process of small earthquakes is complicated, just as in large earthquakes, in terms of spatially variable slip. Also, the SAFOD target events appear to occur on a localized fault patch of high strength capable of earthquakes with high stress drop. The very high peak stress drop that is obtained implies that small-dimension, high-strength asperities exist on the San Andreas Fault.

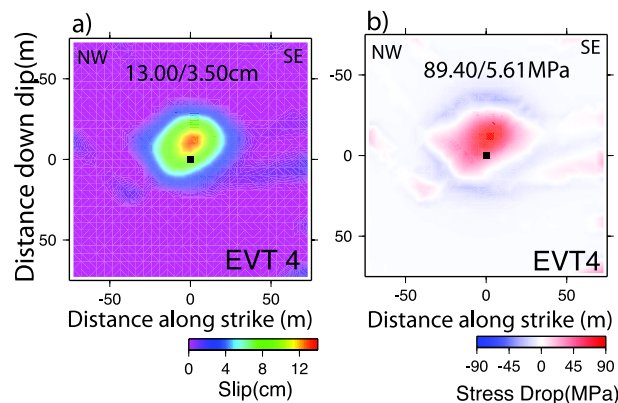


Figure 2.23: Left: Slip model obtained for EVT4. Right: Stress drop distribution for EVT4. For both figures, the number indicates the peak/average slip for each event.

11.5 Acknowledgements

We thank Bob Nadeau for providing the repeating earthquake catalog.

11.6 References

- Dreger, D., R. M. Nadeau, and A. Chung (2007), Repeating earthquake finite source models: Strong asperities revealed on the San Andreas Fault, *Geophys. Res. Lett.*, 34, L23302, doi:10.1029/2007GL031353.
- Hartzell S. H. (1978), Earthquake aftershocks as Green's function, *Geophys. Res. Lett.* 5, 1-4.
- Hickman, S., M. Zoback, and W. Ellsworth (2004), Introduction to special section: Preparing for the San Andreas Fault Observatory at Depth, *Geophys. Res. Lett.*, 31, L12S01, doi:10.1029/2004GL020688.
- Imanishi, K., W. L. Ellsworth, and S. G. Prejean (2004), Earthquake source parameters determined by the SAFOD Pilot Hole seismic array, *Geophys. Res. Lett.*, 31, L12S09, doi:10.1029/2004GL019420.
- Imanishi, K., and W. L. Ellsworth (2006), Source scaling relationships of microearthquakes at Parkfield, CA, determined using the SAFOD pilot hole seismic array, in Earthquakes: Radiated Energy and the Physics of Earthquake Faulting, R. E. Abercrombie, A. McGarr, H. Kanamori and G. Di Toro (Editors), *American Geophysical Monograph* 170, 81-90.
- Lawson, C. L., and R. J. Hanson (1974), Solving Least Squares Problems, Prentice Hall, Englewood Cliffs, New Jersey, 340 pp.
- Nadeau, R. M., W. Foxall, and T. V. McEvilly (1995), Clustering and periodic recurrence of microearthquakes on the San Andreas Fault at Parkfield, California, *Science*, 267, 503-507.
- Nadeau, R. M., and L. R. Johnson (1998), Seismological studies at Parkfield VI: Moment release rates and estimates of source parameters for small repeating earthquakes, *Bull. Seismol. Soc. Am.*, 88, 790-814.
- Ripperger, J., and P.M. Mai (2004), Fast computation of static stress changes on 2D faults from final slip distributions, *Geophys. Res. Lett.*, 31, L18610.
- Thurber, C., H. Zhang, F. Waldhauser, J. Hardebeck, A. Michaels, and D. Eberhart-Phillips (2006), Three-dimensional compressional wavespeed model, earthquake relocations, and focal mechanisms for the Parkfield, California, region, *Bull. Seism. Soc. Am.*, 96, S38-S49.

12 Nonvolcanic Tremor Evolution in the Parkfield, CA Region

Robert M. Nadeau and Aurélie Guilhem

12.1 Introduction

Nonvolcanic tremors have generally been observed in transition zones between freely slipping and locked faults, and in many locations, tremor activity is also seen to increase with detectable transient fault zone deformation (slow-slip events) (*Liu and Rice, 2007*). These associations suggest that tremor activity is closely related to the processes responsible for generating earthquakes. We analyzed tremor activity in the Parkfield region of California between 27 July 2001 and 21 February 2009, during a period when two strong earthquakes occurred in the region: the $6.5M_w$ San Simeon earthquake in 2003 and the $6.0M_w$ Parkfield earthquake in 2004 (Figure 2.24).

12.2 Detection, Size, Location

Using borehole seismic data from the High Resolution Seismic Network (HRSN) at Parkfield, CA, 2198 tremor events (12,547 minutes of activity) were detected during the period (Figure 2.25), with event activity lasting from 3 to nearly 21 minutes. Significant activity also occurred below the detection threshold. The average seismic energy released during the tremors was typically equivalent to a $0.5M_w$ earthquake, and energies ranged over $1.5 M_w$ units. Data from five seismographic networks (BP, BK, NC, CI, and TA) were combined to locate the tremors (Figure 2.25). Approximately 90% of the tremors occurred adjacent to the locked Cholame segment of the San Andreas fault (SAF). An additional 5-10% occurred ~65 km to the northwest in the vicinity of Monarch Peak, CA. Tremors in both zones occurred at between ~15 and 30 km depths.

12.3 Evolution

A sudden increase and subsequent decay of tremor activity (aftertremors) began immediately after the 2003 San Simeon and 2004 Parkfield earthquakes (Figure 2.25A). In addition, approximately 3 weeks before the Parkfield earthquake, an unusually strong episode of activity (foretremor) lasting ~5 days also occurred (*Nadeau and Guilhem, 2009*).

The decay of tremor activity after the Parkfield earthquake continued until mid-2006 when annual rates began again to increase, reaching ~181% of the pre-San Simeon level during the final year of our analysis (Figure 2.25A). Before the Parkfield earthquake, tremor activity in the Monarch Peak tremor zone (Figure 2.24) was low (Figure 2.25B). However, beginning ~10 days after the Parkfield event, activity in this zone increased significantly and

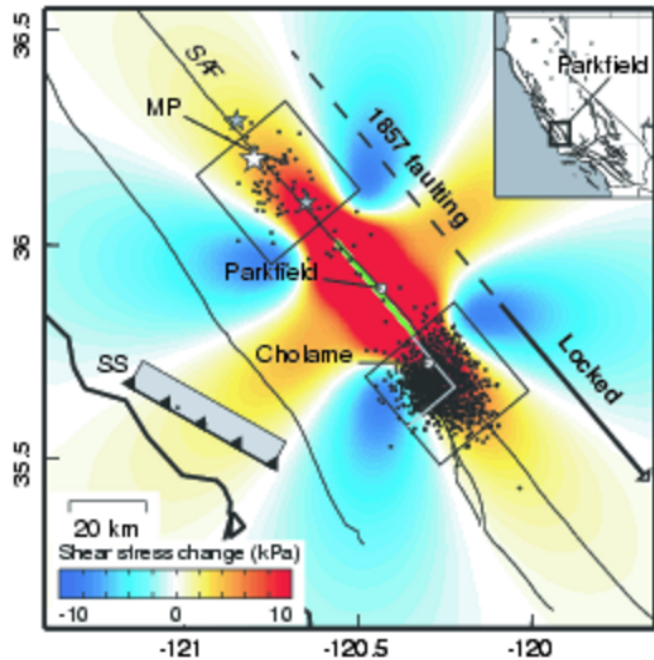


Figure 2.24: Study region with 1250 well-located tremors (black dots). Thirty kilometer square boxes (black) define the Monarch Peak (MP) and Cholame tremor zones. Color contours give regional shear-stress change at 20 km depth from the Parkfield earthquake (green segment) along the San Andreas Fault (SAF). The thrust type San Simeon earthquake rupture is represented by the grey rectangle and hatched line labeled SS. The currently locked Cholame segment is ~63 km long (solid portion of arrow) and is believed capable of rupturing on its own in an ~M7 earthquake. The grey lines within the Cholame box bound the west quadrant where quasi-periodic episodes predominate. White star indicates the epicenter and gray stars the foreshocks of the 1857 Ft. Tejon earthquake.

has continued at an elevated rate. After the Parkfield earthquake, persistent episodes of quasi-periodic tremor also emerged that are reminiscent of episodic tremor observed in some subduction zones (Figure 2.25A) (*Rogers and Dragert, 2003*).

The episodic component of the tremors are most persistent and regular in the western quadrant of the Cholame tremor zone that is bounded by the SAF to the northeast and by the seismic-aseismic transition into the locked Cholame segment to the southeast (Figures 2.24, 2.25C and D). This localization of tremor behavior suggests that there are differences in the process generating tremor

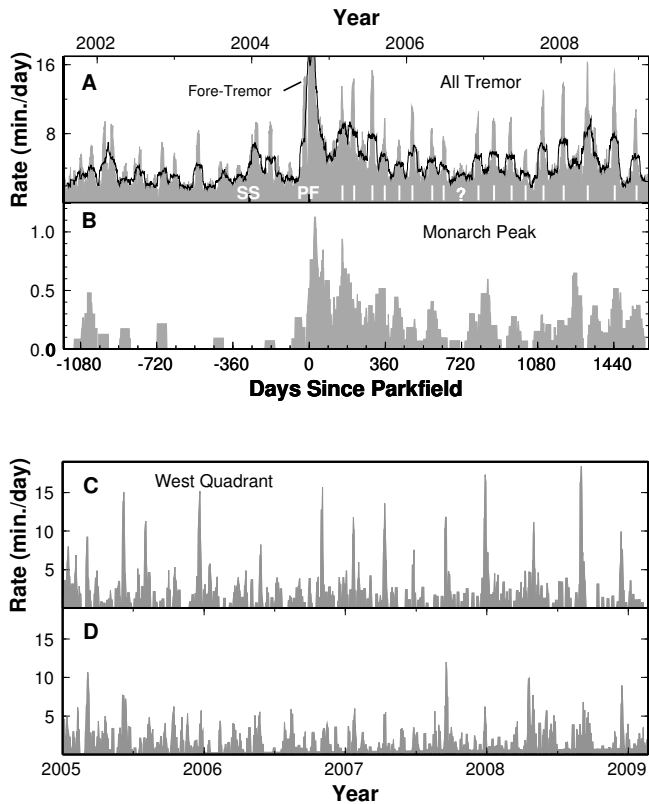


Figure 2.25: Time histories of tremor activity. (A) Fifteen-day (grey) and 45-day (black) smoothed rate histories for all tremors in the study area. Times of the San Simeon and Parkfield earthquakes are SS and PF, respectively. Intense foretremor (Fore-Tremor) activity occurred ~ 3 weeks before PF. Fifteen- and 45-day peak values just after PF are 31.1 and 18.9 minutes/day, respectively. White bars are interpreted times of quasi-periodic episodes. Label ? is time of a weak or missing episode. (B) History of tremor in the Monarch Peak zone (45-day smoothed). (C) History since 2005 of activity (5-day smoothed) in the western quadrant of the Cholame zone (Figure 2.24) (423 tremors; 2835 cumulative minutes of activity) showing strong episodic behavior. (D) Same as (C) for Cholame tremors outside the west quadrant (416 tremors; 2423 cumulative minutes) showing significantly less episodic behavior.

in different subregions of the SAF and that tremor in the Cholame zone is distributed both normal-to and along-strike of the SAF at depth.

12.4 Stress Change

Static Coulomb- and shear-stress changes in the tremor zones from the 2003 San Simeon and 2004 Parkfield earthquakes on SAF aligned planes were small (6 to 14 kPa), but increases in tremor rates correspond with the increases in Coulomb- and shear- stresses. Static normal-

stress changes from the earthquakes do not clearly correspond to the tremor rate changes, suggesting that normal-stress change may not play a significant role in stimulating the SAF tremor. The Coulomb stress changes that stimulated the SAF tremors are roughly an order of magnitude smaller than those typically reported for the triggering of earthquakes (*King et al.*, 1994). This suggests that tremors are a more sensitive indicator of stress change than earthquakes.

12.5 Implications

The periodic tremor and persistent elevated activity after the Parkfield quake are not consistent with expectations of exponentially decaying post-seismic stress after an earthquake (*Savage and Langbein*, 2008). Because the SAF tremor changes have persisted for over 4 years since Parkfield, they could be signaling a shift in the process of deformation and stress accumulation beneath this hazardous portion of the SAF. Faulting from the great M_w 7.8 1857 Ft. Tejon earthquake appears to have propagated from the Monarch Peak area southeastward along the SAF for ~ 350 km, through Parkfield and the Cholame tremor zone (*Topozada et al.*, 2002) (Figure 2.24). The Cholame segment is now fully locked and last ruptured 152 years ago as part of the great 1857 event.

12.6 Acknowledgements

The HRSN is funded by USGS grant 07HQAG0014. Research was supported by USGS grants 06HQGR0167 and 08HQGR0100, and by NSF grants EAR0537641 and EAR0544730.

12.7 References

- King, G.C.P., R.S. Stein and J. Lin, Static Stress Changes and the Triggering of Earthquakes, *Bull. Seism. Soc. Am.*, 84, 935-953, 1994.
- Liu, Y. and J.R. Rice, Spontaneous and triggered aseismic deformation transients in a subduction fault model, *J. Geophys. Res.*, 112, B09404, 2007.
- Nadeau, R.M. and A. Guilhem, Nonvolcanic Tremor Evolution and the San Simeon and Parkfield, California, Earthquakes, *Science*, 325, 191-193, 2009.
- Rogers, G. and H. Dragert, Episodic Tremor and Slip on the Cascadia Subduction Zone: The Chatter of Silent Slip, *Science*, 300, 1942-1943, 2003.
- Savage, J.C. and J. Langbein, Postearthquake relaxation after the 2004 M6 Parkfield, California, earthquake and rate-and-state friction, *J. Geophys. Res.*, 113, B10407, 2008.
- Topozada, T.R., D.M. Branum, M.S. Reichle and C.L. Hallstrom, San Andreas Fault Zone, California: $M \geq 5.5$ Earthquake History, *Bull. Seism. Soc. Am.*, 92, 2555-2601, 2002.

13 Stability of Local and Regional Coda: Application to the Wells, Nevada Sequence

Kevin Mayeda

13.1 Abstract

For this year, we have studied the near-regional Lg-coda from the M_w 6.0 Wells, Nevada earthquake of February 21, 2008 as well as a local M_w 4.2 event from the San Francisco Bay area that exhibited a clear case of source directivity. The Wells event sequence was unique because the U.S. Array broadband seismic deployment had recorded this event along with its aftershocks, thus providing excellent station coverage and redundancy. Figure 2.26 below shows that the local to near-regional coda is very stable in comparison to the direct Lg. We have formed amplitude ratios, in this case 3.5 Hz, between the mainshock and a selected aftershock. The coda velocity and envelope shape functions were found to be virtually identical from station to station, in spite of significant geologic variation for paths traveling east versus those to the north and north-west. Though this event did not exhibit strong directivity (*D. Dreger, pers. comm., 2009*), we still see a radiation pattern in the direct Lg ratios, or perhaps random variation between the two sources. However, for the coda, we see significantly less variation, confirming that the coda is not sensitive to the source mechanism.

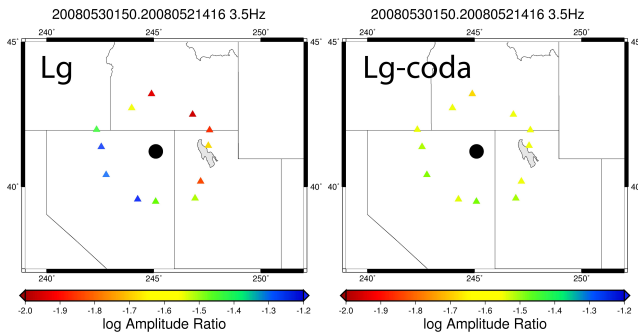


Figure 2.26: Left figure above shows source ratios for Lg at 3.5 Hz for 12 stations surrounding the Wells mainshock region, roughly 200 km in epicentral distance. We observe large variations even though path and site response are removed by forming the source amplitude ratio. In sharp contrast, the right figure shows the coda-derived source ratios for the same event pair and frequency. As found in other studies, the coda is significantly less variable.

For our second example, we studied an M_w 4.2 event that occurred along the Hayward fault in the San Francisco Bay area on July 20, 2007. This event was very

interesting because there were seismic stations equidistant from the mainshock along the strike of the Hayward fault. The mainshock exhibited over a factor of 10 larger amplitude in the north-westerly direction (along strike) relative to the south-east direction. Figure 2.28 shows that station CVS to the north-west has much larger direct wave amplitudes than station MHC to the south-east; however, the coda envelopes are exactly the same after a few tens of seconds. In addition, an aftershock for the same stations and frequency bands does not show any directivity.

13.2 Conclusions

We have documented the coda's property of insensitivity to both the source radiation pattern and directivity. The examples shown in Figures 2.26, 2.27, and 2.28 are strong evidence that the coda's averaging properties also applies to the source heterogeneity, not just path heterogeneity. The recent 2008 M_w 5.8 Wells, Nevada earthquake was well recorded by the U.S. Array, and we show that the local-to-near-regional coda is virtually insensitive to the source radiation pattern and directivity effects. In addition, we demonstrate that the coda wavefield becomes homogenized a few tens of seconds past the expanding direct-wave front.

13.3 References

Mayeda, K., L. Malagnini, W.R. Walter, A new spectral ratio method using narrow band coda envelopes: Evidence for non-self-similarity in the Hector Mine sequence, *Geophys. Res. Lett.*, doi:10.1029/2007GL030041, 2007.

Comparison for 20080521416.20080921316

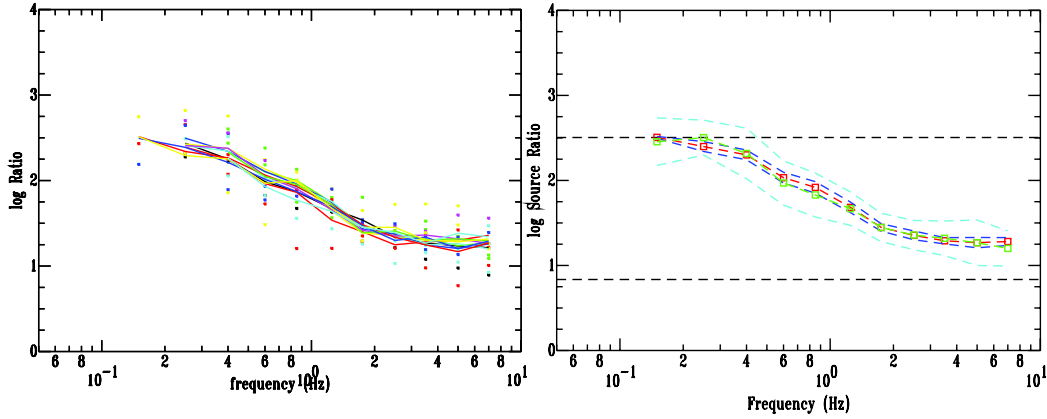


Figure 2.27: Left figure above shows spectral ratios taken between the Wells mainshock and a co-located aftershock. Solid lines represent coda ratios at the 12 stations and colored dots are the direct Lg source ratios. All stations are roughly 200 km in distance. The figure on the right shows the average and standard deviation for both coda and Lg. For the coda, red is the mean and blue is the ± 1 standard deviation and for Lg, green is the mean and light blue is the ± 1 standard deviation. See *Mayeda et al. (2007)* for methodology details.

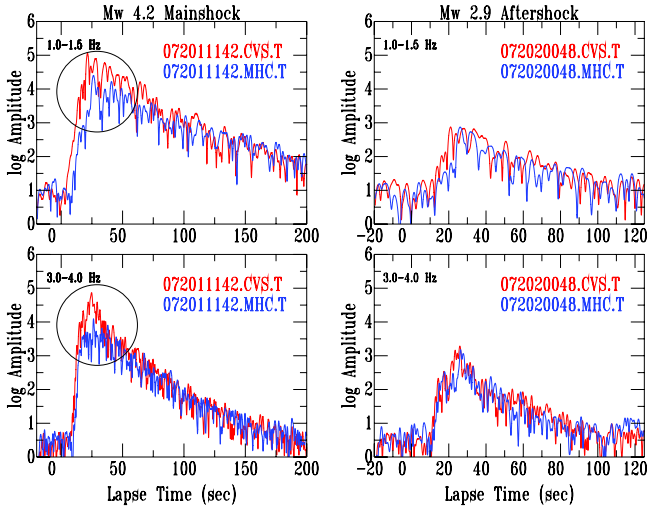


Figure 2.28: We show a clear case of source directivity (left column) that results in roughly a factor or 10 larger amplitude for the direct waves at station CVS, located to the north of the event and along strike relative to station MHC located to the south. However, the coda levels at both stations are identical. An aftershock shows no evidence of directivity (right column).

14 Anomalous Moment Tensor Solutions for The Geysers, CA

Jennifer Taggart, Summer Ohlendorf (UW - Madison), Sean Ford (LLNL), Peggy Hellweg, and Doug Dreger

14.1 Introduction

The Geysers, CA, hosts a Calpine geothermal plant that is an important source of geothermal energy in California. Seismicity in the region is high and has greatly increased in recent years, correlating with geothermal energy production by Calpine. Seismicity is generally shallow, and earthquakes in the region tend to be small ($M_w < 4.5$). The bulk of the seismicity is thought to be induced by geothermal operations. Part of the Clear Lake Volcanic Field, The Geysers appear to have formed in a gap created as the Mendocino Triple Junction migrated north. An underlying pluton forms the geothermal heat source close to the surface.

14.2 Research Objectives

Moment tensor solutions are calculated in real time for most events with $M_w \geq 3.5$ in Northern California (Pasyanos *et al*, 1996, Romanowicz *et al*, 1993) using the waveform moment tensor inversion code developed by Dreger (Minson and Dreger, 2008). Routine moment tensor solutions for The Geysers, computed with pure double couple (DC) and compensated linear vector dipole (CLVD) components (deviatoric solutions), often have a high non DC component. Non DC elements in the solutions to these Geysers events may be real (Dreger *et al*, 2000, Dreger *et al*, 2008, Ford *et al*, 2008), especially for the larger events ($M_w 4+$). A program for full moment tensor inversions, including the isotropic (ISO) component, is available, and large events with a significant non DC component warrant a closer look with this code.

Mechanisms appear to cluster and vary. Some events, mostly in the southeast corner of the region, have solutions with high DC components that appear to reflect strike slip faulting. Others, scattered through the northern part of the region, may have normal faulting. In addition, the moment magnitudes routinely computed with the moment tensor program frequently have a higher M_w than M_L , indicating some difference in the radiated energy from these events that may correspond to a real difference in the events (see map, Figure 2.29).

14.3 Full Moment Tensors at The Geysers

We are reviewing moment tensors for some of the Geysers events. Our first efforts have used two different procedures, discussed here. For six events, Group I, chosen for their occurrence during the USARRAY installation in Northern California (see table), we first gathered all

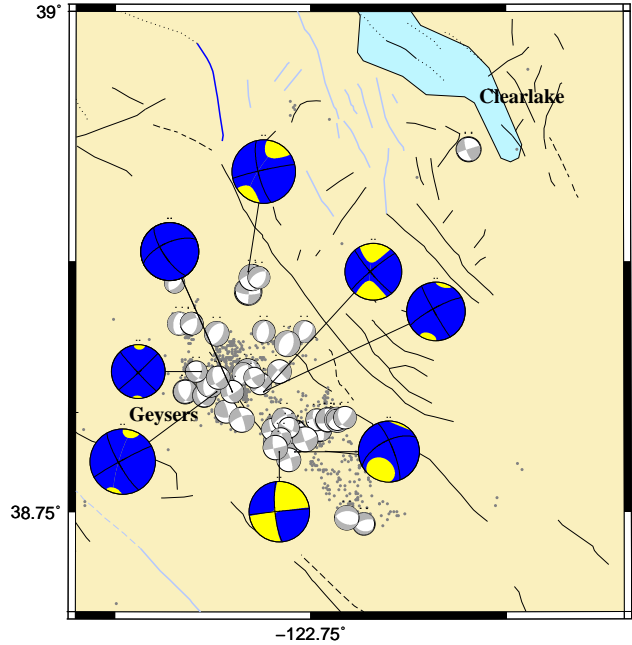


Figure 2.29: The first approach yielded six full moment tensor solutions with significant ISO components, while the second approach yielded one high DC solution and one solution with a significant ISO component. Green's function source depth for Group I is 2 km; for Group II, 5 km. Dark gray dots indicate 2008 background seismicity for The Geysers, while light gray beach balls represent best fit DC solutions from the BSL moment tensor catalog in that region (1990 through January 2009). Black beach balls represent full moment tensors from the two groups.

available low-noise data within 5 degrees of each event and then removed all stations with a best-fit variance reduction of 40% or below. Our best moment tensor solutions used data from between 20 and 60 stations. The large number of stations used provided robust solutions (Ohlendorf, 2008). As Geysers seismicity tends to be shallow, a source depth of 2 km was used. Group II comprised two events with only 46% and 18% respective DC components in the Berkeley Moment Tensor Catalog. Review of Group II events followed the procedure normally used during routine event review at UCB. Final solutions had 11 and 14 stations, respectively.

All six Group I events had best fitting moment tensor solutions with significant non DC components

Date	Location	Type	Stations	DC/CLVD/ISO (percent)	VR (percent)
5/12/2006	38.814 -122.814	Full	65	53/1/46	71.1
10/20/2006	38.867 -122.787	Full	62	44/21/35	69.5
04/30/2007	38.820 -122.823	Full	27	37/15/50	65.6
07/20/2007	38.810 -122.800	Full	24	13/21/66	59.1
12/1/2007	38.733 -122.933	Full	20	18/31/50	65.1
11/17/2005	38.814 -122.782	Full	21	51/25/24	54.7
1/4/2009	38.782 -122.773	Deviatoric	13	61/39/0	80.7
1/4/2009	38.782 -122.773	Full (ISO off)	11	82/18/0	81.6
1/4/2009	38.782 -122.773	Full	11	83/11/5	81.7
5/30/2008	38.776 -122.764	Deviatoric	14	39/61/0	77.9
5/30/2008	38.776 -122.764	Full (ISO off)	14	64/36/0	74.3
5/30/2008	38.776 -122.764	Full	14	20/44/36	75.6

Table 2.2: Top: Full moment tensors at source depth 2 for the Group I events. Bottom: Best solutions at source depth 5 for the Group II events using the deviatoric code, the full moment tensor code with the ISO option turned off, and the full moment tensor from the full moment tensor code.

(total%*ISO*+%*CLVD* 47-87%). Interestingly, the deviatoric solution from the full moment tensor code immediately yielded a significantly higher %DC for both Group II events, which was not expected. The full moment tensor solution further resolved the first event as having 83% DC (using a source depth of 5 km). The full moment tensor solution for the latter event looked primarily explosive, with only 20% DC.

14.4 Perspectives

The deviatoric solutions found with the full moment tensor code for both Group II events yielded significantly higher DC components than the best deviatoric solutions for those events determined using the deviatoric code. We intend to investigate this further.

In Figure 2.29, Group I and II events are located in the same area, the southern region of The Geysers, where Berkeley’s best DC solutions appear to reflect strike slip mechanisms.

The Berkeley Moment Tensor catalog (<http://seismo.berkeley.edu/~mike/solutions.new/>) contains numerous Geysers events, which will be reviewed with the full moment tensor code to determine whether they have significant ISO components. Computing full moment tensors for these events, especially for the larger events, may yield more information about the causes of seismicity at The Geysers.

14.5 Acknowledgements

Earthquake monitoring and reporting activities at the BSL are supported by the CISN funding of the California Governor’s Office of Emergency Services under contract 6023-5 and the US Geological Survey project 07HQAG0013.

14.6 References

- Ohlendorf, S., and D. Dreger, Evidence for Dilational Processes Accompanying Earthquakes at The Geysers Geothermal Field, California, The Third Annual Geoscience Graduate Symposium, Department of Geology and Geophysics, UW-Madison, Madison, WI, May 7-8, 2009 (poster).
- Dreger, D. S., H. Tkalic, and M. Johnston, Dilational processes accompanying earthquakes in the Long Valley Caldera, *Science*, 288, 122-25, 2000.
- Dreger, D., S.R. Ford, and W.R. Walter, Source analysis of the Crandall Canyon, Utah mine collapse, *Science*, 321, 217, 2008.
- Ford, S. R., D. S. Dreger and W. R. Walter, Source Characterization of the August 6, 2007 Crandall Canyon Mine Seismic Event in Central Utah, *Seism. Res. Lett.*, 114, B01306, doi:10.1029/2008JB005743.
- Minson, S. and D. Dreger, Stable Inversions for Complete Moment Tensors, *Geophys. Journ. Int.*, 174(2), 585-592, doi:10.1111/j.1365-246X.2008.03797.x.
- Pasyanos, M.E., D.S. Dreger, and B. Romanowicz, Toward Real-Time Estimation of Regional Moment Tensors, *Bull. Seism. Soc. Am.*, 86, 1255-1269, 1996.
- Romanowicz, B. D. Dreger, M. Pasyanos, and R. Uhrhammer, Monitoring of Strain Release in Central and Northern California Using Broadband Data, *Geophys. Res. Lett.*, 20, 1643-1646, 1993.

15 Statistical Testing of Theoretical Rupture Models Against Kinematic Inversions

Gilead Wurman, Richard M. Allen, Douglas S. Dreger, and David D. Oglesby (UC Riverside)

15.1 Introduction

The process by which earthquake ruptures initiate and propagate is usually expressed as one of two broadly-defined mechanisms: the cascade model and the preslip model. There is a diversity of modeling results that alternately support either cascade- or preslip-type rupture. At least some of the disagreement between the studies may be due to the high degree of variability among kinematic slip inversions, even for the same event. The recent development of the SRCMOD database makes it possible to examine many fault models in a statistical fashion to suppress the effects of this variability. Although the slip at the beginning of rupture is poorly resolved in kinematic inversions, using such a large number of events allows us to make first-order observations of any relationships.

15.2 Method

We examine 152 inversions of 80 different earthquakes in the SRCMOD database (<http://www.seismo.ethz.ch/srcmod>) as well as 7 teleseismic and 8 joint geodetic/teleseismic inversions provided by M. E. Pritchard (Pritchard *et al.*, 2006, 2007; Pritchard and Fielding, 2008; Loveless *et al.*, in review), for a total of 167 inversions and 95 events. We take the final slip distribution for each inversion and reconstruct the time- evolution of slip on the fault from rupture time and rise time information. We calculate the moment release within a given time window by summing the moment based on inferred slip at each grid point. For models with point-wise rupture time or rise time data, we initiate slip on each grid point at the associated rupture time, and increase slip to the final amount in a linear ramp over the associated rise time. In models where one or both of these parameters is not recorded point-wise, we take the reported average rupture velocity or rise time and assume a rupture front expanding isotropically from the hypocenter.

15.3 Relationship between early and final moment

The cascading hypothesis implies that at any given time after rupture initiation all earthquakes have the same magnitude. We can approximate this magnitude via the relation $M_0 = \mu SD = \mu \cdot \pi(V_R t)^2 \cdot \alpha V_R t = \pi \mu \alpha (V_R t)^3$ where $\mu = 3 \times 10^{11}$ dyne-cm, $S = \pi(V_R t)$ is the fault area after t seconds assuming a rupture velocity $V_R = 3 \times 10^5$ cm/s, and $D = \alpha V_R t$ is the mean

slip with $\alpha = 10^{-5}$. We find that a source duration of 1 second corresponds to a moment of approximately 2.5×10^{23} dyne-cm, or M_w 4.9. Thus in the cascading end-member case, any earthquake larger than magnitude 5 should look like a magnitude 5 at one second after nucleation. We can visualize this null hypothesis in Figure 2.30a. The solid diagonal line represents the limit in which the initial magnitude after 1 second is equal to the final magnitude, meaning the rupture has propagated to completion. Since there is no way for the initial magnitude to exceed the final magnitude, no points may lie above this solid line. This can potentially introduce a spurious positive slope to the data, and we minimize this by culling all data points for which the final magnitude is less than the reference magnitude. The hypothesis for a deterministic model is that there will be some positive scaling of the magnitude at 1 second with the final magnitude of the earthquake, yielding a positive slope to the data.

Figure 2.30b-e shows the initial magnitude plotted against the final magnitude for each event for four time windows ranging from 1 second to 8 seconds. We manually pick outliers, and exclude any events for which the initial magnitude is 99% or more of final magnitude, as those events have effectively terminated by the end of the time window. We also exclude all events with a final magnitude less than the reference magnitude for the null hypothesis as described above. The null hypothesis of cascading rupture can be rejected with greater than 95% confidence. The slope of the best-fit lines for all time windows between 1 and 10 seconds are strongly positive, suggesting some degree of non-self-similar behavior for these models. For time windows between 8 and 10 seconds the confidence is not as high as for time windows between 1 and 7 seconds. As rupture evolves, it experiences progressively more of the fault plane's heterogeneities and therefore has progressively more information about the likely final size of the earthquake. We therefore expect the initial magnitude to scale more strongly with final magnitude for longer time windows. One explanation for the degradation in scaling for longer time windows is that more and more events are being excluded due to having completed rupture, thus reducing the number of data points available for analysis. In Figure 2.30b-d, the number of points used for the fit varies between 112 and 128, and by 8 seconds (Figure 2.30e) that number has fallen to 80. Another possibility is that longer time windows afford greater resolution of the slip within the time

window, implying that the strong correlation observed for shorter time windows is a spurious result of poorly resolved slip in such short time spans. The influence of poorly resolved slip can be approximated visually by noting the open symbols, which represent models for which the time window was either shorter than the average rise time for the model or for which only one grid element had begun slipping in that time window.

We attempt to reduce the influence of poorly resolved slip by disregarding all of the “open” data points from Figure 2.30 which represent cases where the slip is likely to be particularly poorly resolved owing to the time window being too short. In addition, we recalculate both the initial and final magnitude for each point, disregarding any slip which is less than 10% of the peak slip for the model. This is to account for the fact that slip below 10% of peak slip is generally regarded as being poorly resolved in kinematic inversions and thus an unstable component of the slip models. Remarkably, the correlation between early and final magnitude is now even stronger, with the null hypothesis being rejected at greater than 99% confidence for all time windows. This suggests that poor resolution of slip in short time windows is not generating a spurious correlation between early and final magnitude. Rather, the analysis suggests that the decreasing number of data points in longer time windows (owing to more ruptures having run to completion) is primarily responsible for the weaker correlation for 8-10 second time windows seen in Figure 2.30.

15.4 Conclusions

We observe a strong scaling of early slip and magnitude with the final magnitude of these events. This result is inconsistent with the hypothesis that earthquakes are cascading rupture phenomena. After filtering the data the scaling remains robust, and in fact is more prominent, indicating that poor resolution of early slip is not the cause of the observed scaling. Given these findings, we must allow for the possibility that earthquakes are not purely cascading phenomena, and that magnitude is at least in part influenced by processes in the early part of the rupture process.

15.5 Acknowledgements

We thank Matt Pritchard for providing 15 of the slip models used in this study.

15.6 References

Loveless, J.P., M.E. Pritchard and N. Kukowski, Testing mechanisms of seismic segmentation with slip distributions from recent earthquakes along the Andean margin, *Tectonophysics*, in review.

Pritchard, M.E. and E.J. Fielding, A study of the 2006 and 2007 earthquake sequence of Pisco, Peru, with InSAR

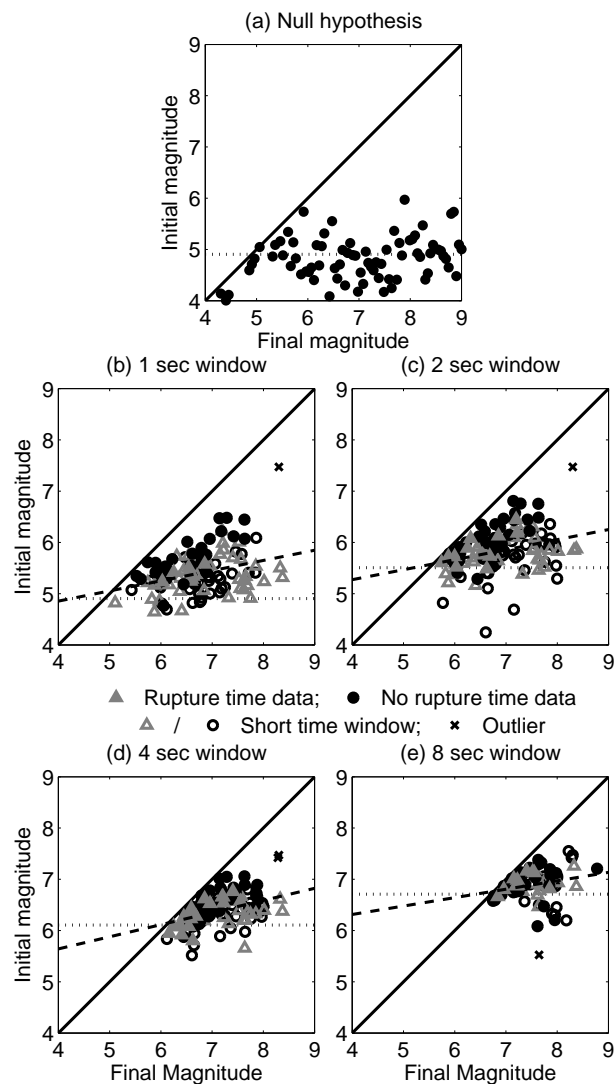


Figure 2.30: (a) Graphical expectation for the null hypothesis, that earthquakes are cascading ruptures. Dotted line represents the theoretical magnitude after 1 second. (b-e) Initial vs. final magnitude for time windows of 1, 2, 4 and 8 seconds. Dashed line represents the least-squares best fit to the data.

and teleseismic data, *Geophys. Res. Lett.*, *35*, L09308, doi:10.1029/2008GL033374, 2008.

Pritchard, M.E., C. Ji and M. Simons, Distribution of slip from 11 $M_w > 6$ earthquakes in the northern Chile subduction zone, *J. Geophys. Res.*, *111*, B10302, doi:10.1029/2005JB004013, 2006.

Pritchard, M.E., E.O. Norabuena, C. Ji, R. Boroschek, D. Comte, M. Simons, T. Dixon and P.A. Rosen, Geodetic, teleseismic, and strong motion constraints on slip from recent southern Peru subduction zone earthquakes, *J. Geophys. Res.*, *112*, B03307, doi:10.1029/2006JB04294, 2007.

16 Testing ElarmS in Japan

Holly Brown and Richard Allen

16.1 Introduction

Earthquake early warning systems detect the initial P-waves from an earthquake, rapidly estimate the magnitude of the event, and predict subsequent ground shaking in the region. Earthquake Alarm Systems, or ElarmS, is a network-based earthquake early warning algorithm that uses the amplitude and frequency content of P-waves from multiple stations to estimate the size and damage potential of an earthquake in realtime.

ElarmS has been tested on multiple California datasets (*Allen and Kanamori, 2003; Olson and Allen, 2005; Tsang, et al., 2007; Wurman, et al., 2007*). However there are limited numbers of recent, well-recorded, large earthquakes in California. We test ElarmS with a dataset of large earthquakes from Japan to improve the robustness of the system and to examine the adaptability of the algorithm to other seismic environments.

We then analyze the accuracy of the ElarmS magnitude estimates, location estimates, and ground shaking predictions, and produce error distributions for each of these three ElarmS outputs. The distributions depend on the quantity of available data, and can be accessed in realtime for uncertainty estimation during an event. We use the error distributions to create a model of the errors in the system. The model identifies the greatest source of error in the final ElarmS output.

16.2 Dataset

The dataset consists of 84 earthquakes, which occurred in Japan between September 1996 and June 2008 (Figure 2.31). The magnitudes range from 4.0 to 8.0, with 43 events of magnitude 6.0 or greater. The largest event is the 26 September 2003 Tokachi-Oki event, with magnitude 8.0.

The events were recorded by Japan's Kyoshin Net (K-NET) strong motion network. K-NET consists of 1,000 digital strong-motion seismometers spaced approximately 25km apart throughout Japan. Each station records ground motions as large as 2000 cm/s^2 .

16.3 Method

ElarmS estimates magnitude from the frequency content and peak displacement of the first few seconds of P-wave at each reporting station. Allen and Kanamori (2003) and Olson and Allen (2005) demonstrated an empirical relationship between magnitude and the observed maximum predominant period, t_{pmax} , of the P-wave. Wurman, et al., (2007) documented a relationship be-

tween magnitude and peak displacement, P_d , of the first few seconds of P-wave. ElarmS uses both relationships independently to calculate two magnitude estimates for a given event, and then averages the estimates together. As additional stations record P-wave arrivals, ElarmS incorporates their period and displacement measurements into the average to create a single magnitude estimate for the event.

ElarmS calculates event location by a three-dimensional grid search. Observed P-wave arrival times are compared to those predicted for a hypocenter at each node of the grid. For the Japanese events, grid layers occur in 10km depth increments, down to 80km.

When ElarmS has an estimated hypocenter and magnitude, it applies these to National Earthquake Information Center (NEIC) ShakeMap attenuation relations to predict ground shaking in the surrounding region. Initially, the prediction is based entirely on the estimated location and magnitude. As stations report peak ground shaking, the observations are incorporated into the predictions.

16.4 Error Distributions

We isolate the location, magnitude and ground shaking processing steps to determine independent error distributions for each of these steps. The error in each step depends on the number of stations triggering, the number of seconds of P-wave arrival, and the number of stations reporting peak ground shaking observations. Thus we have separate error distributions for each quantity of inputs. Figure 2.31 shows the mean error for each distribution curve.

16.5 Error Model

We use these error distributions to create an error model for ElarmS processing. The model calculates the total error in the system, after magnitude, location, and attenuation relation errors have propagated through to the final prediction of shaking. In total, we consider 1081 different combinations of data input quantities, and create a separate error distribution for each combination. These are collectively shown in Figure 2.32a. These 1081 distributions are contained in an ElarmS library, which can be accessed in realtime. Given any combination of number of stations reporting, number of seconds of P-wave arrival, and number of peak ground shaking observations, the appropriate error distribution can be consulted to produce a realtime estimate of uncertainty in the ElarmS prediction of ground shaking.

Table 1: Mean \pm standard deviation of error distributions used by error model.						
	0 stations	1 station	2 stations	3 stations	4 stations	5 stations
Magnitude error, 1 sec of P-wave	-	-0.38 \pm 0.63	-0.33 \pm 0.56	-0.37 \pm 0.57	-0.39 \pm 0.56	-0.41 \pm 0.56
Magnitude error, 2 sec of P-wave	-	-0.2 \pm 0.57	-0.15 \pm 0.5	-0.18 \pm 0.54	-0.21 \pm 0.52	-0.22 \pm 0.50
Magnitude error, 3 sec of P-wave	-	-0.09 \pm 0.53	-0.05 \pm 0.48	-0.08 \pm 0.52	-0.10 \pm 0.49	-0.10 \pm 0.47
Magnitude error, 4 sec of P-wave	-	0.01 \pm 0.52	0.04 \pm 0.46	0.03 \pm 0.48	0.03 \pm 0.44	0.02 \pm 0.43
Magnitude error, 5 sec of P-wave	-	0.04 \pm 0.50	0.07 \pm 0.45	0.07 \pm 0.48	0.07 \pm 0.43	0.06 \pm 0.42
Location error	-	33.6 \pm 17.9	32.1 \pm 21.4	32.5 \pm 18.7	18.8 \pm 13.6	21.1 \pm 16.8
PGA prediction error	0.11 \pm 0.30	0.09 \pm 0.35	0.08 \pm 0.37	0.06 \pm 0.29	0.10 \pm 0.28	0.03 \pm 0.30

Figure 2.31: Mean errors in magnitude estimates, location estimates, and peak ground shaking predictions. Location error is in km. PGA error is the ratio of the predicted PGA to the observed PGA; a factor-of-two error in the predicted PGA relative to the observed PGA corresponds to an error of 0.7.

From the model we isolate the error contribution of each processing step, by “turning off” each contribution in turn. For example, Figure 2.32c shows the error model when the location estimate exactly equals the catalog location (zero location error); all error in the system comes from magnitude estimation and the attenuation relations used to predict ground shaking. Figure 2.32d is the error model when the magnitude estimate exactly equals the catalog magnitude, and error is contributed only by location and attenuation relations. Figure 2.32b is the error model when the attenuation relations are perfect, and all error comes from the location and magnitude estimates. Note the sharper, higher peak in Figure 2.32b. This indicates less error in the system for this scenario. That is, if the attenuation relations were perfect, the error in ElarmS’ output would be significantly reduced. We conclude from this that the prediction of ground motions, produced from NEIC ShakeMap attenuation relations, contributes far more error to the final ElarmS prediction of localized shaking than do the magnitude estimate or location estimate. This suggests that more work should be devoted to improving attenuation relations, and that regional relations should be used whenever possible.

16.6 Conclusion

ElarmS’ successful tests on Japanese events confirm that the ElarmS algorithm is relevant in a subduction zone environment and for large-magnitude events. The error distribution curves and error model show that the attenuation relations contribute the largest source of error to the final ElarmS prediction of ground shaking.

16.7 Acknowledgements

We thank K-NET for the use of their data. This work was funded by USGS/NEHRP award 06HQAG0147.

16.8 References

Allen, R.M., and H. Kanamori, The potential for earthquake early warning in southern California, *Science* 300, 786-

789, 2003.

Olson, E.L., and R.M. Allen, The deterministic nature of earthquake rupture, *Nature* 438, 212-215, 2005.

Tsang, L., R.M. Allen, and G. Wurman, Magnitude scaling relations from P-waves in southern California, *Geophys. Res. Lett.* 34, L19304, 2007.

Wurman, G., R.M. Allen and P. Lombard, Toward Earthquake Early Warning in Northern California, *J. Geophys. Res.* 112, B08311, 2007.

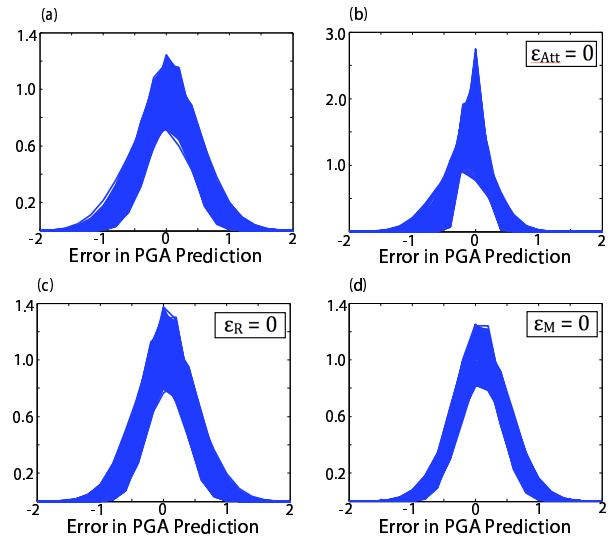


Figure 2.32: Error Model, with 1081 individual error distributions, based on differing quantities of input data (number of stations, number of seconds, number of PGA observations). (a) Complete error model. Error is contributed by magnitude estimate, location estimate, and attenuation relations (used to predict ground shaking). (b) Error model when attenuation relations error is removed. (c) Error model when location error is removed. (d) Error model when magnitude error is removed.

17 Real-time Earthquake Detection and Hazard Assessment by ElarmS Across California

Holly Brown, Richard Allen, Margaret Hellweg, Oleg Khainovski, Peter Lombard, Douglas Neuhauser, and Adeline Souf

17.1 Introduction

ElarmS is a network-based methodology for rapid earthquake detection, location, and hazard assessment in the form of magnitude estimation and peak ground motion prediction. The methodology is currently being tested as part of the real-time seismic system in California, leveraging the resources of the California Integrated Seismic Network (CISN) and the Advanced National Seismic System. ElarmS processing modules at three network processing centers reduce waveforms to a few parameters. These are then collected and processed at UC Berkeley to provide a single statewide prediction of future ground shaking that is updated every second.

The development of a statewide realtime warning system has presented several methodological and programming challenges. Here we focus on the system delays as data is passed between processing centers.

17.2 Method

ElarmS uses the P-wave recorded on velocity and acceleration sensors to detect, locate, and estimate the magnitude of an earthquake. The initial estimate of location is beneath the first station to trigger, then between the first two stations based on the arrival times. Once three triggers are available the event is located using a grid search to minimize arrival time residuals. The depth for all events in California is set at 8 km.

The ElarmS magnitude estimate is based on the amplitude and frequency content of the P-wave arrival. For a given trigger, the maximum observed displacement, P_d , and predominant period, t_{pmax} , are converted to a magnitude estimate using empirical scaling relations [Allen and Kanamori, 2003; Tsang et al., 2007; Wurman et al., 2007]. Magnitude estimates for all triggered stations are averaged at each time step to provide a single estimate for the event.

The methodology naturally divides into a waveform processing module (WP) and an event monitoring module (EVM). WP operates on each data channel individually to reduce the seismic waveform to parameters including trigger times, P_d , P_v , t_{pmax} , peak ground velocity (PGV), peak ground acceleration (PGA) and signal-to-noise levels. The WP module can therefore be distributed. It currently runs at UC Berkeley processing waveforms from the Berkeley Digital Seismic Network (network code BK) at the USGS Menlo Park, processing the Northern California Seismic Network (NC) and some USGS Strong Motion Network (NP) data, and at

Caltech/USGS Pasadena processing Southern California Seismic Network (CI), the Anza Network (AZ), and additional NP data. WP output parameters are telemetered to UC Berkeley where a single implementation of the EVM module integrates data from across the state to detect and analyze earthquake occurrence in real-time.

The EVM module currently processes waveform data from 383 stations (222 velocity instruments and 381 accelerometers) of the BK, NC, NP, CI, and AZ networks (Figure 2.33). The real-time implementation of ElarmS is now processing all stations in California that can be used by the system.

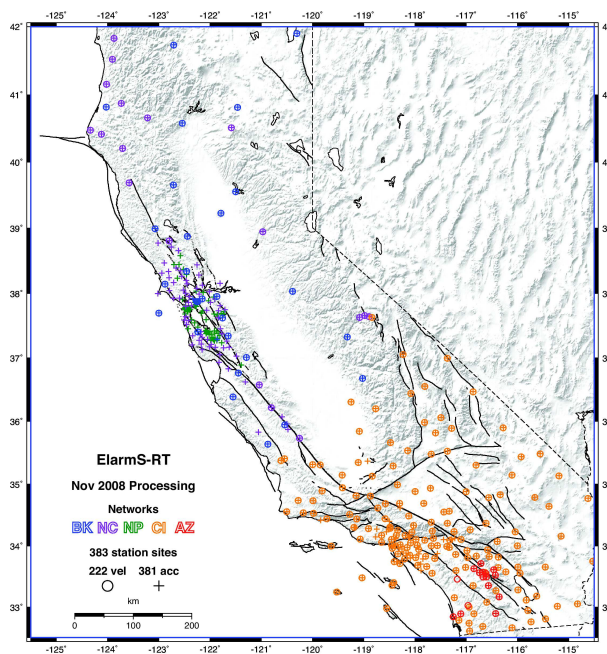


Figure 2.33: Map of stations currently used by realtime system.

17.3 Results

Every second required to telemeter data is a second reduction in warning time. Minimizing the time needed for data telemetry and processing is therefore an important aspect of a network-based early warning system. Figure 2.33 shows the current data latencies for ElarmS in California. The first cause of latency is the delay in getting data to the first shared memory region at its network processing site at UC Berkeley, Caltech/USGS Pasadena, or

USGS Menlo Park (Figure 2.33a). Most of this delay is due to packetization of data. Data loggers at each station wait until a data packet is full before sending it across the telemetry system. Modifications to the configuration of many data loggers could reduce the size of these packets, reducing the overall latency. The actual telemetry (communication) delay at most sites most of the time is a fraction of a second, although packets can be delayed, resulting in the long tail to the distribution. The median waveform data latencies are 2.0, 6.5, 6.6, 6.6, and 11.5 second for NC, CI, BK, NP, and AZ, respectively. AZ has long latencies because AZ data is forwarded from Scripps to Caltech before it is processed by ElarmS. The median latency over all station channels is 6.5 sec.

Once the waveform data has arrived at the first shared memory region at a network center, WP processes the data to determine parameters. Parameters from Caltech/USGS Pasadena and USGS Menlo Park are then forwarded to UC Berkeley where they are incorporated into EVM as they arrive. Figure 2.33b shows the total latency in incorporating P-wave trigger times into the EVM output representing the current latency of the entire system. The median delay is 11.8 seconds and the distribution has a positive-skew, meaning that most frequent latency is in the 9-10 second window but there is a long tail at higher latencies. The actual processing of data by WP or EVM takes a fraction of a second. Most of the additional latency is therefore due to the process of moving data between the shared memory regions at the various stages of processing (including between network centers).

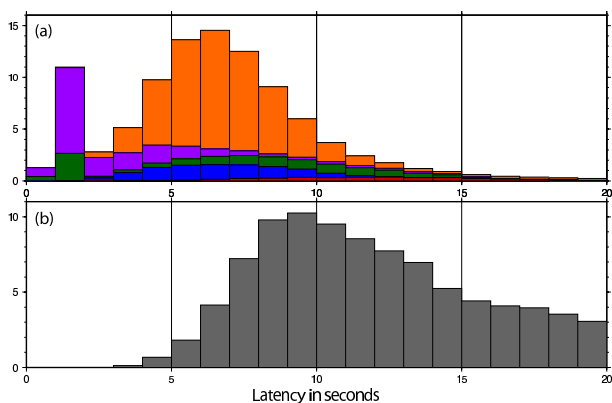


Figure 2.34: Histogram of latencies in the statewide system. (a) Waveform telemetry latency: delay between the absolute time of a P-wave trigger and when it arrives at the network processing center. Blue is BK, purple is NC, green is NC, orange is CI, red is AZ. (b) Total ElarmS latency: delay between the absolute time of a P-wave trigger and the timestamp of the EVM output file that incorporates that trigger.

17.4 Conclusions

The state-wide, real-time test of ElarmS has only just begun (November 2008) so there will be additional methodology development necessary to handle the myriad technical issues that arise as a result of processing the approximately 15 billion observations per day that arrive with varying data latencies and various seismological and electronic sources of noise. In addition, further development is necessary to minimize the warning latency by improving the codes (currently 5 second delay) and upgrading station hardware (currently 6.5 second delay).

17.5 Acknowledgements

The real-time implementation and testing of ElarmS in California is part of a project by the California Integrated Seismic Network (<http://www.CISM.org/>) to test several early warning methodologies in the state. We have worked in collaboration with M. Böse, E. Hauksson, T. Heaton and K. Solanki at Caltech; T. Jordan and P. Maechling at USC and SCEC; D. Given and D. Oppenheimer at the USGS; M. Zeleznik of Saya Systems; and G. Cua at the Swiss Seismological Service. The project is funded by the USGS through cooperative agreement 06HQAG0147.

17.6 References

- Allen, R. M., and H. Kanamori, The potential for earthquake early warning in southern California, *Science* 300, 786-789, 2003.
- Allen, R. M., H. Brown, M. Hellweg, O. Khainovski, P. Lombard, and D. Neuhauser, Real-time earthquake detection and hazard assessment by ElarmS across California, *Geophys. Res. Lett.* 36, L00B08, 2009.
- Böse, M., E. Hauksson, K. Solanki, H. Kanamori, and T. H. Heaton, Real-time testing of the on-site warning algorithm in southern California and its performance during the July 29 2008 M_w 5.4 Chino Hills earthquake, *Geophys. Res. Lett.* 36, L00B03, 2009.
- Tsang, L., R.M. Allen, and G. Wurman, Magnitude scaling relations from P-waves in southern California, *Geophys. Res. Lett.* 34, L19304, 2007.
- Wurman, G., R.M. Allen and P. Lombard, Toward Earthquake Early Warning in Northern California, *J. Geophys. Res.* 112, B08311, 2007.

18 Joint Inversion of Group Velocity Dispersion and Long Period Waveforms for Upper Mantle Structure

Vedran Lekic and Barbara Romanowicz

18.1 Introduction

Surface waves and overtones provide excellent constraints on crustal, upper mantle, and transition zone structure. They offer far better radial resolution of shallow structure than is possible with teleseismic body waves, while simultaneously having excellent global coverage and signal-to-noise ratios. Indeed, since its development a quarter century ago (Woodhouse and Dziewonski, 1984), the modeling of long period waveforms of surface waves and overtones using approximate techniques has made possible the development of high resolution models of upper mantle shear wave velocity and radial anisotropy (Panning and Romanowicz, 2006; Kustowski et al., 2008).

However, the ray- and perturbation theory that underlies these efforts can result in modeling errors that exceed the noise level of the observed waveforms (Panning et al., 2009). In the case of realistic crustal structure, the modeling inaccuracies can significantly contaminate the retrieved images of mantle velocity and radial anisotropy (Lekic et al., 2009). Fortunately, the development of computational techniques capable of fully modeling wave propagation through a complex, heterogeneous medium such as the Earth (Spectral Element Method: e.g. Capdeville et al., 2003) has enabled tomographers to move away from approximate techniques.

The superior accuracy of the spectral element method comes at a far greater computational cost than that associated with approximate techniques. In particular, crustal structure comprising thin layers substantially increases computational costs. At the same time, inaccuracies in existing global crustal models like CRUST2 (Bassin et al., 2000) can contaminate the retrieved mantle images. Because of this, there is a need for a new crustal model that avoids the meshing of thin layers while increasing the accuracy of crustal corrections. Long period waveforms lack the resolution necessary for crustal inversion, so we supplement our waveform dataset using $1 \times 1^\circ$ Rayleigh and Love group velocity dispersion maps provided by *M. Ritzwoller (personal communication)* spanning the 25-150 sec period range.

Here, we present preliminary results of a joint inversion of group velocity dispersion and long period waveforms for crustal and upper mantle elastic structure.

18.2 Method

Tomographic imaging of the Earth's interior using waveforms is a non-linear process requiring an iterative procedure. Each iteration involves a forward modeling

step in which three-component waveforms with periods longer than 60 s are calculated using the spectral element method through a 3D model of isotropic shear wavespeed (V_S) and radial anisotropy (ξ). The partial derivatives relating model perturbations to time-domain misfits between data and synthetics are calculated using non-linear asymptotic coupling theory (NACT: *Li and Romanowicz, 1995*). Model updates are obtained by following the procedures described in *Mégnin and Romanowicz (2000)* and references therein.

In order to account for non-linear effects of model perturbations on group velocities and develop an unbiased starting crustal model, we begin by creating 21,000 candidate models which span a variety of crustal V_S (2-4 km/s). V_S is scaled to compressional wavespeed and density using relations of *Brocher (2003)*. In order to avoid meshing thin crustal layers, we fix crustal thickness to 60 km and mimic the response of a layered isotropic medium by introducing anisotropy (i.e. ξ is allowed to vary between 0.6 and 1.4). The models are represented as degree 3 polynomials, and their group velocities are calculated using a modified MINEOS code (*Woodhouse, 1988*).

Once we obtain a starting crustal model, we regionalize it by grouping similar velocity profiles into 4 clusters, and then summarizing each cluster by a single model of mean density and slownesses. For each reference profile, we then calculate group velocity dispersion curves and partial derivatives relating logarithmic group velocity perturbations from the reference values to perturbations in V_S and ξ . The most appropriate regional kernels are then used to obtain a model update which minimizes the logarithmic misfits between predictions and the group velocity dispersion at each point on the Earth. This ensures that the perturbations are always within the linear regime.

18.3 Results

Figure 2.35 compares the V_S structure of the uppermost mantle obtained using CRUST2 and long period waveforms alone (A: left) and our new Earth model obtained by jointly inverting long period waveforms and group velocity dispersion constraints (B: right). The differences between the models are prominent at shallow depths, where model B exhibits substantially stronger correlation between V_S anomaly and age of oceanic plates. At 100 km, the models are similar, though further differences emerge at 250 km, at which depth model B shows fewer fast anomalies beneath Asia, save for those

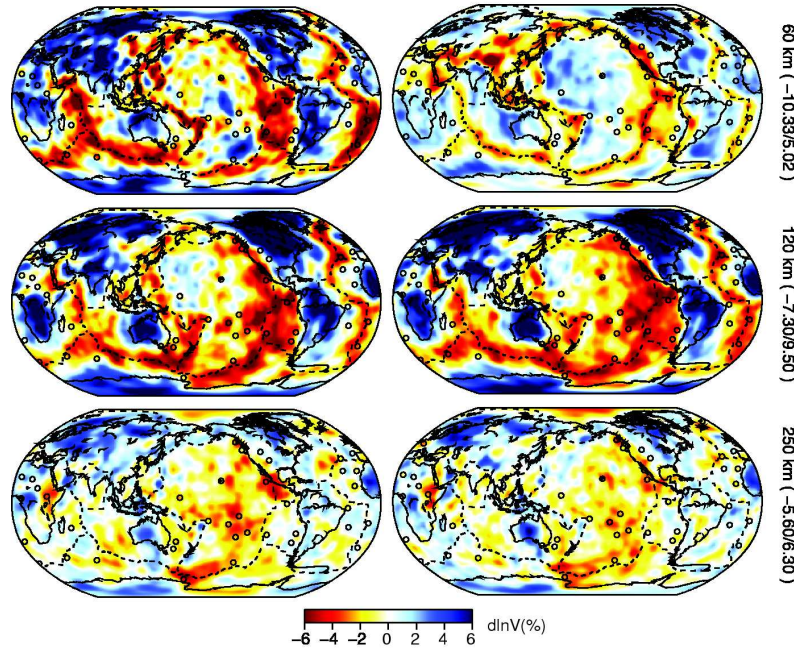


Figure 2.35: Models developed using long period waveforms with (right) and without (left) higher frequency group velocity dispersion maps.

corresponding to the Siberian and Finnoscandian cratons.

The model developed using CRUST2 fits Love waves two times worse than Rayleigh waves, even when inverting for radial anisotropy variations. However, by including higher frequency group velocity measurements and inverting for crustal structure, we improve the fits to both Love and Rayleigh waves and bring them closer to parity.

We plan to carry out further iterations and resolution tests to quantify the benefits of joint inversion of long period waveforms and shorter period group velocity dispersion curves.

18.4 Acknowledgements

This research was supported by National Science Foundation grant NSF/EAR-0308750.

18.5 References

Bassin, C., Laske, G. and G. Masters, 2000. The Current Limits of Resolution for Surface Wave Tomography in North America. *EOS Trans AGU* 81, F897.

Brocher, T.M., 2003. Empirical Relations between Elastic Wavespeeds and Density in the Earth's Crust. *BSSA*, 95, 2081-2092.

Capdeville, Y., E. Chaljub, J.P. Vilotte and J.P. Montagner, 2003. Coupling the spectral element method with a modal solution for elastic wave propagation in global Earth models. *Geophys. J. Int.*, 152, 34-66.

Lekic, V., M. Panning and B. Romanowicz, 2009. A simple method for improving crustal corrections in waveform tomography. *Submitted to Geophys. J. Int.*

Li, X.D. and B. Romanowicz, 1995. Comparison of global waveform inversions with and without considering cross-branch modal coupling, *Geophys. J. Int.*, 121, 695-709.

Megnin, C. and B. Romanowicz, 2000. The three-dimensional shear velocity structure of the mantle from the inversion of body, surface and higher-mode waveforms. *Geophys. J. Int.*, 143, 709-728.

Panning, M. and B. Romanowicz, 2006. A three-dimensional radially anisotropic model of shear velocity in the whole mantle. *Geophys. J. Int.*, 167, 361-379.

Panning, M.P., Y. Capdeville, and B.A. Romanowicz, 2009. Seismic waveform modelling in a 3-D Earth using the Born approximation: potential shortcomings and a remedy. *Geophys. J. Int.*, 177, 161-178.

Woodhouse, J.H. and A.M. Dziewonski, 1984. Mapping the upper mantle: three dimensional modeling of Earth structure by inversion of seismic waveforms. *J. Geophys. Res.* 89, 5953-5986.

Woodhouse, J.H., 1988. The calculation of eigenfrequencies and eigenfunctions of the free oscillations of the Earth and the Sun. *Seismological Algorithms*, ed. Doornbos, D.J., 321-370.

19 Reactivation of an Archean Craton: Constraints from P- and S-wave Tomography in North China

Liang Zhao, Richard M. Allen, Tianyu Zheng, and Shu-Huei Hung

19.1 Introduction

Cratonic nuclei often induce stress concentration and strain localization at their boundaries (Tommasi and Vauchez, 2001), but internally remain stable over very long geological periods. However, the unusual reactivation of the NCC challenges the classical views concerning the strength and stability of cratonic lithosphere. It is proposed that the North China Craton (NCC) (Figure 2.36) formed in the Paleoproterozoic by the amalgamation of two Archean blocks, the Eastern and Western Blocks (EB and WB), along the Central Block (CB) (e.g., Zhao *et al.*, 2001). While there is a growing consensus that lithospheric rifting has occurred in the EB and extended to the CB (Xu *et al.*, 2004; Zhao *et al.*, 2008), evidence for the vertical and horizontal distribution of lithospheric reactivation still remains unclear. This study is the first to provide high-resolution imaging of both P- and S- wave velocities in an effort to understand the process of reactivation of an Archean craton.

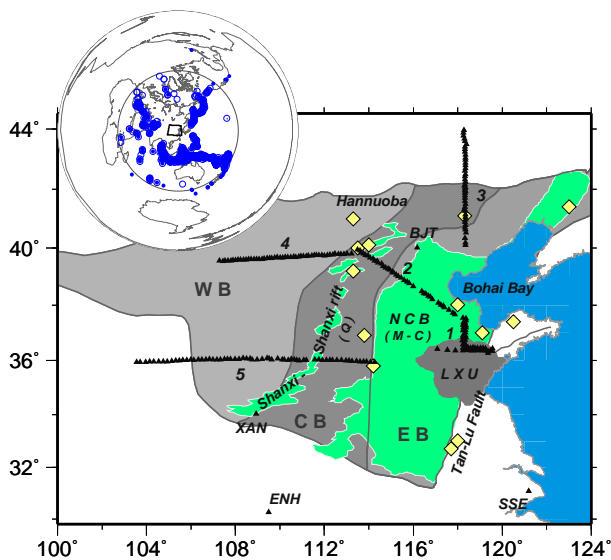


Figure 2.36: Simplified tectonic map showing major tectonic units of the NCC and seismic station locations. The triangles mark stations; yellow diamonds represent locations of Cenozoic basalts; green shadow zones indicate pull-apart basins; numbers indicate the indices of NCISP sub-arrays.

19.2 P- and S-wave Velocity Models and Resolution Tests

Our results show that structures imaged by finite-frequency kernel methods (Figure 2.37) and ray-based methods are very similar, except that the kernel-based models yield higher root-mean-square amplitude of P and S wave velocity perturbation, as expected (Hung *et al.*, 2004). The first-order features of our models, for both P- and S-waves, include: (1) A north-south trending narrow low-velocity region with dimension of 800 km north-south and 200-300 km east-west is located at the base of the CB lithosphere, and extends to more than 300 km depth. The northernmost and southernmost parts extend to more than 500 km depth. (2) A region of high-velocity extends to more than 250-300 km depth beneath the WB, in contrast to the much shallower high-velocity zones beneath the CB and EB.

Resolution tests show that the resolution is good down to 600km depth for anomalies ≥ 200 km even for data with 30% noise in the regions with good sampling coverage, and the downward smearing length is less than 50 km.

19.3 Conclusions

Finite-frequency kernel based P- and S-wave velocity images show that a N-S trending low velocity anomaly extends from beneath the CB to at least 500 km. High-velocity anomalies extend to more than 250-300 km depth beneath the WB, and to shallower depths beneath the CB and the EB. The imaged structure suggests that the presence of warm material with a source at least as deep as the transition zone is responsible for reactivation of the NCC. The pre-existing weak zone within the CB of the craton likely acted as a sublithospheric corridor for the warm mantle material.

19.4 Acknowledgements

This work was completed during L. Zhao's visit to Berkeley Seismology Lab sponsored by K.C. Wong Education Foundation, Hongkong. We thank M. Xue, M. Obrebski, H.Y. Yuan, R. Porritt, W.W. Xu, L. Chen and C. Paffenbarger for constructive help.

19.5 References

Hung, S., et al., Imaging seismic velocity structure beneath the Iceland hot spot: A finite frequency approach, in *J. Geophys. Res.*, 109, B08305, doi:10.1029/2003JB002889, 2004.

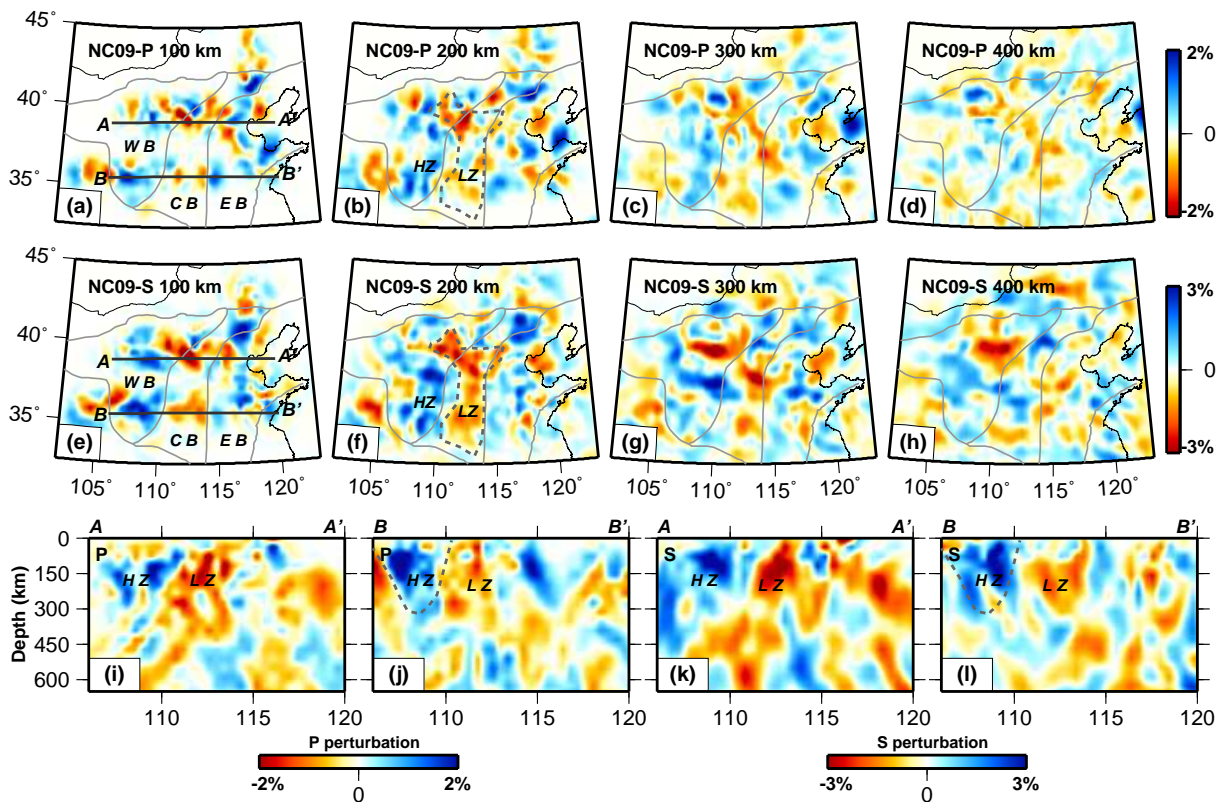


Figure 2.37: P- and S-wave velocity perturbations resolved from finite-frequency tomography. (a)-(d) P-wave velocity perturbations at indicated depths. (e)-(h) S-wave velocity perturbation. Cross sections are presented along A-A' and B-B' in (i) and (j) for the P-wave and (k) and (l) for S-wave model. Closed dashed lines on (b) and (f) give the outline of recognized N-S low velocity zone beneath the CB; dashed line on (j) represents high-velocity zone beneath the WB. LZ: low-velocity zone; HZ: high-velocity zone.

Tommasi, A., and A. Vauchez, Continental rifting parallel to ancient collisional belts: an effect of the mechanical anisotropy of the lithospheric mantle, in *Earth Planet. Sci. Lett.*, 185, 199-210, 2001.

Xu, Y., et al., Contrasting Cenozoic lithospheric evolution and architecture in the eastern and western Sino-Korean craton: constraints from geochemistry of basalts and mantle xenoliths, in *J. Geology*, 112, 593-605, 2004.

Zhao, G., et al., Archean blocks and their boundaries in the North China Craton: lithological, geochemical, structural and P-T path constraints and tectonic evolution, in *Precambrian Res.* 107, 45-73, 2001.

Zhao, L., et al., Insight into craton evolution: Constraints from shear wave splitting in the North China Craton, in *Phys. Earth Planet. Inter.*, 168, 153-162, 2008.

20 Plume vs. Plate: Convection Beneath the Pacific Northwest

Mathias Obrebski, Richard M Allen, Mei Xue (Tongji University, Shanghai, China) Shu-Huei Hung (National Taiwan University, Taipei, Taiwan)

20.1 Introduction

The Pacific Northwest of western North America is unusual in that both a subducting slab and a hotspot occur within 1000 km of one another. The Juan de Fuca plate (JdF) that continues to subduct today (Figure 2.38) is a remnant corner of the Farallon plate. Subduction beneath the Pacific Northwest has been continuous for more than ~ 150 Ma (Atwater, 1989) and we would expect, and previous work has imaged, several thousand kilometers of slab extending deep into the mantle (Sigloch *et al.*, 2008). The westernmost US hosts major Neogene to Quaternary volcanic provinces. The Columbia River Basalts (CRB) are the product of a phase of massive volcanic outpouring that occurred 17 Ma. The Yellowstone Snake River Plain is a bimodal volcanic trend that exhibits a time progressive sequence of calderas. Two groups of hypotheses have been proposed to explain this surface geology: a stationary deep-seated whole mantle plume (Pierce *et al.*, 2000; Camp and Ross, 2004; Smith *et al.*, in review), or various lithospheric-driven processes of fracture and volcanism (Dickinson, 1997; Humphreys *et al.*, 2000; Christiansen *et al.*, 2002). Nevertheless, seismic imaging efforts to constrain the geometry of any Yellowstone plume anomaly through the mantle have been inconclusive.

20.2 Data and Method

Here we compile a seismic waveform dataset consisting of teleseismic body-waves, both direct and core phases, recorded at seismic stations across the western United States. We use data from the US from Earthscope's US-Array, the regional seismic networks and temporary seismic deployments that together provide an array of more than 1000 seismometers with an unprecedented density and spatial extent. Relative body-wave traveltime delays are measured by cross-correlation in the 1.25 to 0.5 sec frequency band for compressional arrivals and 50 to 10 sec for shear arrivals. We use events at greater than 30° epicentral distance with magnitude greater or equal to 5.5 from January 2006 to July 2009. The compressional-arrival dataset is derived from 30,670 traveltime observations of direct P from 127 earthquakes. The shear-arrival dataset includes 38,750 travel-time measurements, 34,850 S-wave observations from 142 events and 3,900 SKS observations from 24 events. In this study, we combine this regional dataset with a tomographic technique utilizing finite frequency sensitivity kernels. The banana-doughnut-shaped kernels account for the frequency- and depth-dependent width of the region to which teleseismic body-waves are sensitive and account for wave-front

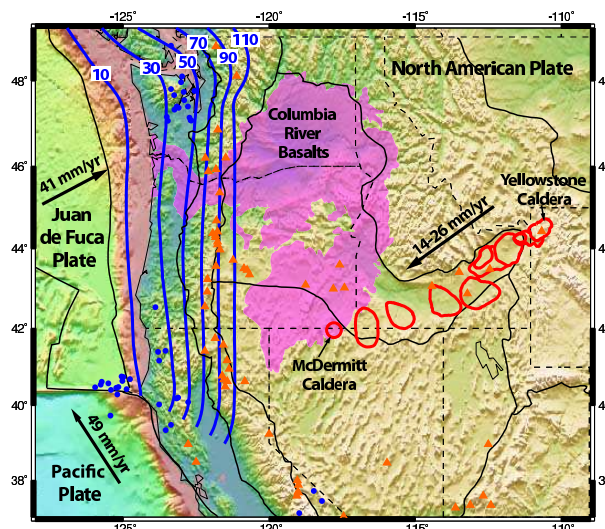


Figure 2.38: Geologic-tectonic features of the Pacific Northwest of the United States overlaid on topography and bathymetry. The Juan de Fuca plate is subducting beneath the North American plate with an oblique convergence rate of 41 mm/yr. The estimated depth of the top of the subducting slab is shown with blue contours labeled in km. The location of all $M > 4$ earthquakes with depth > 35 km since 1970 are shown as blue dots. Volcanoes are shown as orange triangles. The Yellowstone Hotspot Track exhibits a series of time-progressive calderas (red outline) from McDermitt (~ 16.1 Ma) to the currently active Yellowstone Caldera. The track is approximately parallel to the absolute plate motion of North America. The Columbia River Flood Basalt Province was a massive outpouring of basalt from ~ 16.6 to ~ 15.0 Ma and is shown in pink.

healing effects. Our tomographic method uses paraxial kernel theory to calculate the forward scattering sensitivity kernels for teleseismic arrival times (Hung *et al.* 2004).

20.3 Results and Discussion

The main features imaged in both our P and S models (Figure 2.39) include a whole mantle plume beneath Yellowstone emplaced between slab fragments, the surprisingly short and uneven Juan de Fuca plate, and the presence of a fossil slab fragment adjacent to the currently subducting slab. Interpreted together, all these features are strong indications that the Yellowstone plume broke

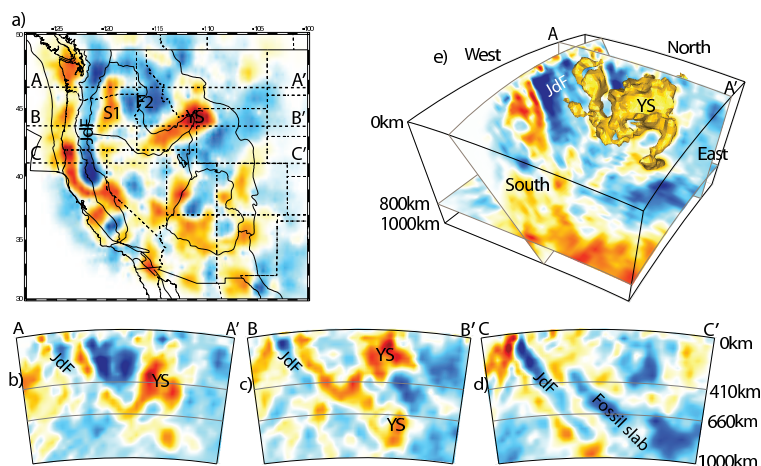


Figure 2.39: Cross sections through our P model. (a) Constant depth slice at 200 km showing the continuous high-velocity Juan de Fuca slab and the strong low-velocities below the Yellowstone Caldera. (b) through (d) are E-W cross-sections at locations shown in (a). The currently subducting slab is visible in all sections though the amplitude of the slab anomaly reduces from south to north. The Yellowstone plume has a strong signature as deep as 900km in (b) and (c). The parallel fossil-slab anomaly is strong in (d). (e) is composed of an oblique section through the Juan de Fuca slab, a constant depth slice at 800km, the E-W vertical slice (b) and a 3D isosurface that illustrates the 3D geometry of the Yellowstone plume.

through the Farallon slab to reach the surface, and that it thermally consumed part of the slab. We propose that as the plume head rose towards the surface the Farallon slab first stopped it. Due to continuous thermal erosion and flexure imposed by the increasing volume of hot and buoyant plume material, the portion of the slab located above the head of the plume weakened and was assimilated by it. Free from structural barrier, the resulting blend continued its ascent to the surface and fed the CRB. The geochemistry of the of the Grande Ronde basalts, representing the climax stage of the CRB and more than 80% of the volume of the CRB, has been interpreted as a heterogeneous source of plume material containing fragments of oceanic crust (Takahahshi *et al.*, 1998), consistent with this interpretation. Farther from the plume conduit, the slab that was not thermally consumed eventually broke. Assuming a subduction rate of around 5cm/y to account for the higher Pacific-North America convergence velocity during the Neogene (Riddihough, 1984), the slab rupture evidenced by our model would have been achieved at the time of or slightly before the CBR outpouring.

20.4 References

- Atwater, T., Plate tectonic history of the northeast Pacific and western North America, in Winterer, E. L., Hussong, D. M., and Decker, R. W., eds., *The Eastern Pacific Ocean and Hawaii: Geological Society of America, Boulder, Colorado, The Geology of North America*, v. N, 21-72, (1989).
- K. Sigloch, N. McQuarrie, G. Nolet, Two-stage subduction history under North America inferred from multiple-

- frequency tomography, *Nature Geoscience*, 1, 458 (2008).
- K. L. Pierce, L. A. Morgan, R. W. Saltus, Yellowstone plume head: Postulated tectonic relations to the Vancouver slab, continental boundaries and climate, Open-File Report 00-498, U.S. Geological Survey, (2000).
- V. E. Camp, M. E. Ross, Mantle dynamics and genesis of mafic magmatism in the intermontane Pacific Northwest, *J. Geophys. Res.* 109, B08204, (2004).
- R. B. Smith *et al.*, Geodynamics of the Yellowstone Hotspot and Mantle Plume: Seismic and GPS Imaging, Kinematics, and Mantle Flow, *J. Vol. Geotherm. Res.*, (in review).
- W. R. Dickinson, OVERVIEW: Tectonic implications of Cenozoic volcanism in coastal California, *Geol. Soc. Am. Bull.*, 109, 936 (1997).
- E. D. Humphreys, K. G. Dueker, D. L. Schutt, R. B. Smith, Beneath Yellowstone: Evaluating Plume and Nonplume Models Using Teleseismic Images of the Upper Mantle, *GSA Today*, 10, 1 (2000).
- R. L. Christiansen, G. R. Foulger, J. R. Evans, Upper-mantle origin of the Yellowstone hotspot, *Geol. Soc. Am. Bull.*, 114, 1245 (2002).
- E. Takahahshi, K. Nakajima, T. L. Wright, Origin of the Columbia River basalts: melting model of a heterogeneous plume head, *Earth Planet. Sci. Lett.*, 162, 63 (1998).
- R. Riddihough, Recent Movements of the Juan de Fuca Plate System, *J. Geophys. Res.*, 89, B8, (1984)

21 Imaging Shallow Cascadia Structure with Ambient Noise Tomography

Robert W. Porritt and Richard M. Allen

21.1 Introduction

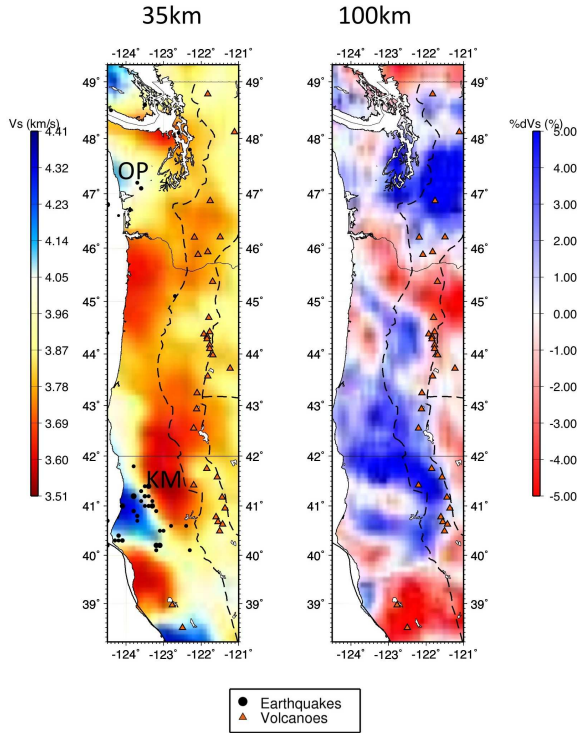


Figure 2.40: A - depth slice at 35km below mean sea level. This is plotted in best fit velocity to show crustal to uppermost mantle structure. B - slice at 100km depth plotted in relative velocity to highlight lateral variation.

Along strike variation has been observed along the Cascadia Subduction Zone in studies with a variety of data sets. Body-wave tomography shows a broad zone in the center of the slab with a weak high velocity signal in an atypically quiescent seismic zone (*Obrebski and Allen, 2009*). Primitive basalts in the arc volcanoes change characteristics along strike, defining four distinct magma sources or plumbing systems (*Schmidt et al, 2007*). Most striking, however, is the change in recurrence rate of episodic tremor and slip throughout the region (*Brudzinski and Allen, 2007*). These disparate observations may reflect regional variations in the lithosphere. This study seeks to connect these previous observations by developing a short period surface wave model of structure in the region using ambient seismic noise as the source.

21.2 Data Processing

Data for this study comes from the Berkeley Digital Seismic Network (BDSN), Southern California Earthquake Center, the Canadian National Seismic Network, and USArray with a focus on two Flexible Array Experiments. The Flexible Array deployments, FlexArray Along Cascadia For Segmentation (FACES) and Mendocino Broadband, were deployed in 2007 and are nearing the completion of their two year deployments. This is one of the first studies utilizing the approximately one hundred stations in these broadband experiments.

Detailed processing flow for computing group and phase velocity maps can be found in *Benson et al, 2007*. Group and phase velocity mean values and errors are computed using a jack knife approach from cross correlations of 11 months of continuous data. Dispersion curves over the model space and their corresponding errors are utilized in a Monte Carlo inversion scheme (*Shapiro and Ritzwoller, 2002*) using PREM as a starting model to compute smooth one dimensional velocity profiles on each tenth of a degree by tenth of a degree node from the surface to 150km depth. The profiles are concatenated together and corrected for topography to build a three dimensional model. To better visualize lateral variations

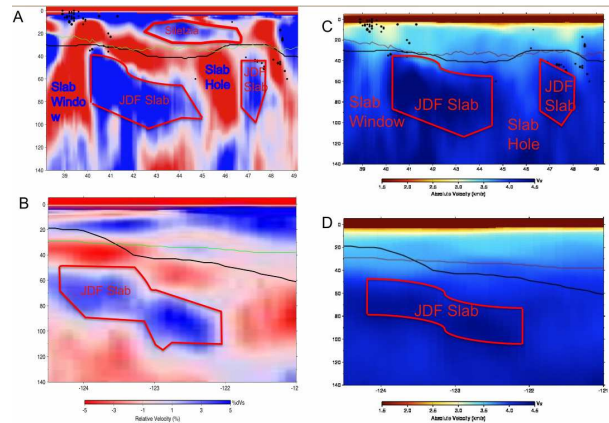


Figure 2.41: A - Longitudinal cross section along 123.2°W. B - Latitudinal cross section along 44.5°N. C - same as A, but in best fit velocity. D - same as B, but in best fit velocity. Key aspects of the model are highlighted. Thin red and thin green lines show the estimate of Moho based on greatest vertical gradient within ± 10 km of Crust2.0

in the mantle, a one-dimensional mean model is extracted and used to compute a three dimensional model of velocity relative to that one-dimensional model.

21.3 Results

Figure 2.40 shows two representative slices at constant depth in the Pacific Northwest. In the 35km depth slice, the semi-circular pattern of the Olympic Peninsula (OP), with faster rocks in the center and lower velocities around the outer part, is clearly seen, and the crustal root of the Klamath Mountains (KM) is also clear as a slow mass in the mantle. In the 100km depth section, the overlay of the main arc volcanoes closely matches the edge of the slab. Figure 2.41 shows two cross sections along 123.2°W and 44.5°N respectively. Figures 2.41 A and B are shown in velocity relative to a one-dimensional model, while C and D are in best fit velocity from the inversion. Overlain are the slab contours from *Audet et al*, 2009 in black and black circles showing earthquakes.

The structure is largely consistent with what would be expected; however, unexpected structural variations are apparent. Examples of expected structures include: deep crustal roots of the Klamath mountains, the border between the slab window and the slab following the trend of the Mendocino Fracture Zone, and the high velocity slab dipping the same way as the receiver functions suggest. The offset between the receiver function top of the slab and this image may reflect a layer of oceanic sediments of varying thickness overlying the main basaltic oceanic lithosphere in the subducting slab.

There is a reduction in the velocity of the subducting Juan de Fuca slab between 45°N and 47°N in a similar location as the weakening of the high velocity slab shown in *Obrebski and Allen*, 2009. There is also a high velocity lower crustal layer between 43°N and 47°N which correlates with the Siletzia terrain (*Brudzinski and Allen*, 2007). The Siletzia terrain has the longest recurrence interval of episodic tremor and slip (ETS) events throughout the subduction zone. Because this is a high shear wave velocity zone and ETS is less active in this zone, it is likely this is a region of lower fluid content than the rest of the subduction zone. Further analysis incorporating receiver functions and estimates of V_p/V_s ratio could confirm this finding.

21.4 Acknowledgements

We would like to acknowledge our co-PI's and collaborators on the flexible array experiments. The Mendocino Broadband experiment was made possible through NSF grants EAR0643392 and EAR0745934, with help from Gene Humphreys, Leland O'Driscoll, Alan Levander, and Yongbo Zhao for fieldwork and discussions. The FlexArray Along Cascadia was funded through NSF grant EAR0643007 with co-PI Mike Brudzinski and his students Devin Boyarko and Stefany Sit.

We thank Morgan Moschetti, Michael Ritzwoller, Yingji-Yang, Nikolai Shapiro, and Fan-Chi Lin for help with the ambient noise tomography processing flow to create the model. Data from this study came from the Earthscope USArray/Transportable Array, the Canadian National Seismic Network through the AutoDRM system, the Berkeley Digital Seismic Network, and the Southern California Earthquake Center.

Field assistance has been provided by the following: Derry Webb, Marcos Alvarez, Lloyd Carothers, Eliana Arias Dotson, Pat Ryan, Lisa Linville, Pallavi Chethan, Kevin Jensen, Chris McMillan, Stefany Sit, Andrew Tran, Summer Ohlendorf, Dan'L Martinez, Valerie Zimmer, Will Levandowski, Amanda Thomas, Heidi Reeg, Nickles Badger, Tom Owens, Eileen Evans, Holly Brown, Joanne Emerson, Ajay Limaye, Rick Lellinger, Mathias Obrebski, Samanta Cubias, Caroline Eakin, Liang Zhao, and David Belt.

This work has been made possible with the resources available through the PASSCAL instrument center at New Mexico Tech.

21.5 References

- Audet, P., Bostock, M. G., Christensen, N. I., and Peacock, S. M., Seismic evidence for overpressured subducted oceanic crust and megathrust fault sealing, *Nature*, 457, 76-78, 2009.
- Benson, G.D., Ritzwoller, M.H., Barmin, M.P., Levshin, A.L., Lin, F., Moschetti, M. P., Shapiro, N.M., Yang, Y., Processing seismic ambient noise data to obtain reliable broadband surface wave dispersion measurements, *Geophysical Journal International*, 169, 1239-1260, 2007.
- Bostock, M.G., Hyndman, R.S., Rondenay, S., and Peacock, S. M., An inverted continental Moho and serpentinization of the forearc mantle, *Nature*, 417, 53-539, 2002.
- Brudzinski, M. and Allen, R. M., Segmentation in Episodic Tremor and Slip All Along Cascadia, *Geology*. 35 (10) 907-910, 2007.
- Obrebski, M. J., and Allen, R. M., Plume Vs. Plate: Convection beneath the Pacific Northwest, *Berkeley Seismological Laboratory Annual Report*, 2009.
- Schmidt, M. E., Grunder, A.L., and Rowe, M., Segmentation of the Cascades Arc as indicated by Sr and Nd isotopic variation among primitive basalts, *Earth and Planetary Science Letters*, 266, 166-181, 2007.
- Shapiro, N. M., and Ritzwoller, M. H., Monte-Carlo inversion for a global shear velocity model of the crust and upper mantle, *Geophysical Journal International*, 151, 88-105, 2002.
- Xue, M., and Allen, R. M., The Fate of the Juan de Fuca Plate: Implications for a Yellowstone Plume Head, *Earth and Planetary Science Letters*, 264, 266-276, 2007.

22 Seismic Anisotropy Beneath Cascadia and the Mendocino Triple Junction: Interaction of the Subducting Slab with Mantle Flow

Caroline M. Eakin, Mathias Obrebski, Richard M. Allen, Devin C. Boyarko (Miami Univeristy, Ohio), Michael R. Brudzinski (Miami Univeristy, Ohio) and Robert Porritt

22.1 Introduction

The tectonic history of Cascadia is well characterized from plate reconstructions and tomography, but how subduction has affected mantle flow is relatively unknown. Such knowledge about the mantle flow field is primarily obtained from studies of mantle anisotropy using observations such as shear wave splitting. Cascadia and the Mendocino Triple Junction (MTJ) are generally lacking in such observations compared to other subduction zones worldwide, despite showing patterns that are unique to the global data set, i.e. trench normal fast directions beneath the slab (*Long and Silver, 2008*).

22.2 Data and Methods

Here we present shear wave splitting observations made using the datasets from FAME (Flexible Array Mendocino Experiment) and FACES (Flexible array Along Cascadia Experiment for Segmentation) networks (Figure 2.42). Data was available over the time period of Oct 2007-Sept 2008 for FAME and Nov 2007-July 2009 for FACES. Events of magnitude greater than 6.3, occurring within the given time period and in the epicentral distance range 85° to 130° were selected. Fifty suitable events were identified from which SKS and SKKS phases were analyzed. Calculations of shear wave splitting were performed using SplitLab (*Wüstfeld et al., 2007*). Splitting measurements at each station were then stacked following a quality assessment.

22.3 Results

A stacked result was obtained at 63 stations (Figure 2.42). The splitting pattern is highly uniform throughout Cascadia with a mean fast direction of $N67^\circ E$. This direction is normal to the trench and is comparable to the absolute motion of North American plate, the absolute motion of the Gorda-Juan de Fuca (G-JdF) plate (as shown by motion vectors on Figure 2.42), and also the subduction direction. The average delay time is 1.25 seconds.

On the west coast at the latitude of the MTJ, the observed fast direction dramatically rotates by almost 90 degrees. The mean splitting direction for stations south of the MTJ is $N71^\circ W$ with an average splitting time of 1.48 seconds. There is also a gradual rotation from the NW-SE orientation immediately south of the triple junction back to a NE-SW orientation at stations to the east

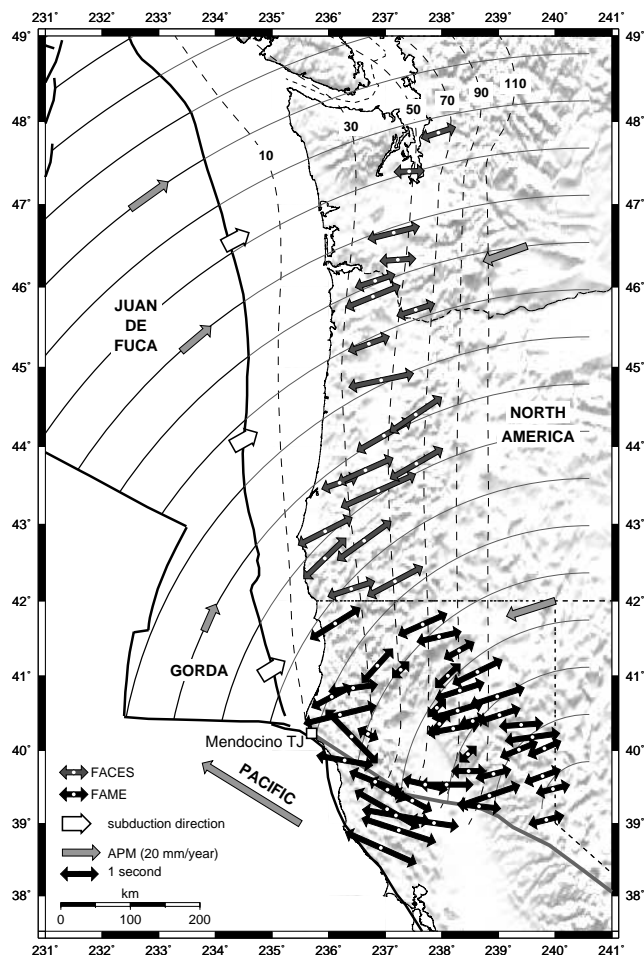


Figure 2.42: Tectonic map for the study region including stacked shear wave splitting results. Orientation of arrows represents the fast direction, and their length is proportional to the delay time. Thin black lines (motion vectors) have been drawn to emphasize the rotational movement of the G-JdF plate as determined from its absolute plate motion. Thick black lines are plate boundaries, interpolated edge of the G-JdF slab is in grey. Estimated depths of the top of the subducting slab are drawn as dashed lines.

across the southern half of the FAME network (Figure 2.42).

Figure 2.43 shows our results, previous splitting observations in the region (*Wang et al., 2008; West et al., 2009;*

Zandt and Humphreys, 2008 and references therein), and a vertical average (100-400 km) of tomographically imaged upper mantle velocities from the DNA09 P-wave model. The rotation of the splits south of the triple junction corresponds to the low velocity region that wraps around the southern end of the slab.

22.4 Sources of Anisotropy and Mantle Flow

After considering the multiple possible source regions of anisotropy in a subduction zone, the sub-slab mantle is considered to be the most likely candidate. It is the only region that is large enough (>200km) to produce the size of the observed delay times and is capable of generating the consistent splitting orientation throughout the subduction zone. As the fast direction is parallel to subduction of the G-JdF plate, this is consistent with entrained mantle flow beneath the slab as the source of the anisotropy.

The rotation of splitting south of the MTJ (Figure 2.43) suggests that the anisotropy is due to flow around the southern edge of the slab. During rollback, as the trench migrates in the direction of the oceanic plate, mantle material from below is forced around the edge of the slab into the mantle wedge which is under lower pressure. Such a mechanism has been inferred to account for trench-parallel splitting underneath subducting slabs, as the mantle tries to move around the slab which is undergoing rollback (Long and Silver, 2008). This study has produced evidence for flow around the slab edge from rollback but without trench parallel flow beneath the subducting plate. This is unique to Cascadia where the effect of rollback on the mantle flow field only appears to be at the slab edge.

Fig.2.43 also shows the regional pattern of splitting for the entire western US. The large scale circular pattern centered upon Nevada has been previously modeled as toroidal flow around the G-JdF slab (Zandt and Humphreys, 2008). More recently West et al. (2009) have interpreted a high velocity anomaly beneath central Nevada (Fig.2.43) as a lithospheric drip that could also explain the same circular pattern of splits. In our study we interpret the anisotropy as flow around the southern edge of the Gorda slab but on a smaller scale than previously proposed by Zandt and Humphreys (2008). The improved level of detail provided by our results allows us to distinguish that flow around the slab edge is a separate feature from anisotropy associated with the Nevada anomaly.

22.5 Acknowledgements

This work was funded by NSF awards EAR-0643392, EAR-0745934 and EAR-0643077. We extend our thanks to Andreas Wüstfeld for providing guidance concerning

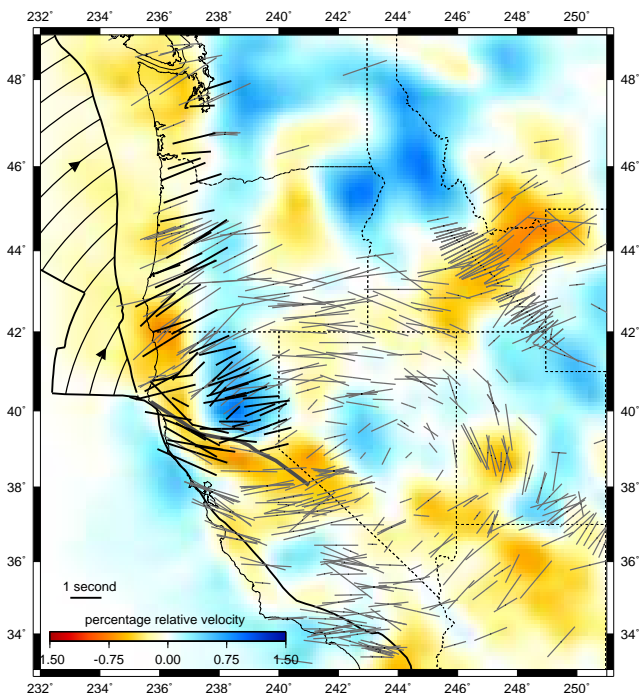


Figure 2.43: Regional splitting pattern overlain on the vertically averaged (100-400km depth) upper mantle velocity anomaly from DNA09 P-wave model. Our splitting results are shown in black and those of previous studies are in grey (see text). Curved black lines on the G-JdF plate represent the direction of its absolute plate motion.

SplitLab, and to Gene Humphreys, Maureen Long, John West and George Zandt for sharing their shear wave splitting data sets.

22.6 References

- Long, M.D., and P.G. Silver, The Subduction Zone Flow Field from Seismic Anisotropy: A Global View, *Science*, 319, 315-318, 2008.
- Wang, X., J.F. Ni, R. Aster, E. Sandvol, D. Wilson, C. Sine, S.P. Grand, and W.S. Baldrige, Shear-wave splitting and mantle flow beneath the Colorado Plateau and its boundary with the Great Basin, *Bull. Seis. Soc. Am.*, 98, 2526-2532, 2008.
- West, J.D., M.J. Fouch, J.B. Roth and L.T. Elkins-Tanton, Vertical mantle flow associated with a lithospheric drip beneath the Great Basin, *Nature Geoscience*, 2, 439-444, 2009.
- Wüstfeld, A., G. Bokelmann, C. Zaroli, and G. Barroul, SplitLab: A shear-wave splitting environment in Matlab, *Computers and Geosciences*, 34, 515-528, 2007.
- Zandt, G. and E. Humphreys, Toroidal mantle flow through the western US slab window, *Geology*, 36, 295-298, 2008.

23 Recovering the Attenuation of Surface Waves from One-Bit Noise Correlations: A Theoretical Approach

Paul Cupillard, Laurent Stehly and Barbara Romanowicz

23.1 Introduction

Cross-correlation of ambient seismic noise recorded by a pair of stations is now commonly recognized to contain the Green's function between the stations. Travel times extracted from such data have been extensively used to get images of the Earth interior. Some studies have also attempted to explore the information contained in the amplitude (Larose *et al.*, 2007; Gouedard *et al.*, 2008; Matzel, 2008; Prieto *et al.*, 2009). In a recent work, Cupillard and Capdeville (2009) carried out numerical experiments showing that the attenuation of surface waves can be recovered from one-bit noise correlations in the case of a uniform distribution of noise sources on the surface of the Earth (Figure 2.44). We here provide a theoretical explanation for such a surprising result.

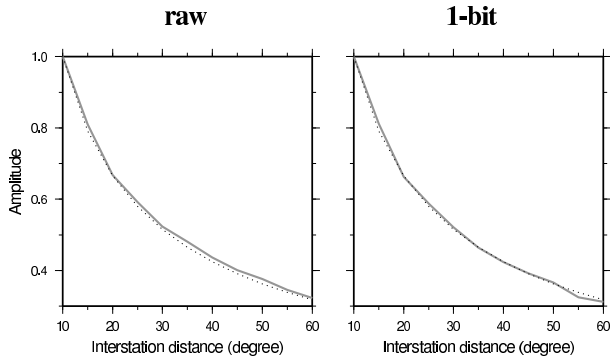


Figure 2.44: Results from Cupillard and Capdeville (2009). These authors generate synthetic noise on the surface of a 1D Earth model and compute correlations using a stream of twelve stations. Then, they compare the amplitude decay of the correlations (gray line) with the amplitude decay of the Rayleigh wave Green's functions (dotted line). The two curves match well, even when applying one-bit normalization to the noise records.

23.2 Amplitude of the raw noise correlation

Consider two receivers A and B that are separated by a distance Δ in a homogeneous medium in which the wave speed is v . Noise sources are distributed in this medium, and each receiver therefore records a time-signal. We denote by $A(t)$ (respectively $B(t)$) the recording from A (respectively B).

We assume that these signals can be decomposed in the following manner:

$$A(t) = A^c(t) + A^i(t) \quad (2.1)$$

$$B(t) = B^c(t) + B^i(t) \quad (2.2)$$

such that the cross-correlation $C_{AB}(t)$ between the signals can be written

$$C_{AB}(t) = \frac{1}{T} \int_0^T A^c(\tau) B^c(t + \tau) d\tau, \quad (2.3)$$

where T is the length of the signals. We designate $A^c(t)$ and $B^c(t)$ as coherent, whereas $A^i(t)$ and $B^i(t)$ are called incoherent.

We also assume that

$$B^c(t_0 + \tau) \propto A^c(\tau), \quad (2.4)$$

where $t_0 = \Delta/v$, so we have

$$C_{AB}(t_0) = \sigma_{A^c} \sigma_{B^c}, \quad (2.5)$$

where σ_{A^c} (respectively σ_{B^c}) is the standard deviation of $|A^c(t)|$ (respectively $|B^c(t)|$).

23.3 Amplitude of the one-bit noise correlation

Using notations and assumptions made in the previous section, we can now find out what the amplitude of the one-bit noise correlation contains.

One-bit normalization consists of retaining only the sign of the raw signal by replacing all positive amplitudes with a 1 and all negative amplitudes with a -1. Thus, we can write

$$C_{AB}(t) = \int \text{sgn}[A(\tau)] \text{sgn}[B(t + \tau)] d\tau \quad (2.6)$$

$$= n_1(t) - n_{-1}(t), \quad (2.7)$$

where $n_1(t)$ (resp. $n_{-1}(t)$) is the number of samples for which $\text{sgn}[A(\tau)] = \text{sgn}[B(t + \tau)]$ (resp. $\text{sgn}[A(\tau)] \neq \text{sgn}[B(t + \tau)]$).

For some samples τ , $|A^i(\tau)| > |A^c(\tau)|$ or $|B^i(t + \tau)| > |B^c(t + \tau)|$: at one of the two stations, the incoherent noise has a larger amplitude than the coherent noise and so controls the sign of the sample for this station. As the incoherent noise is random, the two events $\text{sgn}[A(\tau)] = \text{sgn}[B(t + \tau)]$ and $\text{sgn}[A(\tau)] \neq \text{sgn}[B(t + \tau)]$ have the same probability, so for this population of samples we have $n_1(t) = n_{-1}(t)$.

For the other samples, $|A^i(\tau)| < |A^c(\tau)|$ and $|B^i(t + \tau)| < |B^c(t + \tau)|$: the coherent noise controls the sign of both $A(\tau)$ and $B(t + \tau)$, so $\text{sgn}[A(\tau)] = \text{sgn}[A^c(\tau)]$ and $\text{sgn}[B(t + \tau)] = \text{sgn}[B^c(t + \tau)]$. Equation 2.4 yields $\text{sgn}[B(t_0 + \tau)] = \text{sgn}[A^c(\tau)]$, so for this population of samples we have $n_{-1}(t_0) = 0$.

Now we can write

$$C_{AB}(t_0) = nP_1P_2, \quad (2.8)$$

where n is the total number of samples in the correlation, P_1 is the probability that $|A^c(t)| > |A^i(t)|$ and P_2 is the probability that $|B^c(t)| > |B^i(t)|$. Assuming that coherent and incoherent noise are both gaussian, we are able to express P_1 and P_2 . Denoting by σ_{A^i} (respectively σ_{B^i}) the standard deviation of $|A^i(t)|$ (respectively $|B^i(t)|$), we find

$$C_{AB}(t_0) = n \left[1 - \frac{2}{\pi} \tan^{-1} \left(\frac{\sigma_{A^i}}{\sigma_{A^c}} \right) \right] \left[1 - \frac{2}{\pi} \tan^{-1} \left(\frac{\sigma_{B^i}}{\sigma_{B^c}} \right) \right] \quad (2.9)$$

23.4 The case of a uniform distribution of noise sources

Equation 2.9 has been established with no hypothesis on the distribution of noise sources. We have found that the amplitude of the one-bit noise correlation is related to physical quantities. In this section, we evaluate these quantities in the case of a uniform distribution of noise sources.

We assume that $A^c(t)$ is due to the contribution of all the noise sources in the coherent zone (denoted by Ω^c in the following) as defined by Snieder (2004). This coherent zone is an hyperboloid whose parameters depend on inter-station distance and frequency. Using the central-limit theorem, we write

$$\sigma_{A^c}^2 = \int_{\Omega^c} \sigma_A^2(x) dx. \quad (2.10)$$

In this equation, $\sigma_A(x)$ is the standard deviation of the signal recorded in A due to a source in x . Considering surface waves at the angular frequency ω , we have

$$\sigma_A(x) \propto \frac{1}{\sqrt{x}} \exp\left(-\frac{\omega x}{2vQ}\right), \quad (2.11)$$

where Q is the quality factor of the medium.

Using equation 2.11 in equation 2.10, we obtain

$$\sigma_{A^c}^2 \propto \Delta \cos^{-1} \left(\frac{\Delta - \frac{\lambda}{6}}{\Delta} \right) [K_1(\beta) + K_2(\beta)] e^\beta, \quad (2.12)$$

where λ is the wavelength, K_1 and K_2 are Bessel functions of the second kind and $\beta = \frac{\omega \Delta}{2vQ}$.

The same procedure enables us to compute σ_{B^c} , σ_{A^i} and σ_{B^i} . We finally get two analytical expressions for

$C_{AB}(t_0)$: one for the raw noise correlation and one for the one-bit noise correlation. We do not provide these expressions because they are too long, but we plot them in Figure 2.45. It is clear that the two amplitude decays correspond to the decay of the Rayleigh wave Green's function.

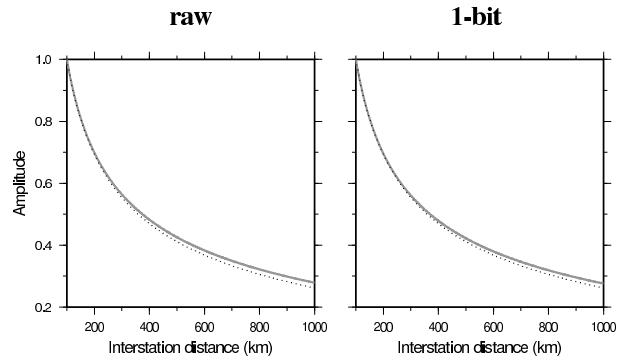


Figure 2.45: The amplitude decay of the correlations predicted by our theory (gray line) is compared with the decay of the Rayleigh wave Green's function (dotted line). The curves have been obtained using $\lambda = 50 \text{ km}$ and $Q = 300$.

23.5 References

- Capillard, P. and Y. Capdeville, On the amplitude of surface waves obtained by noise correlation and the capability to recover the attenuation: a numerical approach, *Geophys. J. Int.*, submitted.
- Gouépard, P., P. Roux, M. Campillo and A. Verdel, Convergence of the two-points correlation function toward the Green's function in the context of a prospecting dataset, *Geophysics*, 73(6), V47-V53, 2008.
- Larose, E., P. Roux and M. Campillo, Reconstruction of Rayleigh-Lamb dispersion spectrum based on noise obtained from an air-jet forcing, *J. Acoust. Soc. Am.*, 122(6), 3437, 2007.
- Matzel, E., Attenuation tomography using ambient noise correlation, *Seism. Res. Lett.*, 79(2), 358, 2008.
- Prieto, G. A., J. F. Lawrence and G. C. Beroza, Anelastic Earth structure from the coherency of the ambient seismic field, *J. Geophys. Res.*, 144, B07303, doi:10.1029/2008JB006067, 2009.
- Snieder, R., Extracting the Green's function from the correlation of coda waves: a derivation based on stationary phase, *Phys. Rev. E*, 69, 046610, 2004.

24 The Origin of Seismic Anisotropy in the D''

Sanne Cottaar, Paul Cupillard, Allen McNamara, Barbara Romanowicz, and Rudy Wenk

24.1 Introduction

The D'' zone at the base of the mantle is a boundary layer, both chemically and thermally. Complex dynamic processes are the cause of lateral heterogeneities, with sharp boundaries at the edge of superplumes (e.g. *Toh et al.*, 2005). Another characteristic of D'' is the presence of strong and laterally varying anisotropy. A global long-wavelength model for S-wave velocity and radial anisotropy shows that, in general, SH phases are faster than SV phases (*Panning and Romanowicz*, 2006). This observation leads to the idea that flow causes anisotropy by alignment of anisotropic minerals.

The goal of this research is to investigate seismic anisotropy and sharp velocity boundaries in the D'' region by combining geodynamics, mineral physics, and seismic modeling. Different seismic velocity models will be created to test hypotheses of possible microscopic and macroscopic processes. Comparing data computed for the models with real data will confirm or rule out these processes as a possibility for the lowermost mantle.

This contribution is an overview of ongoing research.

24.2 Geodynamics

The two-dimensional geodynamical model (provided by Allen McNamara) is refined to emphasize deformation in D'' (*McNamara and Zhong* 2004). Lagrangian tracers travel through the lowermost part of the model, providing strain information. Horizontal shear deformation increases near the CMB, while vertical deformation is strong in the upwelling region. An example of development along a tracer is shown in Figure 2.46. A great number of data points of several tracers are combined to create a static (snapshot) model.

24.3 Mineral Physics

Calculating the seismic velocities from the strain requires knowing elastic constants and deformation mechanisms at the temperature and pressure conditions of D''. These are measured for the most abundant minerals: perovskite ($MgSiO_3$) and periclase (MgO).

We predict the seismic response of a suite of different mineral phases and assemblages. Post-perovskite is proposed as one of the possible anisotropic minerals. In fast regions, the top of the D'' is characterized by a velocity discontinuity, possibly caused by the pPv transition of $MgSiO_3$ (e.g. *Wookey et al.*, 2005). For pPv we will try different elastic constants and deformation systems. Disparate results for elastic constants are found compu-

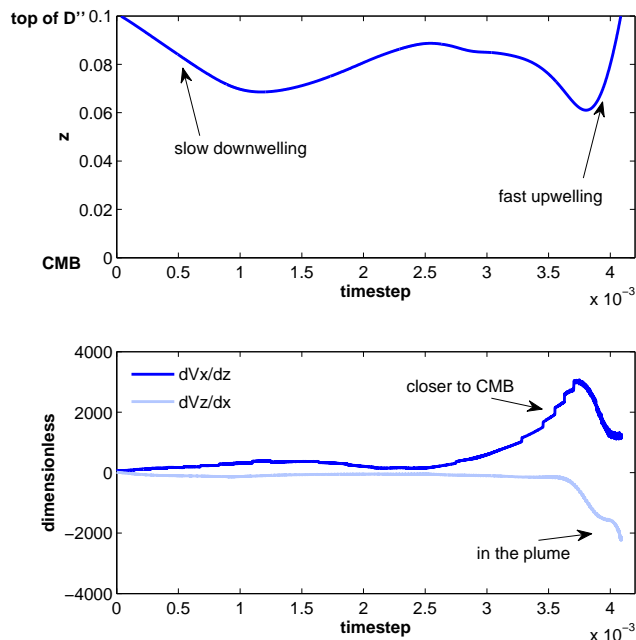


Figure 2.46: Top figure shows the depth of the Lagrangian tracer in the geodynamical model with time. The bottom figure shows the development of strain. Horizontal strain is higher deeper in the mantle and vertical strain increases in the plume.

tationally by *Stackhouse et al.* (2005) and *Wentzocovitch et al.* (2006). Various slip-systems are found by theoretical work and in deformation experiments (e.g. *Merkel et al.*, 2007). It has also been suggested that ferropericlase, (Mg, Fe)O, might be the dominant cause of seismic shear anisotropy (e.g. *Marquardt et al.*, 2009).

Although other origins of anisotropy, like SPO and melt inclusions, have been proposed, they are not considered in this project.

24.4 Synthetic Data

Slices of two-dimensional velocity models extend the model in the third dimension and will be implemented in sandwiched C-SEM (Coupled Spectral Element Method, *Capdeville et al.*, 2003). Sandwiched-CSEM couples the SEM part in the lower mantle to a computationally faster 1D normal mode solution in the rest of the Earth. Eventually, the data will be calculated down to periods of ~ 10 seconds. The predicted waveforms will be compared to observations.

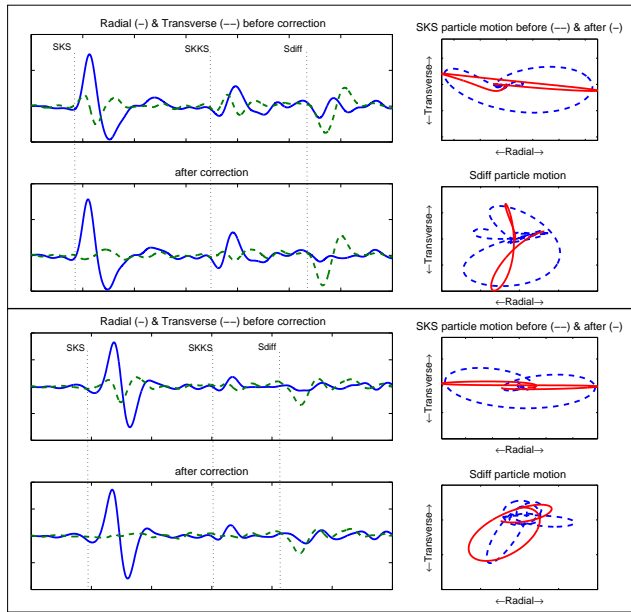


Figure 2.47: Observations for 7.1 M_w event at 530 km depth in Mindanao, Philippines. Top four figures show data before and after correction for station HLID at a distance of 108° . The lower four are for station A04A at 101° .

24.5 Real Data

Several phases are used to study the D $''$. The S-wave, the core-reflected S (ScS) and the diffracted phase (Sdiff) have shown that D $''$ is anisotropic.

Data from deep earthquakes are needed to avoid source-side anisotropy in the upper mantle. Unfortunately, the azimuthal coverage of this data is not very good. Vertical transverse isotropy (VTI) can, however, be measured along one path by the splitting of S-waves into SH and SV phases. Coverage has been greatly improved by the USArray, providing a large number of stations at the correct distance from deep earthquakes in the region of Indonesia and Fiji-Tonga. These paths cover the boundaries of the Pacific superplume.

Before measuring anisotropy in D $''$, the phases need to be corrected for the receiver side anisotropy. The SKS has a shorter path in D $''$, but an almost similar path through the upper mantle. Therefore, we correct the Sdiff phase with values measured for SKS at similar azimuth using (a modified version of) SplitLab (Wüsterfeld *et al.*, 2007). Figure 2.47 shows examples of how this decreases and increases anisotropy in D $''$.

24.6 Future Work

Besides varying a number of assumptions with the models, several major improvements are needed to make

the models more realistic. One of the improvements will be to use a three-dimensional model providing more realistic strains.

Possible mineral phase transitions will be implemented. This could test the occurrence of sharp horizontal and vertical velocity boundaries or transitional zones.

24.7 Acknowledgements

This project is funded by NSF's CSEDI program under grant number NSF EAR-0757608.

24.8 References

- Capdeville, Y., B. Romanowicz, and A. To, Coupling spectral elements and modes in a spherical earth: an extension to the "sandwich" case, *Geophys. J. Int.*, 154, 44-57, 2003.
- McNamara, A.K. and S. Zhong, The influence of thermochemical convection on the fixity of mantle plumes, *EPSL* 222, 485, 2004.
- Merkel S., A.K. McNamara, A. Kubo, S. Speziale, L. Miyagi, Y. Meng, T. S. Duffy, H.-R. Wenk, Deformation of (Mg,Fe)SiO $_3$ post-perovskite and D $''$ anisotropy, *Science*, 316, 1729-1732, 2007.
- Marquadt, H., S. Speziale, H. J. Reichmann, D. J. Frost, F. R. Schilling and E. J. Garnero, Elastic Shear Anisotropy of Ferropicrcline in Earth's Lower Mantle, *Science*, 324, 224, 2009.
- Panning, M. and B. Romanowicz, A three dimensional radially anisotropic model of shear velocity in the whole mantle, *Geophys. J. Int.*, 167, 361-379, 2006.
- Stackhouse, S., J.P. Brodholt, J. Wookey, J.-M. Kendall and G.D. Price, The effect of temperature on the seismic anisotropy of the perovskite and post-perovskite polymorphs of MgSiO $_3$, *EPSL* 230, (1-2), 1-10, 2005.
- Toh, A., B. Romanowicz, Y. Capdeville and N. Takeuchi, 3D effects of sharp boundaries at the borders of the African and Pacific Superplumes: observation and modeling, *Earth and Planet. Sci. Lett.*, 233, 137-153, 2005.
- Wentzcovitch, R.M., B.B. Karki, M. Cococcioni, and S. de Gironcoli, Thermoelastic properties of MgSiO $_3$ -perovskite: insights on the nature of the Earth's lower mantle, *PRL* 92, doi:10.1103/PhysRevLett92.018501, 2004.
- Wookey, J., S. Stackhouse, J. Kendall, J. Brodholt, and G. D. Price, Efficacy of the post-perovskite phase as an explanation for lowermost-mantle seismic properties, *Nature*, 438, 1004, 2005.
- Wüsterfeld, A., G. Bokelmann, C. Zaroli and G. Barrool, SplitLab: A shear-wave splitting environment in Matlab, *Computers and Geosciences* 34(5), 515-528, 2007.

25 Toward a 3D Global Attenuation Model in the Lower Mantle from the Earth’s Free Oscillations

Shan Dou and Barbara Romanowicz

25.1 Introduction

In the past two decades, seismic velocity tomography has benefited from rapidly growing data quality, coverage, and computational capability, and has provided snapshots of the present velocity variations in the Earth’s mantle. On the other hand, the study of attenuation has lagged behind that of the elastic velocities because of more complexity in its measurements and interpretation. However, attenuation is important for at least two reasons:

1) Attenuation is considerably more sensitive to temperature variations than elastic velocities. While elastic velocities have a quasi-linear dependence upon temperature variations, seismic attenuation depends exponentially on temperature (e.g., *Jackson, 1993; Karato, 1993*). Therefore, attenuation tomography is important for studying temperature variations within the Earth, and combining elastic and anelastic studies has the potential to separate different effects of chemical composition, water content, partial melting, etc.

2) Attenuation causes physical dispersion of seismic velocities, and this effect needs to be corrected for velocity models.

25.2 Methods and Work Plan

Lower mantle imaging is especially difficult compared with that of the upper mantle because surface waves lose their sensitivity to such deep structures. Therefore, lower mantle tomography mostly relies on deep-turning teleseismic body waves and normal mode data. In addition to the contamination from the upper-mantle structure, body-wave datasets suffer from an uneven distribution of events and stations, which can bias the images by over-interpreting the unsampled regions in the lower mantle. Since the Earth’s free oscillations involve the vibration of the whole planet, mode observations have the capacity to resolve deeper structures in the mantle at long wavelengths, and are much less likely to be biased by the uneven distribution of earthquake sources and seismic receivers.

Contamination caused by elastic effects and source complexity can lead to large uncertainties in attenuation measurements. Even if we minimize the uncertainties caused by the source term, elastic processes, especially the effects of scattering and multipathing (i.e. the focusing/defocusing phenomena due to the transverse gradients of elastic structure), are not well constrained, and yield generally very noisy attenuation datasets. There-

fore, we will first start by establishing a new and higher-quality three-dimensional lower mantle elastic structure from modal constraints. This new lower mantle tomographic model can not only serve as a prerequisite for resolving attenuation structure, but can also be used to test the quality of the data set and the accuracy of our measurement and inversion methods.

The constraints on the Earth’s three-dimensional structure extracted from normal modes data mainly rely on detailed analysis of the free oscillation spectrum. In a spherically symmetric, non-rotating, purely elastic, and isotropic idealized 1-D earth model (the SNREI model), the spectrum of each mode is expected to be a sharp and narrow peak. However, the spectra peaks of the real earth demonstrate splitting, broadening, and overlapping in the observed modes, which indicates that the fine structure of the spectra of these records carries important information on the interior three dimensional elastic and anelastic structure of the Earth. Owing to the high quality digital data set assembled in the last 20 years on the global broadband seismic network, and owing to the occurrence of several very large earthquakes, especially the 2004 great Sumatra-Andaman earthquakes mentioned above, putting new constraints on the large-scale attenuation in the lower mantle from normal modes is promising.

Three main stages are involved in retrieving structural information from modal data: 1) Gather many spectra from time series of a large earthquake ($M_w \geq 7.5$); 2) Retrieve spectra of a mode or modes combination from the spectra, and repeat the process for many other large events; 3) Repeat for other modes, build up a greatly expanded catalogue of normal modes sensitive to the lower mantle, and invert for the 3D model of the lower mantle.

25.3 Preliminary Results and Prospective Work

Two main approaches frequently used in deriving tomographic models from normal mode spectra will both be applied, and results will be compared with each other: (1) The “one-step” method: directly derive tomographic models from fitting modal spectra by solving a non-linear inverse problem in a least-square iterative way (e.g. *Li et al. 1991, Hara and Geller 2000; Kuo and Romanowicz 2002*); (2) The “two-step” method: the splitting matrix

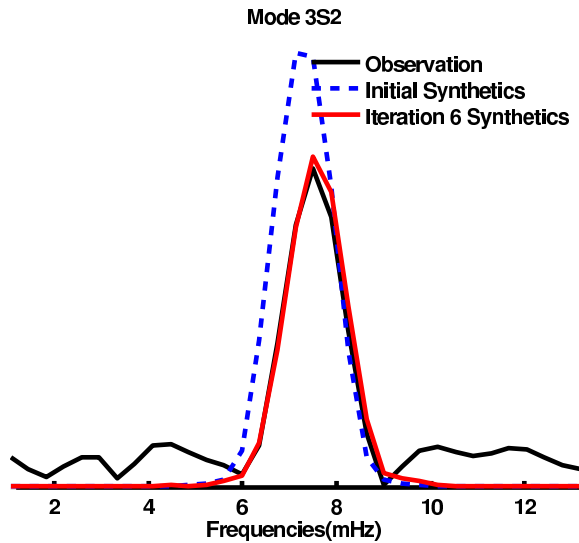


Figure 2.48: Modeling of the spectrum of multiplet $3S_2$ with the ISF procedure, for a recording of the 9 October 1994 Kuril Island earthquake at station SBC (Santa Barbara, US). Black line: Observed amplitude spectrum; dashed blue line: spectrum generated from the initial splitting coefficients used in the ISF procedure; red line: spectrum after six iterative fittings.

is simplified into its equivalent function on the sphere, known as the “splitting function” (Woodhouse and Giardini 1985). It is a similar procedure to that commonly used in surface wave tomography, in which one first determines 2D maps of phase velocity over a range of frequencies and then uses these to infer the 3D structure perturbations needed to explain the inferred phase velocity maps. Because the nonlinear stage of this approach only needs a relatively smaller number of parameters represented by the splitting function, the computation cost is smaller than the “one-step” method.

We start with the “two-step” method for the elastic structure inversion, where the Iterative Spectral Fitting (ISF) method (Ritzwoller et al. 1986, 1988) is applied in the process of splitting function inversion. Figure 2.48 shows an example of the ISF method. For mode $3S_2$, we can clearly see the improvement of spectra fitting within six iterations. The associated splitting function images are shown in Figure 2.49.

We hope to obtain constraints on the long wavelength attenuation structure at the base of the mantle by combining the mode data with the Berkeley waveform dataset, which provides constraints on upper mantle attenuation (following the Ph.D. work of Vedran Lekic). Even if we can only resolve the longest wavelengths (degrees 2 or possibly up to 4), this will be important for the understanding of the nature of the two low velocity regions at the base of the mantle, commonly referred

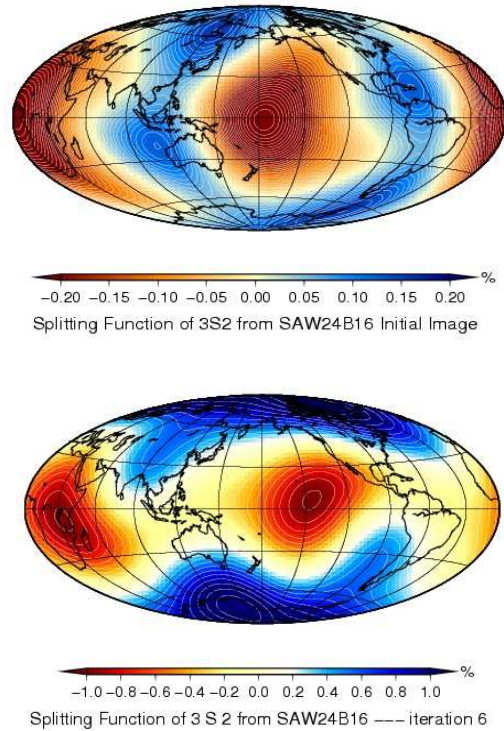


Figure 2.49: Splitting function for mode $3S_2$. Upper panel: splitting function obtained from the initial splitting coefficients (the model is the Berkeley mantle model SAW24B16); Lower panel: splitting function after six iterations of ISF procedure.

to as “superplumes,” whose thermo-chemical nature is still under debate (e.g. Masters et al. 1982, Romanowicz 1998, Bijwaard and Spakman 1999, Ishii and Tromp 1999, Romanowicz 2001, Trampert et al. 2004, Gung and Romanowicz 2004, Anderson 2005).

25.4 References

- Ritzwoller M, Masters G, and Gilbert F, Observations of anomalous splitting and their interpretation in terms of aspherical structure with low frequency interaction coefficients: Application to uncoupled multiplets, *Journal of Geophysical Research*, 91, 10203-10228, 1986.
- Ritzwoller M, Masters G, and Gilbert F, Constraining aspherical structure with low frequency interaction coefficients: Application to uncoupled multiplets, *Journal of Geophysical Research*, 93, 6369-6396, 1988.
- Romanowicz B and Mitchell B, Deep Earth Structure — Q of the Earth from Crust to Core, *Treatise on Geophysics, Volume 1*, 775-803, 2007.
- Widmer-Schmidrig R and Laske G, Theory and Observations — Normal Modes and Surface Wave Measurements, *Treatise on Geophysics, Volume 1*, 67-125, 2007.

26 Anisotropic North American Lithosphere and its Boundary with Asthenosphere

Huaiyu Yuan and Barbara Romanowicz

26.1 Introduction

Since the pioneering work by *Vinnik* (1984) and *Sliver* (1988), seismic anisotropy has been extensively used to infer upper mantle strain induced fabrics caused by the past and present time mantle deformation processes (e.g. *Park and Levin*, 2002). Successful correlation of the mapped seismic anisotropy field with many tectonic phenomenon in North America (e.g., edge flow of the continent keels (*Fouch et al.*, 2000); lithospheric drip (*West et al.*, 2009); toroidal flow (*Zandt and Humphreys*, 2008); fossil slab stacking (*Bostock* 1998; *Snyder* 2003, 2008; *Gorman et al.*, 2002; *Mercier et al.*, 2009); rifting (*Gok et al.*, 2003); hotspot tracks (*Walker* 2004; *Schutt et al.*, 1998; *Eaton and Federiksen* 2007); lithosphere thickening (*Deschamps et al.* 2008); and lithosphere-asthenosphere-boundary topography (*Plomerova et al.*, 2002)) has greatly improved our understanding of the dynamics and revolution of the continent.

Using long-period surface waveform tomographic inversion, here we show that the seismic anisotropy beneath North American cratons is strongly stratified, characterized by abrupt changes of fast velocity symmetry axis with depth. At the lithosphere and asthenosphere boundary (LAB), the observed craton-wide change of the anisotropy fast axis towards the absolute plate motion direction defines an anisotropic LAB of the North American upper mantle.

26.2 Tomographic Approach

We perform a two-stage inversion to acquire the 3-D azimuthal anisotropy structure in the North American Continent upper mantle. First we simultaneously invert over 150000 3-component long period surface wave fundamental and overtone waveforms to obtain the isotropic V_s and radial anisotropy X_i structure. Then we further perturb the optimal V_s and X_i model (shown in the next research contribution) from the first step for two azimuthal 2-psi coefficients G_c and G_s . Station averaged shear wave splitting measurements are added, which greatly improves the inversion resolution to the deeper mantle (*Marone and Romanowicz*, 2007).

26.3 North American Azimuthal Anisotropy: Lithospheric Stratification

Figure 2.50 shows the inverted azimuthal anisotropy structure at selected depths. Those depths are chosen to present upper and lower lithosphere and asthenosphere depths based on estimates from other studies, including

seismic velocity, petrology and lithosphere electrical resistivity (e.g., *van der Lee*, 2002; *Griffin et al.*, 2004; *Darbyshire et al.*, 2000, 2007; *Snyder* 2008; *Chen et al.*, 2008; *McKenzie and Priestley* 2008). At shallow depth (70 km, Figure 2.50a), the craton fast axis is generally plate motion direction parallel, except beneath the east central US and the Labrador Sea/Baffin Island, where the fast axis is pointing north. In the lower lithosphere (150km), the craton region has a nearly uniform north-pointing fast axis, with exclusions of east-west striking fast axis beneath North Dakota Trans-Hudson Orogen and north-east Grenville province. At deeper depth (250km), the fast axis aligns everywhere to the plate motion direction. These images thus demonstrate stratified anisotropic layers beneath the continent, with two lithospheric layers clearly presented in some of the cratons.

26.4 North American Azimuthal Anisotropy: Anisotropic LAB

To further constrain the change between the lithosphere and asthenosphere anisotropy, we look for the gradient of the fast velocity axis near the cratonic LAB depths estimated from other studies, with combined constraints from our isotropic velocity V_s and radial anisotropy X_i (see *Eaton* (2009) for various seismic definitions of the LAB). Results shown in Figure 2.51 are derived from our tomographic inversion results only.

Our anisotropic LAB is consistently uniform in the depth range of 180-240 km beneath the cratons, except the Wyoming craton, whose LAB is substantially shallower (Figure 2.51a). A depth profile across the major cratons of the study area clearly shows a two layer anisotropy domain in the Archean craton lithosphere, and the abrupt transition of the fast axis to the plate motion direction parallel across the LAB. The unique two-layer pattern of the lithospheric anisotropy may suggest multiple-stage continent lithosphere formation processes (e.g., *Arndt* 2009). Alternatively, *Thybo* (2006) suggests a ubiquitous low velocity zone at 100 km depth due to lowered solidus of normal mantle rocks by the presence of limited amounts of fluids. This is consistent with the velocity drop around 100km depth in our isotropic V_s image (upper right panel in Figure 2.50b); however causes of the anisotropy change associated with the low velocity zone are unknown. The anisotropy stratification changes when going into the late Proterozoic Grenville and even younger Appalachian orogens, reflecting somehow different lithosphere formation processes in this area.

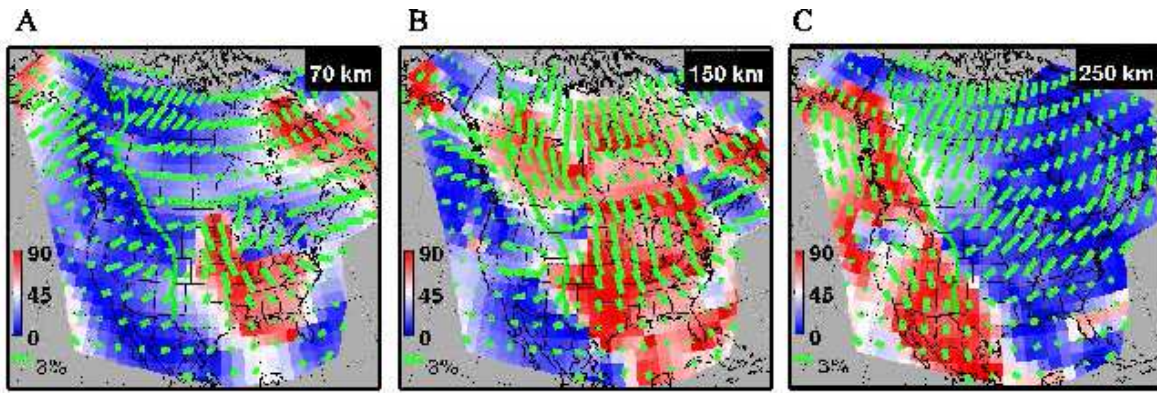


Figure 2.50: Azimuthal anisotropy at selected depths. Sticks on each sub-plot show both the fast velocity symmetry axis direction and the anisotropy strength. The deviation of the inverted fast axis from the absolute plate motion direction (*Gripp and Gordon, 2002*) is drawn in the background such that blue regions show a fast axis parallel to the absolute plate motion direction and red regions perpendicular to it. The Rocky Mountain front (green curve) separates the stable cratons and active west Cordillera.

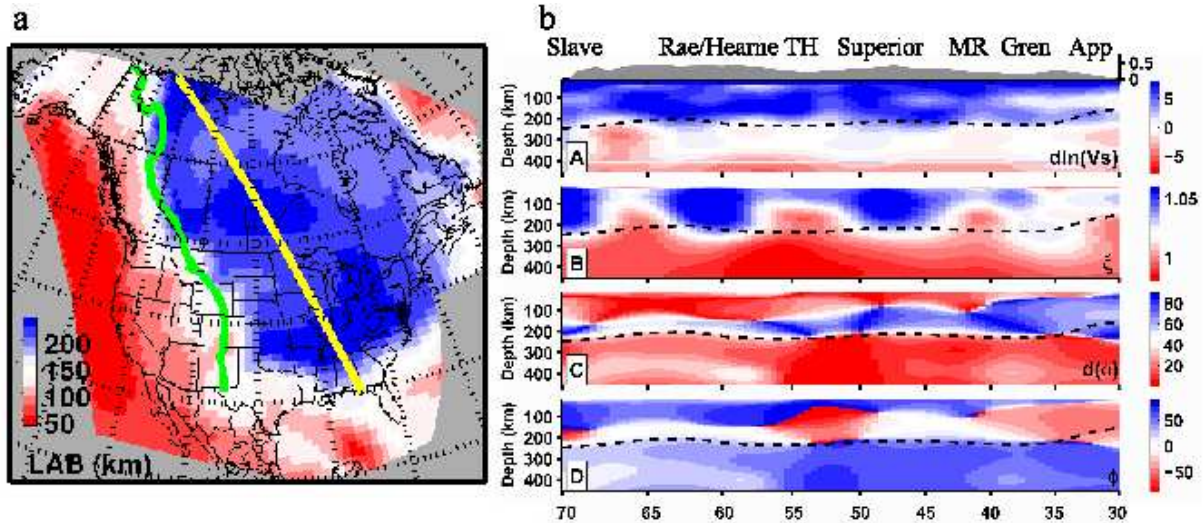


Figure 2.51: LAB estimates. A cratonic cross section through the yellow line is shown in b. From top to bottom, isotropic V_s variation, radial anisotropy (with respect to isotropy), deviation of the fast axis direction from the plate motion direction, and the absolute value of the inverted fast axis direction. Black dotted line is the LAB measurements shown in a. TH, Trans-Hudson Orogen, MR, Mid-continent Rift, Gren, Grenville Orogen, and App, Appalachian Orogen.

26.5 Conclusions

Overall, our tomographic inversion reveals a layered anisotropic cratonic upper mantle. The strong lithospheric layering suggests different stages of the cratonic formation. Detecting anisotropy changes from surface wave tomography makes it possible to obtain large scale and high resolution LAB measurements at once.

26.6 Acknowledgements

We thank the IRIS DMC and Canadian National Data Center for providing the waveform data. This project is supported by NSF EAR-0643060.

26.7 References

References are listed in the Section 27.5.

27 Crustal Stress and Mechanical Anisotropy of the Lithosphere in Western North America

Pascal Audet

27.1 Introduction

The flexural rigidity of continental lithosphere can be estimated from isostatic transfer functions (admittance, coherence) relating topography and gravity anomalies using the equation for the flexure of a thin elastic plate. There is growing evidence that such transfer functions are anisotropic, and inferred weak directions correlate with principal directions of crustal stress, indicating either more complicated models of loading, and/or anisotropic rigidities. Here we derive isostatic response functions using the equations for the flexure of a thin elastic plate that incorporate the effects of in-plane loading. We then calculate local 1-D and 2-D wavelet admittance and coherence functions in western North America, and invert for either rigidity anisotropy or in-plane force.

27.2 Isostatic response functions

Flexural isostasy describes the condition that loads must be supported at some depth within the lithosphere via elastic plate flexure. The flexural rigidity $D \propto ET_e^3$, where E is Young's modulus and T_e is the elastic thickness, is a rheological property that governs the resistance of the plate to bending. A popular method of estimating the flexural rigidity is based on calculating transfer functions relating gravity and topography and inverting using isostatic response functions obtained from plate flexure equations (Forsyth, 1985). In the case where an isotropic plate is loaded both horizontally by in-plane force n and surface load q , the flexure equation is written

$$D\nabla^4 w(\mathbf{r}) = q(\mathbf{r}) + n(\mathbf{r}), \quad (2.13)$$

where w is plate deflection at the Moho, and $\mathbf{r} = (x, y)$. For an orthotropic plate, equation (2.13) becomes

$$\left[D_x \frac{\partial^4}{\partial x^4} + 2B \frac{\partial^4}{\partial x^2 \partial y^2} + D_y \frac{\partial^4}{\partial y^4} \right] w(\mathbf{r}) = q(\mathbf{r}) + n(\mathbf{r}),$$

where D_x and D_y are rigidities in two perpendicular directions, and B is the torsional rigidity approximated by $B \approx \sqrt{D_x D_y}$. The vertical load at the surface is given by

$$q(\mathbf{r}) = \rho_c g h(\mathbf{r}) - (\rho_m - \rho_c) g w(\mathbf{r}),$$

where g is gravitational acceleration, h is the topography, ρ_c and ρ_m are crustal and mantle density, respectively, and we will use the shorthand $\Delta\rho = \rho_m - \rho_c$. In-plane forces are given by

$$n(\mathbf{r}) = \left[N_x \frac{\partial^2}{\partial x^2} + N_y \frac{\partial^2}{\partial y^2} + 2N_{xy} \frac{\partial^2}{\partial x \partial y} \right] w(\mathbf{r}),$$

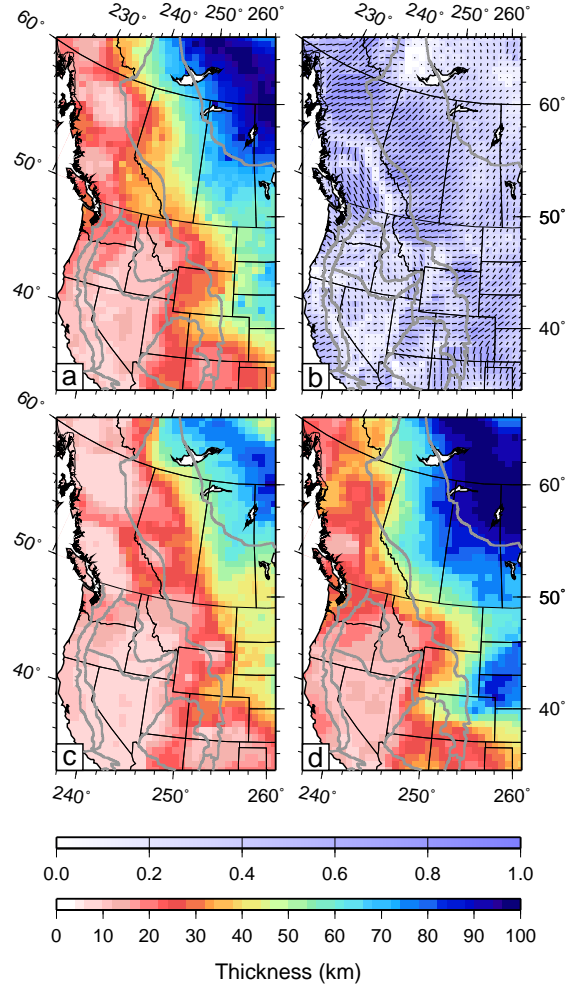


Figure 2.52: Elastic thickness results for western North America. a) Isotropic T_e ; b) Direction of T_{min} (β); c) T_{min} ; d) T_{max} . Shading in b) is given by $(T_{max} - T_{min})/T_{max}$. Grey lines indicate major tectonic boundaries.

where N_x , N_y represent axial loads (compression is negative) in the x and y directions, respectively, and N_{xy} denotes shear loading. Solving these equations in the Fourier domain yields linear isostatic response functions relating Moho deflection to surface topography that take the form

$$\Theta(\mathbf{k}) = \frac{\rho_c}{\Delta\rho} \left[1 + \frac{\psi(D_x, D_y, \mathbf{k})}{\Delta\rho g} + \frac{\zeta(N_x, N_y, N_{xy}, \mathbf{k})}{\Delta\rho g} \right]^{-1},$$

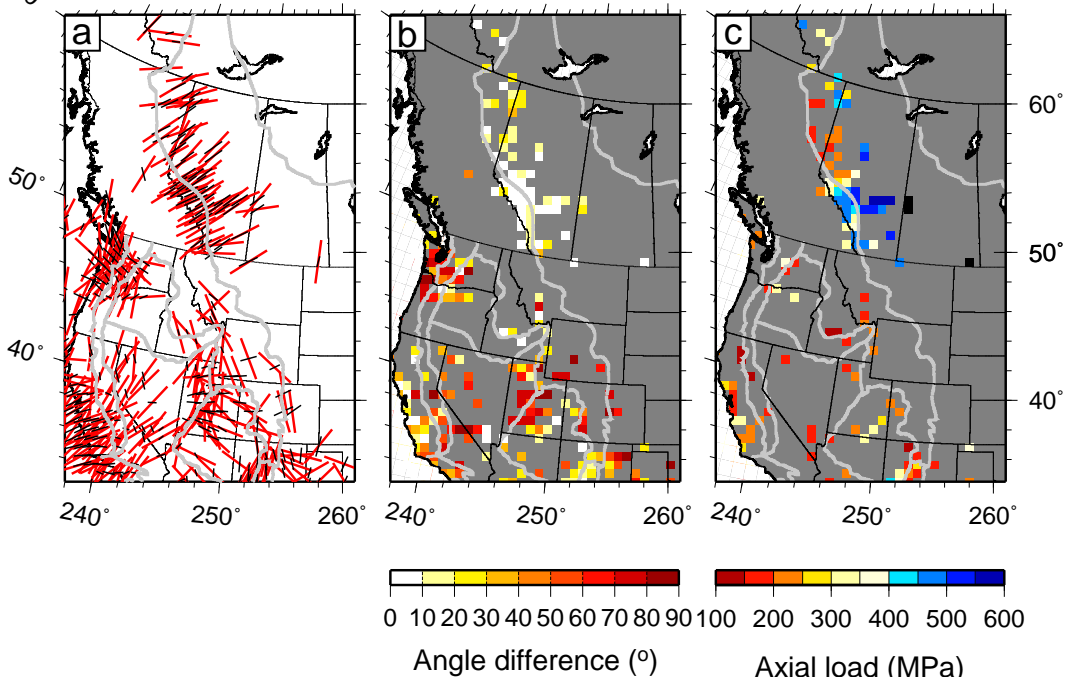


Figure 2.53: Comparison between β and orientation of maximum horizontal compressive stress. a) shows crustal stress indicators (red bars) and co-located weak directions (black bars); b) is the angular difference between both indicators; and c) is the estimated in-plane load necessary to fit the observed 2-D admittance and coherence.

where $\mathbf{k} = (k_x, k_y)$, and $|\mathbf{k}| = k$. The functions ψ and ζ correspond to

$$\psi = \begin{cases} Dk^4 & \text{isotropic plate} \\ (\sqrt{D_x}k_x^2 + \sqrt{D_y}k_y^2)^2 & \text{orthotropic plate.} \end{cases}$$

$$\zeta = \begin{cases} 0 & \text{no in-plane force,} \\ N_x k_x^2 + N_y k_y^2 + 2N_{xy} k_x k_y & \text{with in-plane force.} \end{cases}$$

For subsurface loading the isostatic function is

$$\Phi(\mathbf{k}) = \frac{\rho_c}{\Delta\rho} \left[1 + \frac{\psi(D_x, D_y, \mathbf{k})}{\rho_c g} + \frac{\zeta(N_x, N_y, N_{xy}, \mathbf{k})}{\rho_c g} \right].$$

Isostatic response functions are combined to form theoretical admittance (Q) and coherence (γ^2) functions between Bouguer gravity and topography

$$Q(\mathbf{k}) = 2\pi\Delta\rho G e^{-|\mathbf{k}|z_c} \frac{(\Theta + \Phi f^2 \Theta^2)}{(1 + f^2 \Theta^2)}, \quad (2.14)$$

$$\gamma^2(\mathbf{k}) = \frac{(1 + \Phi \Theta f^2)^2}{(1 + f^2 \Theta^2)(1 + f^2 \Phi^2)}, \quad (2.15)$$

where f is the ratio between surface and subsurface loads, G is the gravitational constant, and z_c is the depth of compensation, taken at the Moho.

27.3 Results for western North America

We calculated the wavelet admittance and coherence in western North America following the method of *Audet and Mareschal* (2007) and inverted the corresponding isostatic quantities to yield estimates of D for the

isotropic case, and D_{min}, D_{max} and β (i.e. the direction of D_{min}) for the orthotropic case. We give results in terms of elastic thickness using the relation $D = \frac{ET^3}{12(1-\nu^2)}$, where T can be either T_e , or T_{min}, T_{max} (Figure 2.52). Low values ($T_e < 30$ km) are found across most of western North America, increasing toward the continental interior. In the northeastern craton, T_e values can reach 100 km. Maps of T_{min} and T_{max} follow the same general patterns as the isotropic T_e , whereas β is oriented dominantly SW-NE, except in the highly deforming regions of western United States, where it is highly variable in both magnitude and direction.

We further compared the weak direction with orientations of maximum horizontal compressive stress from the World Stress Map project <http://dc-app3-14.gfz-potsdam.de/>. We re-sampled stress indicators onto the T_e grid and calculated the angular difference between both directions (Figure 2.53a,b). There is good agreement in the Canadian Cordillera and near the coast of California, both regions where stress regime is compressional. An exception is the arc and forearc in the Pacific Northwest, where compressive stress directions are parallel to the coast whereas weak directions are perpendicular, perhaps reflecting more complex loading near the subduction zone. Angle difference is large ($> 45^\circ$) in extensional regimes, such as Basin and Range and western Colorado Plateau.

These correlations allow us to use isostatic functions for the isotropic plate with axial loading to fit the 2-

D coherence and admittance in order to estimate load magnitudes where angular difference is within 30° . We use isotropic T_e and β obtained previously, and estimate total axial load (Figure 2.53c). Preliminary results indicate loads on the order of 100-600 MPa, which are up to three times larger than estimates from dynamical models of deformation using a uniformly thick (100 km) elastic plate (Humphreys and Coblenz, 2007). Such large discrepancy also suggests that, in addition to lithospheric stress, significant rigidity anisotropy must be involved in producing anisotropy in the observed transfer functions. Lastly we note that shear loads were not modeled at this point, which will be the focus of future efforts.

27.4 Acknowledgements

This work was funded by the Miller Institute for Basic Research in Science (UC Berkeley).

27.5 References

Audet, P., and J.C. Mareschal, Wavelet analysis of the coherence between Bouguer gravity and topography: Applications to the elastic thickness anisotropy in the Canadian Shield, *Geophys. J. Int.*, 168, 287-298, 2007.

Forsyth, D.W., Subsurface loading and estimates of the flexural rigidity of continental lithosphere, *J. Geophys. Res.*, 90, 12, 623-12, 632, 1985.

Humphreys, E.D., and D. Coblenz, North American dynamics and western U.S. tectonics, *Rev. Geophys.*, 45, RG3001, 2007.

28 Berkeley 3-D Isotropic and Anisotropic S-velocity Model of North American Upper Mantle, Updated to June 2008

Huaiyu Yuan and Barbara Romanowicz

28.1 Introduction

We present here the isotropic and radial anisotropy part of our 3-D North American upper mantle shear wave velocity model. This new model is constructed starting from a new global 1D reference Earth model, based on a combination of seismic and mineral physics data (Cammarano and Romanowicz, 2007), which is smooth at 220 km, and a crustal correction approach that takes into account the non-linearities involved (Lekic and Romanowicz, submitted).

28.2 North American Isotropic Vs and Radial Anisotropy model

The pronounced findings of the Vs model include: 1) high velocity cratonic roots extend to 200-250 km depth range (A-E); 2) at shallow depth (< 200km; A-D) low velocities flank the cratonic region from the west and the south, with a sharp transition along the Rocky Mountain Front; 3) a high velocity feature exists from 450 to 600 km (H) in transition zone beneath the western US; and 4) small scale (100km) velocities correlate with surface geological features, e.g., the Rio Grande rift, Colorado Plateau, and the Eastern Snake River Plain in the western US.

The radial anisotropy model (I-L) is plotted with respect to an isotropic reference. The dominant feature above 200 km is the faster V_{sh} than V_{sv} or $X_i > 1$ everywhere. Abnormal X_i is spotted beneath the northeastern Pacific rise, the Rio Grande Rift, the Nevada Basin and Range, and the central Trans-Hudson Orogen, suggesting V_{sv} is faster in those regions. At >300km, most of the radial anisotropy has disappeared, except beneath the western US where $X_i < 1$, indicating a probable deep origin of the anomaly. A negative X_i anomaly is observed in the vicinity of the East Pacific Rise at all depths (I to L), suggesting a probable deep (> 300km) origin of this anomaly.

28.3 References

Arndt, N. T., et al. (2009), Origin of Archean subcontinental lithospheric mantle: Some petrological constraints, *Lithos*, 109(1-2), 61-71.

Bostock, M. G. (1998), Mantle stratigraphy and evolution of the Slave Province, *J. Geophys. Res.*, 103(B9), 21,183-121,200.

Cammarano, F. and B. Romanowicz (2007), High-Pressure Geoscience Special Feature: Insights into the nature of the transition zone from physically constrained in-

version of long-period seismic data, *PNAS*, 104, 9139-9144, doi:10.1073/pnas.0608075104

Chen, C.-W., et al. (2007), New constraints on the upper mantle structure of the Slave craton from Rayleigh wave inversion, *Geophys. Res. Lett.*, 34(L10301), doi:10.1029/2007GL029535.

Darbyshire, F. A., et al. (2000), Central structure of central and northern Iceland from analysis of teleseismic receiver functions, *Geophys. J. Int.*, 143(1), 163-184.

Darbyshire, F. A., et al. (2007), New insights into the lithosphere beneath the Superior Province from Rayleigh wave dispersion and receiver function analysis, *Geophys. J. Int.*, 169(3), 1043-1068.

Deschamps, F., et al. (2008), Stratified seismic anisotropy reveals past and present deformation beneath the East-central United States, *Earth Planet. Sci. Lett.*, 274(3-4), 489-498.

Eaton, D. W., and A. Frederiksen (2007), Seismic evidence for convection-driven motion of the North American plate, *Nature*, 446(7134), 428-431.

Eaton, D. W., et al. (2009), The elusive lithosphere-aesthenosphere boundary (LAB) beneath cratons, *Lithos*, 109(1-2), 1-22.

Fouch, M. J., et al. (2000), Shear wave splitting, continental keels, and patterns of mantle flow, *J. Geophys. Res.*, 105(3), 6255-6275.

Griffin, W. L., et al. (2004), Lithosphere mapping beneath the North American plate, *Lithos*, 77(1-4), 923-944.

Gok, R., et al. (2003), Shear wave splitting and mantle flow beneath LA RISTRA, *Geophys. Res. Lett.*, 30, 1614, doi:10.1029/2002GL016616.

Gorman, A. R., et al. (2002), Deep Probe: Imaging the roots of western North America, *Can. J. Earth Sci.*, 39(3), 375-398.

Gripp, A. E., and R. G. Gordon (2002), Young tracks of hotspots and current plate velocities, *Geophys. J. Int.*, 150(2), 321.

Marone, F., et al. (2007), 3D radial anisotropic structure of the North American upper mantle from inversion of surface waveform data, *Geophys. J. Int.*, doi: 10.1111/j.1365-246X.2007.03456.

Marone, F., and B. Romanowicz (2007), The depth distribution of azimuthal anisotropy in the continental upper mantle, *Nature*, 447(7141), 198-201.

Mckenzie, D., and K. Priestley (2008), The influence of lithospheric thickness variations on continental evolution, *Lithos*, 102(1-2), 1-11.

Mercier, J. P., et al. (2008), The teleseismic signature of fossil subduction: Northwestern Canada, *J. Geophys. Res.*, 113.

Park, J., and V. Levin (2002), Seismic anisotropy: Tracing plate dynamics in the mantle, *Science*, v296, 485-489.

Plomerova, J., et al (2002), Mapping the lithosphere-aesthenosphere boundary through changes in surface-wave anisotropy, *Tectonophysics*, 358(1-4), 175-185.

Savage, M. K., and A. F. Sheehan (2000), Seismic anisotropy and mantle flow from the Great Basin to the Great Plains, western United States, *J. Geophys. Res.*, 105(6), 13,715-713,734.

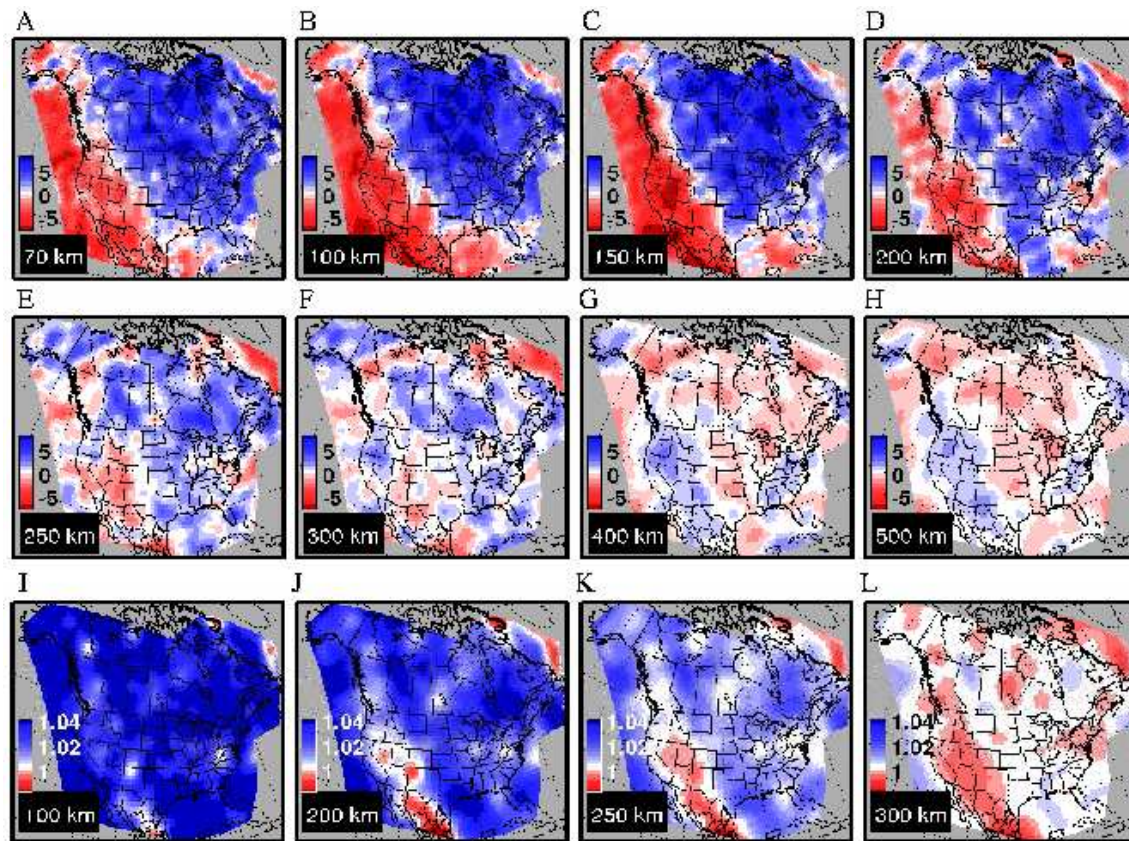


Figure 2.54: Figure 3-D isotropic V_s (A-H) and radial anisotropy ξ (I-L) model of North America upper mantle.

Schutt, D., et al. (1998), Anisotropy of the Yellowstone Hot Spot wake, eastern Snake River plain, Idaho, in *Geodynamics of lithosphere and Earth's mantle; seismic anisotropy as a record of the past and present dynamic processes.*, edited by J. Plomerova, et al., pp. 443-462, Birkhaeuser Verlag, Basel, Switzerland.

Silver, P. G., and W. W. Chan (1988), Implications for continental structure and evolution from seismic anisotropy, *Nature*, 335, 34-39.

Snyder, D. B. (2008), Stacked uppermost mantle layers within the Slave craton of NW Canada as defined by anisotropic seismic discontinuities, *Tectonics*, 27.

Thybo, H. (2006), The heterogeneous upper mantle low velocity zone, *Tectonophysics*, 416(1-4), 53-79.

van der Lee, S. (2002), High-resolution estimates of lithospheric thickness from Missouri to Massachusetts, USA, *Earth Planet. Sci. Lett.*, 203(1), 15-23.

Vinnik, L., et al. (1984), Anisotropy of the lithosphere according to the observations of SKS and SKKS waves, *Dokl. Akad. Nauk SSSR*, 278, 1335.

Waite, G., et al. (2005), Models of lithosphere and asthenosphere anisotropic structure of the Yellowstone hotspot from shear wave splitting, *J. Geophys. Res.*, 110(B11304), doi:10.1029/2004JB003501.

Walker, K. T., et al. (2004), Shear-wave splitting beneath the Snake River Plain suggests a mantle upwelling beneath eastern Nevada, USA, *Earth Planet. Sci. Lett.*, 222(2), 529-542.

West, J. D., et al. (2009), Vertical mantle flow associ-

ated with a lithospheric drip beneath the Great Basin, *Nature Geosci.*, 2(6), 439-444.

Zandt, G., and E. Humphreys (2008), Toroidal mantle flow through the western US slab window, *Geology*, 36(4), 295-298.

29 Weak Mantle in NW India Probed by Postseismic GPS Measurements Following the 2001 Bhuj Earthquake

D. V. Chandrasekhar and Roland Bürgmann

29.1 Introduction

Transient crustal deformations induced by large earthquakes are used to infer the rheology of the continental crust and the upper mantle. Generally, these studies find that the elastically strong part of the continental crust is 15-30 km thick, that the lower crust has a higher viscosity than the uppermost mantle, and that the mantle asthenosphere has a low viscosity ($< 5 \times 10^{19}$ Pa s) (Bürgmann and Dresden, 2008). However, all of the postseismic deformation transients considered to date are from active plate boundary zones with strongly thinned lithosphere (< 60 km), and relatively hot and hydrated mantle asthenosphere. In contrast, studies of postglacial rebound in stable shield areas (Fennoscandia, North America) indicate an elastic plate thickness of ~ 100 km overlying a high viscosity substratum ($> 10^{20}$ Pa s) (Milne et al., 2001). The Bhuj earthquake of January 26, 2001 in Kachchh, India is the largest event (M_w 7.6) in the last 50 years to strike the Indian shield in its recorded history, lies > 300 km from the nearest active Plate boundary and provides a unique opportunity to probe the rheology of the deep lithosphere in an intraplate region. We use GPS displacements to models of postseismic deformation caused by the earthquake to assess the viscous strength of the lower crust and upper mantle.

29.2 Postseismic GPS Observations

Time series of GPS-measured surface displacements document transient deformation during 6 years following the Bhuj earthquake. We update and expand on initial results from this network published by Reddy and Sunil, 2007 who provide further detail on the GPS observations and analysis. Sites are labeled in the maps of Figure 2.55. Time series of positions of each site in the well-determined ITRF 2000 are obtained from the combined quasi-observations and provide relative position time series from February 2001 to January 2007 of each site with respect to a station at Ahmedabad (AHMD). The time series show the decaying nature of the postseismic motions and are well represented by a log function $a' + b' \log(t)$, where t is the time (yr) and a' and b' are constants to fit the displacement time series. We used the logarithmic curve-fit values to estimate total displacements at each site with respect to AHMD for 6 months, 1 year, 2 years and 6 years after the Bhuj earthquake.

Viscoelastic models and results

The broadly distributed nature of the postseismic deformation field suggests a deeply buried source of transient deformation and thus we primarily consider models of viscous relaxation in our investigation. To calculate the viscoelastic postseismic deformation we adopt the earthquake source parameterization of Antolik and Dreger (2003), which is also consistent with geodetic constraints on the rupture (Chandrasekhar et al., 2004; Schmidt and Bürgmann, 2006). The location of the rupture is shown in the maps in Figure 2.55. Strike, dip, rake, and seismic moment are 82° , 51° , 77° , and $1.6 \cdot 10^{20}$ Nm, respectively. The model rupture is 40 km long and 10–32 km deep. The slip distribution of Antolik and Dreger (2003) is simplified with a larger amount of slip (8.2 m) confined to the center ($25 \times 15 \text{ km}^2$) and less slip (1.7 m) on the surrounding part. We calculate postseismic deformation using VISCO1D (Pollitz, 1997), for a simple layered Earth model consisting of an elastic plate overlying a viscoelastic substrate. The free model parameters are the thickness H_p of the elastic plate and the viscosity η_a of the viscoelastic material below. The minimum root mean-square error (RMS) between the observed and predicted motions is found at $H_p = \sim 34$ km for all time periods considered (Figure 2.55), which is close to the local crustal thickness inferred from seismic data (Sarkar et al., 2001). Optimal effective mantle viscosities increase with time from $\eta_a = 3 \times 10^{18}$ Pa s for the first 6 month period to 2×10^{19} Pa s for the full 6 years displacements, which is consistent with a stress dependent rheology of the upper mantle (Freed and Bürgmann, 2004). An increase of the coseismic moment of the rupture by $1 \frac{1}{2}$ times raises the effective viscosity estimates by 30-50% for the different time intervals considered, given that some teleseismic moment estimates are as high as 3.6×10^{20} Nm (Wesnousky et al., 2001). We also estimate the viscosity of a 15-km-thick lower crustal layer separate from the upper mantle. The misfit suggests that the observed data do not require relaxation of the lower crust and indicate a lower bound of 10^{20} Pa s on its effective viscosity. We find very small contribution of mainshock induced pore-pressure changes to the near-field horizontal deformation and subsidence of as much as 65 mm localized over the buried coseismic rupture. None of the afterslip models demonstrate the observed pattern or magnitude of motions of the GPS network, suggesting that viscous relaxation and afterslip are distinctly different.

Discussion and Conclusions

The estimated first-order viscoelastic structure deduced consists of an elastic plate whose thickness is ~ 34 km and an underlying viscoelastic asthenosphere whose effective viscosity is 2×10^{19} Pa s, during the 6-year observation period. Estimated effective viscosities increase with time suggesting power-law rheology due to dislocation creep. Modest, shallow afterslip may have contributed to the near-field GPS. The inferred viscosity of the upper mantle below the Bhuj region is closer to that found for thermally weakened and hydrated mantle below western North America and other back-arc or former back-arc regions (viscosity estimates generally range from $0.1 - 1 \times 10^{19}$ Pa s below 40-60 km depth) than that found from ice-unloading studies over the North American and Fennoscandian cratons (ranging from $0.5 - 1 \times 10^{21}$ Pa s below a >100 km thick elastic lithosphere). The low mantle viscosity deduced may be the result of thermal weakening due to the late Cretaceous Reunion (Deccan) plume, which is indicated by a 200-km-wide seismic wave speed anomaly in the uppermost mantle beneath the region (Kennett and Widiyantoro, 1999). In contrast, the apparent strength of the lower crust is consistent with a mafic and dry composition indicated by unusually high seismic velocities at lower crustal depths (Mandal and Pujol, 2006), which may have developed in association with intrusive activity during an early Jurassic period of rifting (Chandrasekhar and Mishra, 2002). The mantle lithosphere in the Gujarat region in NW India appears to be weaker than fully intact continental shields. Relaxation of remote stresses in such a weak zone can concentrate stress in the overlying crust and lead to the observed intraplate seismicity in this region.

29.3 Acknowledgements

This study was accomplished while DC was visiting researcher at the University of California, Berkeley, USA, funded by the DST, New Delhi through a BOYSCAST fellowship. RB acknowledges support by NSF grant EAR-0738298.

29.4 References

Antolik, M., Dreger, D., Rupture process of the 26 January 2001 M_w 7.6 Bhuj, India, earthquake from teleseismic broadband data, *Bull. Seismol. Soc. Am.*, *93*, 1235-1248, 2003.

Bürgmann, R., Dresen, G., Rheology of the lower crust and upper mantle: Evidence from rock mechanics, geodesy and field observations, *Ann. Rev. Earth Plan. Sci.*, *36*, 531-567, 2008.

Chandrasekhar, D.V., Mishra, D. C., Some geodynamic aspects of Kutch basin and seismicity: An insight from gravity studies, *Current Science*, *83*, 492-498, 2002.

Chandrasekhar, D.V., Mishra, D. C., Singh, B., Vijayakumar, V., Bürgmann, R., Source parameters of the Bhuj earthquake, India of January 26, 2001 from height and gravity changes, *Geophys. Res. Lett.*, *31*, doi:10.1029/2004GL020768, 2004.

Freed, A. M., Bürgmann, R., Evidence of power-law flow in the Mojave desert mantle, *Nature*, *430*, 548-551, 2004.

Kennett, B. L. N., Widiyantoro, S., A low seismic wavespeed anomaly beneath northwestern India: A seismic signature of the Deccan Plume?, *Earth and Planetary Science Letters*, *165*, 145-155, 1999.

Mandal, P., Pujol, J., Seismic imaging of the Aftershock zone of the 2001 M_w 7.7 Bhuj earthquake, India, *Geophys. Res. Lett.*, *33*, 1-4, 2006.

Milne, G. A., Davis, J. L., Mitrovica, J. X., Scherneck, H. -G., Johansson, J. M., Vermeer, M., Koivula, H., Space-geodetic constraints on glacial isostatic adjustment in Fennoscandia, *Science*, *291*, 2381-2385, 2001.

Pollitz, F. F., Gravitational viscoelastic postseismic relaxation on a layered spherical Earth, *J. Geophys. Res.*, *102*, 17921-17941, 1997.

Reddy, C. D., Sunil, P. S., Post-seismic crustal deformation and strain rate in Bhuj region, western India, after the 2001 January 26 earthquake, *Geophysical Journal International*, *172*, 593-606, doi: 10.1111/j.1365-1246X.2007.03641.x., 2008.

Sarkar, D., Reddy, P. R., Sain, K., Mooney, W. D., Catchings, R. D., 2001. Kutch seismicity and crustal structure, *Geol. Soc. Am. Programs*, *262*, 2001.

Schmidt, D. A., Bürgmann, R., InSAR constraints on the source parameters of the 2001 Bhuj earthquake, *Geophys. Res. Lett.*, *33*, doi:10.1029/2005GL025109, 2006.

Wesnousky, S. G., Seeber, L., Rockwell, K. T., Thakur, V., Briggs, R., Kumar, S., Ragona, D., Eight days in Bhuj: Field report bearing on surface rupture and genesis of the January 26, 2001 Republic Day earthquake of India, *Seismol. Res. Lett.*, *72*, 514-524, 2001.

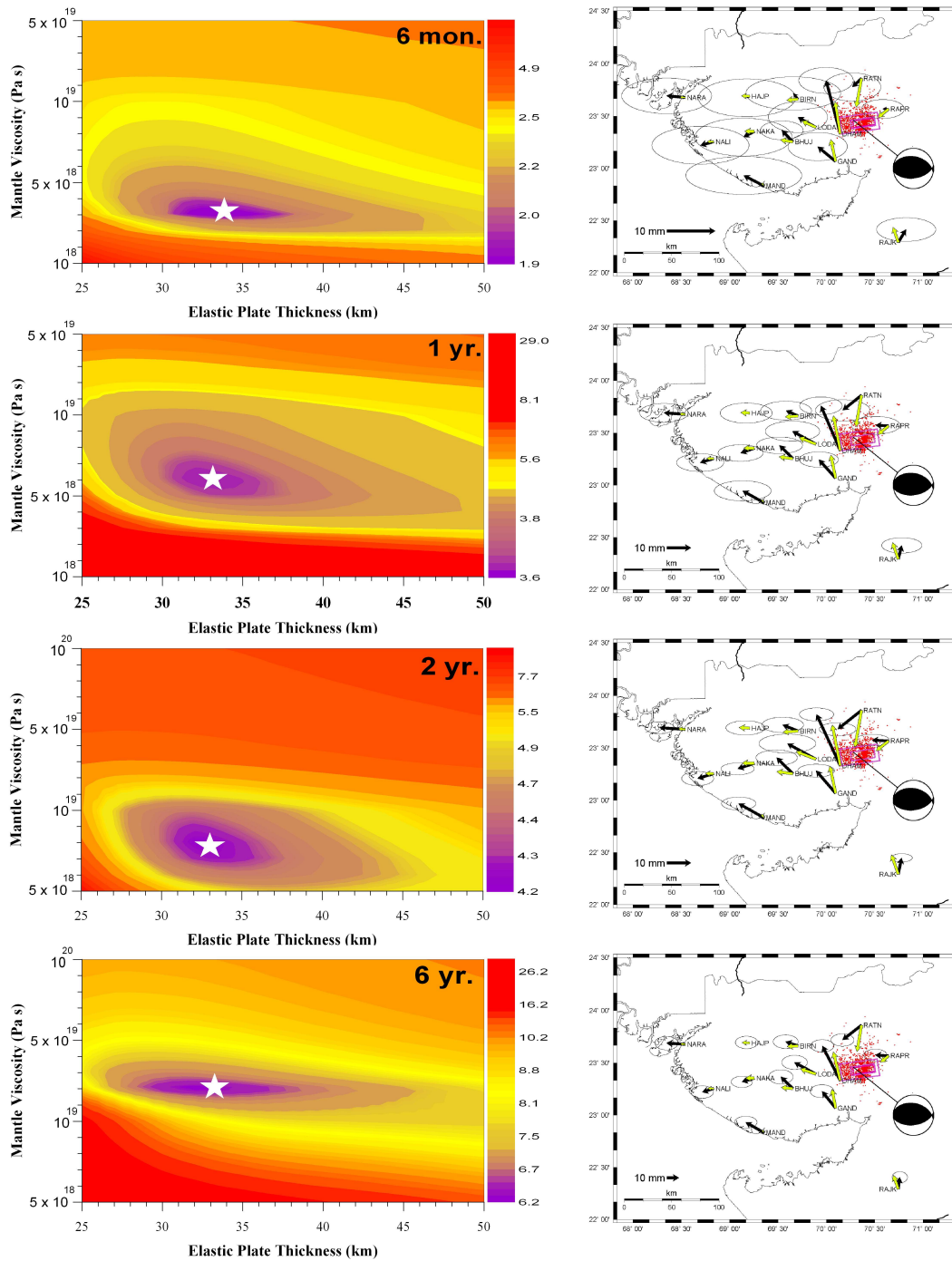


Figure 2.55: Model results. The RMS misfit between the calculated and observed horizontal displacements as a function of elastic plate thickness (H_p) and asthenosphere viscosity (η_a) for the two layer Earth model as a function of time since the earthquake. The star marks the best-fit displacement model with the least RMS error value, whose best-fit horizontal displacements are plotted adjacent to the misfit plot. Vectors in black denote the observed displacement tipped with 95% confidence ellipses and yellow arrows are the calculated model displacements. (See color version of this figure at the front of the research chapter)

30 Comprehensive Test Ban Monitoring: Contributions from Regional Moment Tensors to Determine Source Type and Depth

Margaret Hellweg, Douglas Dreger and Barbara Romanowicz

30.1 Introduction

Regional distance moment tensor (MT) analysis can be used, even for relatively small magnitude events ($M > 3.4$), to discriminate explosions from naturally occurring earthquakes. For earthquakes, MT analysis can also provide insight into an event's size, depth and type of faulting. Mechanism information is also important for applications like assessing earthquake effects and tsunami warning. In this project, we apply the UC Berkeley full moment tensor code (*Minson and Dreger, 2008*) to a suite of events recorded regionally at broadband seismic stations operated by the International Monitoring System (IMS).

30.2 Events and Green's Function

For regional moment tensor analysis using the full moment tensor code, it is important to have data from three or more stations with good signals in the period band between 10 s and 100 s or more, depending on the size of the event. Typically, for events with $M < 4$, we use the period band 10 s – 50 s, for $4 < M < 5$ the band 20 s – 50 s, and for $5 < M < 7$ the band 20 s – 100 s.

Reviewing the distribution of primary IMS stations certified by April 2009, we chose the region from 30°E – 70°E and from 20°N – 45°N , for its seismicity and IMS

station availability. From the many events in the Reviewed Event Bulletin (REB), we selected two sequences from Western Iran (Figure 2.56) for two reasons: (a) Their epicenters were only about 20 km apart, so propagation paths to regional stations would be similar, and (b) the mechanisms of the largest events, as given in the GCMT catalog (Figure 2.56), were different. Magnitudes as given in the REB and in the PDE catalog (NEIC) are shown in Figure 2.56 for the mainshocks and other selected events. Of the approximately 20 events in each sequence, five were chosen from the REB, spanning a range of depths and magnitudes (Figure 2.56).

Green's functions were calculated for two 1D velocity models. The first is a generic 1D global model, *iasp91*. The second 1D velocity model is adapted from the *Pasyanos, et al. (2004)* 3D model for the region. For the chosen events, seismic moment magnitude (M_w), depth and source mechanism will be estimated using both types of Green's functions.

30.3 Ongoing Work and Perspectives

We received waveform data for the events from the IMS shortly before the ISS09 meeting. Unfortunately, no waveforms were available for stations at distances smaller than 2000 km for any events in 2002. Many of the waveforms for the 2006 events have gaps, and poor signal-to-noise ratios are particularly a problem for the small events. Based on the review of the data, we hope to be able to determine moment tensors for several 2006 events using data from the IMS. We will review recent seismicity in the region to determine whether other events have occurred which could contribute to this study.

30.4 Acknowledgements

The work performed for this project was supported by LLNL CTBT Contract B583480. Travel of MH to the ISS09 in Vienna, Austria, to present the interim results was funded by NSF Grant EAR-0926120.

30.5 References

Minson, S. and D. Dreger, Stable Inversions for Complete Moment Tensors, *Geophys. Journ. Int.*, 174, 585-592, doi:10.1111/j.1365-246X.2008.03797, 2008.

Pasyanos, M.E., W.R. Walter, M.P. Flanagan, P. Goldstein and J. Bhattacharyya, Building and Testing an a priori Geophysical Model for Western Eurasia and North Africa, *Pure appl. geophys.*, 161, 235281, 2004.

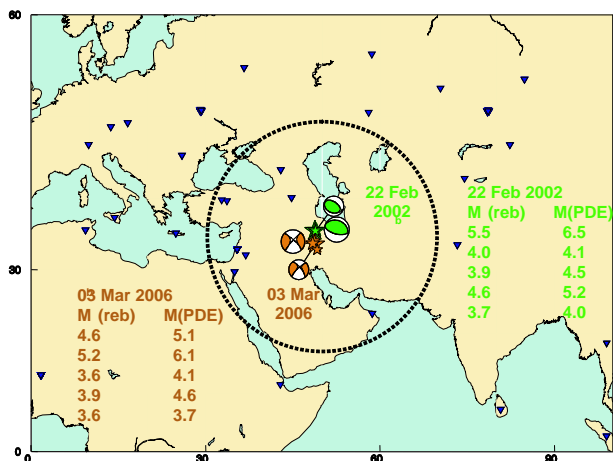


Figure 2.56: Map showing the events chosen for analysis (stars). Certified IMS stations (as of April 2009) are shown as inverted triangles. The mechanisms shown for the largest events are from the GCMT catalog. The tables give the magnitudes of the selected events.